CHEMICAL MICROSYSTEM BASED ON INTEGRATION OF RESONANT MICROSENSOR AND CMOS ASIC

A Dissertation
Presented to
The Academic Faculty

By

Kemal Safak Demirci

In Partial Fulfillment
Of the Requirements for the Degree
Doctor of Philosophy in the
School of Electrical and Computer Engineering

Georgia Institute of Technology

August 2010

CHEMICAL MICROSYSTEM BASED ON INTEGRATION OF RESONANT MICROSENSOR AND CMOS ASIC

Approved by:

Dr. Oliver Brand, Advisor
School of Electrical and Computer Engineering
Georgia Institute of Technology

Dr. F. Levent Degertekin
School of Electrical and Computer Engineering
Georgia Institute of Technology

Dr. Paul E. Hasler
School of Electrical and Computer Engineering
Georgia Institute of Technology

Dr. Peter J. Hesketh
School of Mechanical Engineering
Georgia Institute of Technology

Dr. Pamela T. Bhatti
School of Electrical and Computer Engineering
Georgia Institute of Technology

Date Approved: June 25, 2010

To my parents and my love Esra.

ACKNOWLEDGMENTS

First of all, I would like to express my appreciation and thanks to my thesis advisor Dr. Oliver Brand. While being allowed to follow an independent research, I have always felt his friendly guidance, support and encouragement throughout my PhD study. I feel very lucky that I had the opportunity to work with a professor with a great personality, broad expertise in microsystems, and excellent teaching and advising skills.

I would like to thank my dissertation committee members Dr. Paul E. Hasler, Dr. Pamela T. Bhatti, Dr. F. Levent Degertekin, and Dr. Peter J. Hesketh for their interest in my work and their constructive advice.

I want to thank Bob House for his help with PCB fabrication, David Webb for his support with the design software, Florian Herrault for his help with the measurement setup implementation, and the MIRC staff for their assistance. Also, I owe thanks to Dr. Jeanne Pitz, Nicole Cunningham, Dr. Ajit Sharma and the rest of the Mixed Signal Automotive Group at Texas Instruments for their support and helpful discussions during my co-op term there. I would like to specially thank Dr. Jeanne Pitz for giving me a chance to do my co-op at Texas Instruments and for providing IC fabrication support.

I am grateful to past and present members of our research group for their help, useful discussions and friendship. Many thanks to my colleagues Dr. Jae Hyeong Seo, Stuart Truax, Luke A. Beardslee, Dr. Kianoush Naeli, Juan M Cesaretti, Albert Byun, Jin-Jyh Su, Dr. Yulia Luzinova, and Dr. Young Do Jung. In addition, I would like to thank all my friends in Atlanta, especially Erman, Meltem, Onur, Gence, Nevin and Ahmet for making Atlanta a better and enjoyable place to live.

I would like to express my sincere gratitude to my parents and grandparents for their encouragement and patience. I have achieved all that I have with their continuos guidance and support. I would like to also acknowledge my wife's family for their

support and trust. I also owe special thanks to my brother and the Arıkan family, my uncle İstiklal, my aunt Dilek and my cousin Pınar, for their support and guidance throughout my life. Finally, I would like to express my special thanks and deepest gratitude to my wife Esra for her love, patience, understanding, and encouragement.

TABLE OF CONTENTS

LIST OF TABLES

LIST OF FIGURES

LIST OF ABBREVIATIONS

A/D	Analog-to Digital
AFM	Atomic Force Microscopy
AGC	Automatic Gain Controller
ASIC	Application-Specific Integrated Circuit
BAW	Bulk Acoustic Wave
BW	Bandwidth
CM	Common Mode
CMFB	Common-Mode Feedback
CMOS	Complementary Metal-Oxide-Semiconductor
CMRR	Common-Mode Rejection Ratio
CWA	Chemical Warfare Agent
DAC	Digital-to-Analog Converter
DAQ	Data Acquisition
DCPS	Digital-Controlled Phase Shifter
DDA	Differential Difference Amplifier
FEM	Finite Element Method
FPW	Flexural-Plate-Wave
GBW	Gain-Bandwidth
HPF	High-Pass Filter
IC	Integrated Circuit
IDT	Inter-Digitated Transducer

LOD	Limit of Detection
LPF	Low-Pass Filter
LW	Lowe-Wave
MEMS	Microelectromechanical Systems
MFC	Mass-Flow Controller
MOS	Metal-Oxide-Semiconductor
MOSFET	Metal-Oxide-Semiconductor Field Effect Transistor
OP-AMP	Operational Amplifier
PCB	Printed Circuit Board
PD	Phase Detector
PLL	Phase Locked Loop
PM	Phase Margin
PPM	Parts-per-Million
PSD	Power Spectral Density
SAW	Surface Acoustic Wave
SEM	Scanning Electron Microscope
SFM	Scanning Force Microscopy
SH	Shear-Horizontal
SNR	Signal-to-Noise Ratio
STW	Surface-Transverse-Wave
QCM	Quartz Crystal Microbalance
Q-FACTOR	Quality Factor
TCF	Temperature Coefficient of Frequency

VCO	Voltage-Controlled Oscillator
VGA	Variable-Gain Amplifier
VOC	Volatile Organic Compound

SUMMARY

The recent growth of the chemical sensor market is supported by technological advances, such as the use of microfabrication techniques, which enable low-cost, miniaturized chemical sensors. Microfabricated chemical sensors can potentially offer affordable solutions to many challenges in analytical chemistry, which cannot be solved with conventional bench-top laboratory equipment. In particular, these microsensors are useful in applications requiring continuous on-site monitoring, e.g. in threshold-level or environmental monitoring. In these applications, portability is often a key issue and, thus, reliable and low-cost hand-held chemical sensor instruments are needed. In realizing such hand-held instruments, CMOS-integrated interface electronics play a crucial role. When compared to off-chip electronics, CMOS interface circuits allow the integration of the entire system in a compact package with reduced power consumption and system cost.

The main objective of this thesis is to develop a chemical microsystem based on the integration of a silicon-based resonant microsensor and a CMOS application-specific integrated circuit (ASIC) for portable sensing applications. Two types of resonant microstructures are used as mass-sensitive sensors: cantilever and disk-shape microresonators. Based on the characteristics of the microresonators, CMOS-integrated interface and control electronics have been designed and implemented. The CMOS ASIC utilizes the self-oscillation method, which incorporates the microresonator in an amplifying feedback loop as the frequency determining element. In this manner, the ASIC includes a main feedback loop to start and sustain oscillation at or close to the fundamental resonance frequency of the microresonator. For stable oscillation, an automatic gain control loop, which regulates the oscillation amplitude by controlling the gain of the main feedback loop, has been implemented. In addition, an automatic phase control loop has been included to adjust the phase of the main feedback loop to ensure an

operating point as close as possible to the resonance frequency, which results in improved frequency stability. The CMOS chip has been interfaced to cantilever and disk-shape microresonators and short-term frequency stabilities as low as 3.4×10^{-8} in air have been obtained with a 1 sec gate time.

The performance of the implemented microsystem as a chemical sensor has been evaluated experimentally with microresonators coated with chemically-sensitive polymer films. To be able to evaluate the performance of the implemented microsystem as a chemical sensor, a gas-phase chemical measurement setup has been constructed. With this setup, gas-phase chemical measurements have been performed and different concentrations of benzene, toluene and m-xylene have been detected. The limit of detection of the implemented microsystem for benzene, toluene and m-xylene in the gas phase has been estimated as 5.3 ppm, 1.2 ppm and 0.35 ppm, respectively.

To improve the long-term stability and therefore the sensor resolution in monitoring applications with slowly changing analyte signatures, a method to compensate for frequency drift caused by environmental disturbances and aging of the microresonator has been proposed and implemented on the CMOS chip. This method uses a controlled stiffness modulation generated by a frequency drift compensation circuit to track the changes in the resonator's Q-factor in response to variations in the environmental conditions. The measured Q-factor is then used to compensate for the frequency drift using a relation between Q-factor and resonance frequency obtained through an initial calibration step. The feasibility of the proposed method has been verified experimentally by compensating for temperature-induced frequency drift during gas-phase chemical measurements.

CHAPTER 1

INTRODUCTION

Bench-top analytical instruments are widely used for chemical analyses. These instruments use various analytical techniques including gas chromatography (GC) and mass spectrometry (MS) and are able to analyze even complex mixtures with high accuracy, high selectivity, and excellent reproducibility. Since these instruments require rigid operating procedures, careful sample handling, and interpretation of the measured data, the analyses are typically time consuming and labor intensive. Also, these instruments are generally bulky and expensive. These disadvantages currently limit the application areas of bench-top instruments.

On the other hand, microfabricated chemical sensors can offer affordable solutions to many challenges in analytical chemistry, which cannot be solved with conventional bench-top laboratory equipment. While chemical sensors might offer lower sensitivity and selectivity compared to bench-top analytical instruments, they offer fast response times, in-field sensing capabilities, portability and potentially low analysis cost allowing for widespread use. Although bench-top analytical systems and chemical sensors are not directly competing, chemical sensors offer complementary solutions that should be chosen depending on the application requirements.

Chemical microsensors provide qualitative and quantitative information about the chemical character of their environment. They are typically composed of a transduction element (transducer) and a sensitive layer used as a chemical recognition element as shown in Figure 1.1. The physicochemical properties of the sensitive layer, such as its mass, volume, optical properties, or resistance, change reversibly when the sensor interacts with chemical analytes [1]. The transduction element then detects and converts this change of the physicochemical properties into an electrical signal, which is read out

with the sensor interface electronics. The effectiveness of a chemical sensor in terms of its sensitivity, selectivity, lifetime, response time, etc. is determined by both the nature of the sensitive layer, which e.g. controls selectivity, and the integration of the sensitive layer and the transducer without changing their functional properties [2, 3].

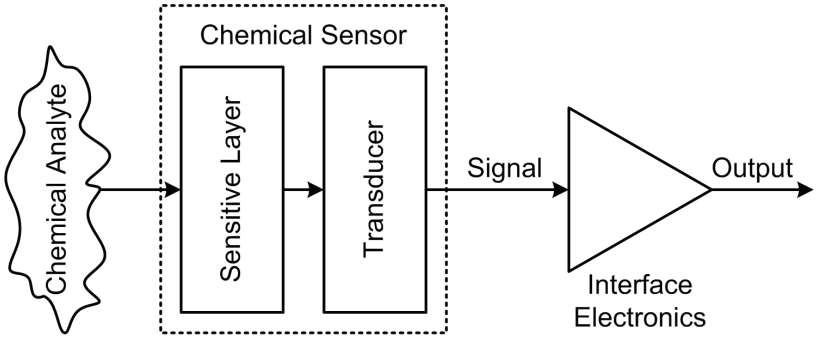

Figure 1.1: General structure of a chemical sensor.

According to their transduction principles, chemical microsensors can be divided into four main categories [4]: i) mass-sensitive sensors, ii) thermal sensors, iii) optical sensors, and iv) electrochemical sensors. Each of these transduction principles has advantages and disadvantages depending on the application and the environment in which the sensor is deployed. However, independent of the transduction principle, a good chemical sensor should provide a high selectivity, a high sensitivity, a large dynamic range, a short response time, long-term reliability, and a low-cost implementation. In the following, we will highlight applications for portable chemical sensors, present current solutions and outline the scope of this thesis.

1.1 Chemical Sensing Devices and Applications

Chemical sensor technology has attracted substantial interest for the past several decades [4]. The need for chemical sensors is rapidly growing in industry, academia, and military. This growth is supported by technological advances, especially in microfabrication techniques that allow realization of low-cost, miniaturized chemical sensors. In particular, micromachined chemical sensors and sensor arrays have tremendous potential in applications requiring continuous on-site monitoring of a range of chemical analytes, e.g. environmental monitoring applications. In many of these applications, portability and system cost are the key issues; thus, reliable and low-cost hand-held chemical sensor instruments targeting a finite number of analytes of interest rather than a complete chemical analysis are needed.

Some examples of chemical sensing scenarios include environmental monitoring, military applications, industrial health and safety monitoring, process control, automotive applications, indoor air quality monitoring, agricultural applications, scientific research, and medical diagnostics [5-8]. Environmental monitoring is required to protect people and the environment from harmful and polluting chemicals such as sulfur dioxide, carbon monoxide, nitrogen dioxide, and volatile organic compounds (VOCs) [9]. Many of these pollutants are released into the environment by vehicle emissions, power plants, refineries, and industrial and laboratory processes. The US Environmental Protection Agency (EPA) provides extensive lists of air and water pollutants that require monitoring [10, 11]. Current testing procedures for these pollutants typically rely on field sampling and subsequent analysis in centralized laboratories by conventional analytical systems, which are often based on separation techniques, such as GC/MS. Military applications include detection of chemical warfare agents (CWA), such as nerve and blister agents, that are intended for use in warfare or terrorist attacks and of explosives, e.g. at airports. In automotive applications, chemical microsensors can be used to control heating, ventilation and air conditioning for increased driver and passenger comfort and safety,

especially in traffic jams. In this case, e.g. the air circulation is started when a threshold level of carbon monoxide and VOCs is reached. The detection of the exhaust gas to improve combustion efficiency is another automotive application [12]. As an example for industrial applications, chemical sensors can be employed to detect toxic gases and alert workers of possible health and safety risks. Also, chemical sensors can be incorporated into automated process monitoring and control systems in the industry [7]. One of the medical diagnostics applications that has attracted interest in recent years is monitoring patient health by breath analysis [13]. Breath primarily consists of nitrogen, oxygen, carbon dioxide, inert gases, water vapor, and VOCs (e.g., acetone, isoprene, and pentane). The organic constituents of blood can be examined by analysis of the exhaled breath. A large number of studies have examined the effect of different diseases, including asthma, chronic obstructive pulmonary disease, and lung and breast cancer, on the breath constituents [13, 14].

There are various suppliers of individual chemical sensors, which are mostly fabricated using conventional rather than microfabrication techniques. An example is metal oxide sensors manufactured by Figaro [15] for different gas sensing applications. These stand-alone sensor components are generally embedded into a chemical sensing system, which includes appropriate driving and signal conditioning circuitry to provide a suitable output signal. Of particular interest to this thesis are portable, hand-held chemical sensing instruments, several of which are currently on the market and can be utilized in many of the applications mentioned above. Table 1.1 gives examples of such instruments, with most of them relying on electrochemical transducers. The costs of these devices range from $ 430 to $ 6,400, depending on the number of sensors and accessories included. In general, one must distinguish between single-sensor systems, which are typically targeting a single analyte or analyte class, and multi-sensor systems, which generally provide selectivity for a small number of analytes. The discrimination of multiple analytes generally requires an array of sensors [16], which each offer at least

Table 1.1: Examples of commercially available portable, hand-held chemical sensing instruments.

Device	Company	Transducer	Price	Ref.
C16 PortaSens II	Analytical Technology, Inc.	Electrochemical	$ 1,100 and up	[17]
GasAlertMicro 5 PID	BW Technologies	Electrochemical, PID	$ 1,500 and up	[18]
X-am 7000	Draeger Safety, Inc.	Electrochemical, Thermal, PID, IR	$ 2,900 - $ 6,400	[19]
Recon/4	Enmet Corp.	Electrochemical, Thermal	Not specified	[20]
M40	Industrial Scientific Corp.	Electrochemical, Thermal	$ 430 - $ 650	[21]
IQ-250	International Sensor Technology	Electrochemical, Solid-state	$ 795 - $ 1,500	[22]
Sirius	MSA	Electrochemical, Thermal, PID	Not specified	[23]
HAZMATCAD Plus	MSA	Mass-sensitive, Electrochemical	Not specified	[24]
MultiLog 2000	Quest Technologies, Inc.	Electrochemical	$ 1,700	[25]
VRAE	RAE Systems	Electrochemical, Thermal	$ 1,400 - $ 2,200	[26]
Scout	Scott Health & Safety	Electrochemical, Thermal, PID	$ 1,400	[27]
Genesis	Thermo Fisher Scientific	Electrochemical, Thermal	$ 795 - $ 1,300	[28]
Sensit Gold CGI	J and N Enterprises, Inc.	Electrochemical, Thermal	Not specified	[29]
Biosystems MultiVision	Sperian Protection	Electrochemical, Thermal	$ 620 - $ 1,800	[30]
MiniMax X4	Honeywell Analytics, Inc.	Electrochemical	Not specified	[31]

partial selectivity, or either spectroscopic or separation techniques [32, 33]. The possibility of integrated sensor arrays is one of the key benefits of using microfabrication techniques.

Among possible miniaturized chemical sensing platforms, we are particularly interested in mass-sensitive chemical microsensors and their integration into a chemical sensing platform. Mass-sensitive chemical sensors simply measure the mass of the analyte molecule of interest and, thus, are arguably the most fundamental type of chemical sensor. Silicon-based mass-sensitive sensors can be readily miniaturized and arranged in arrays and are thus well suited for hand-held instruments. As a result, they have been widely researched in recent years (see Chapter 2). However, research has typically focused on the transducer and often neglected important system aspects, such as the stability of the chemical layer or the role of the interface circuitry. Importantly, system aspects and especially the circuitry used to condition the sensor and read out the sensor signal can improve the sensor performances in critical areas, such as long-term stability. Thus, the focus of this thesis is to follow a systems approach and, in particular, develop interface circuitry for a mass-sensitive chemical sensor array that ensures that the sensors are automatically driven at their optimal working point and that temperature-induced long-term drift is compensated for. Thereby, the thesis builds on research into mass-sensitive chemical microsensors, in particular silicon-based cantilever [34] and disk-resonators [35], and develops a sensing system around the microsensors.

The developed chemical sensing system is tested by detecting volatile organic compounds (VOCs) in air. VOCs including benzene, toluene, xylenes, and hexane [36] are usually used in industrial and commercial products including fuels, paints, aerosols, cosmetics, disinfectants, refrigerants, and pesticides [37]. According to the air pollutant emissions trends data listed by the Environmental Protection Agency (EPA), VOCs are one of the major air pollutants in the U.S.A. (15,927 thousand tons in 2008) [38] because of their extensive industrial and household usage. However, there are only a limited

number of portable, hand-held instruments capable of detecting individual VOCs. Portable instruments for VOC sensing typically rely on photoionization detectors (PIDs) and only have the ability to monitor the total concentration of all photoionizable VOCs present in the environment. In other words, they do not have the ability to distinguish between individual VOCs. By implementing silicon-based resonant sensor arrays coated with different sensing layers, individual VOCs can be distinguished, i.e. higher selectivity can be achieved. However, like most of the other miniaturized chemical sensors, silicon-based resonant sensors have not achieved their full potential for commercial portable instruments yet. The primary reason is the performance degradation in the harsh field environment. Very low analyte concentrations, high noise levels, and constantly changing environmental conditions in the field reduce the sensor performance. The requirement to overcome these problems is system approach, where sensor and interface electronics are integrated and optimized together.

1.2 Outline of Thesis

The main objective of this thesis is to develop a chemical microsystem based on the integration of a silicon-based resonant microsensor and a CMOS application-specific integrated circuit (ASIC) for portable sensing applications. Accordingly, CMOS circuit architectures for signal conditioning are primarily investigated to implement a low-cost and high performance microsystem.

After the introduction, Chapter 2 gives an overview of mass-sensitive chemical sensors. This overview explains transducer types, open- and closed-loop interfacing techniques, and performance parameters including selectivity, sensitivity, frequency stability, and limit of detection. Moreover, possible integration techniques such as hybrid, monolithic and flip-chip integration to connect CMOS and sensor chips are discussed.

Chapter 3 gives a system-level overview of the implemented chemical microsystem. The resonant microstructures used in this work are presented, and their

integrated excitation and detection mechanisms are explained. Then, subsystems of the integrated CMOS interface and control electronics are introduced.

In this work, two different CMOS-integrated ASICs have been implemented. Chapter 4 explains the design of the more recently fabricated ASIC in detail and, at the same time, compares the two chips where different circuit topologies have been used to obtain the same functionality. The performance tests of the ASIC interfaced to a microresonator are also provided in this chapter.

In Chapter 5, gas-phase chemical measurements performed with the implemented microsystem and the setup used in these measurements are presented. Detection of VOCs is demonstrated, and the performance of the realized microsystem is evaluated.

A frequency drift compensation method based on a controlled stiffness modulation by a feedback loop is introduced in Chapter 6. The concept of the proposed compensation method and experimental results are presented in this chapter.

Finally, Chapter 7 summarizes the research results and discusses possible future improvements.

1.3 Major Results

1.3.1 CMOS-Integrated Interface Electronics

CMOS-integrated interface and control electronics to operate a mass-sensitive resonant microsensor have been implemented. The electronics include a main feedback loop to start and sustain oscillation at or close to the dominant resonance frequency of the microresonator. For stable oscillation, an automatic gain control loop has been implemented to regulate the oscillation amplitude by controlling the gain of the main feedback loop. In addition, an automatic phase control loop has been included to adjust the phase of the main feedback loop to ensure an operating point as close as possible to the resonance frequency, which results in improved frequency stability. The CMOS chip

has been interfaced to cantilever and disk-shape microresonators and short-term frequency stabilities as low as 3.4×10^{-8} in air have been obtained with a 1 sec gate time.

1.3.2 Gas-Phase Chemical Measurements

The CMOS chip has been interfaced to microresonators coated with a chemically-sensitive film, and therefore an integrated chemical microsystem has been realized. To be able to evaluate the performance of the implemented microsystem as a chemical sensor, an automated gas-phase chemical measurement setup has been constructed. With this setup, gas-phase chemical measurements have been performed and different concentrations of VOCs have been detected. The limit of detection of the microsystem in the gas phase has been estimated as 5.3 ppm, 1.2 ppm, and 0.35 ppm for benzene, toluene, and m-xylene, respectively.

1.3.3 Frequency Drift Compensation

To compensate for frequency drift caused by environmental disturbances, a frequency drift compensation method has been proposed and implemented on the CMOS chip. This method uses a controlled stiffness modulation generated by the frequency drift compensation circuit to track the changes in the resonator's Q-factor in response to variations in the environmental conditions. The measured Q-factor is then used to compensate for the frequency drift using a relation between Q-factor and resonance frequency obtained through an initial calibration step. The feasibility of the proposed method has been verified experimentally by compensating for temperature-induced frequency drift during gas-phase chemical measurements.

CHAPTER 2

MASS-SENSITIVE CHEMICAL SENSORS

Mass-sensitive chemical sensors belong to the class of resonant sensors, which are excited at one of their resonance modes, while changes in the resonance characteristics (e.g. frequency, amplitude or phase) are monitored. As their name suggests, these chemical sensors respond to the mass loading on the sensor caused by adsorption/desorption of the chemical analytes in the sensitive layer. This mass loading results in a change in the resonance frequency, quality factor (Q-factor), phase, or vibration amplitude of the sensor. The resonance frequency is usually chosen as the sensor output signal, since the frequency signal can be easily digitized using a counter. This digitization eliminates the inaccuracies caused by analog-to-digital (A/D) conversion and provides a wide dynamic range [39]. Moreover, the frequency output is not sensitive to amplitude fluctuations associated with analog signals and can be measured with high resolution [40]. In addition, mass-sensitive chemical sensors allow realization of sensor arrays with a relatively simple fabrication process and show high inherent sensitivity. These advantages make these sensors promising candidates for portable chemical sensor systems for continuous real-time monitoring applications [36]. This chapter gives an overview of mass-sensitive chemical sensors, including transducer types, interfacing techniques, performance parameters, and integration methods.

2.1 Transducer Types

Acoustic wave and silicon-based devices have been extensively used as the transducers to implement mass-sensitive chemical sensors. The operation principles, advantages, and disadvantages of these devices are explained in the following sections.

2.1.1 Acoustic Wave Devices

Acoustic wave devices use piezoelectric excitation and detection; thus, they are fabricated on piezoelectric substrates such as quartz (SiO_2), lithium tantalite ($LiTaO_3$), lithium niobate ($LiNbO_3$), gallium arsenide (GaAs), silicon carbide (SiC), or using piezoelectric thin films such as zinc oxide (ZnO), and aluminum nitride (AlN) deposited e.g. on silicon substrates [41, 42]. Exciting the device with an AC voltage generates an acoustic wave traveling through or on a substrate. Property changes on the device surface affect the velocity or amplitude characteristics of this acoustic wave. When an acoustic wave device is used as a mass-sensitive sensor, a sensitive layer is coated on the device surface. In this case, a mass change caused by the adsorption/desorption of analytes in the sensitive layer alters the wave velocity, which in turn results in a change in the resonance frequency of the acoustic wave device.

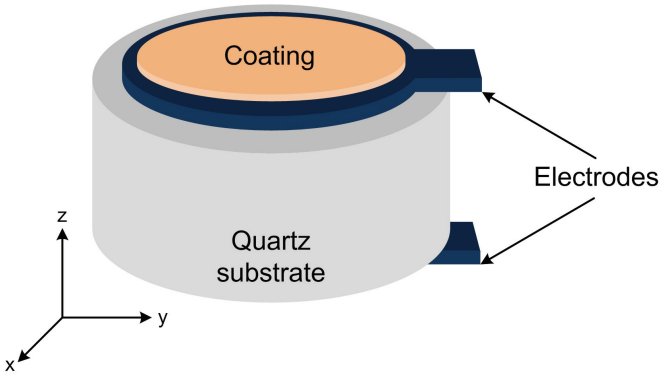

Figure 2.1: Schematic diagram of a QCM, which is composed of an AT-cut quartz substrate with two electrodes implemented on both sides.

Acoustic wave devices are classified as bulk acoustic wave (BAW) and surface acoustic wave (SAW) devices based on the mode of wave propagation. In BAW devices,

the wave propagates through the substrate. The most common BAW device is the quartz crystal microbalance (QCM), which is typically composed of an AT-cut quartz substrate with two electrodes implemented on both sides as shown in Figure 2.1. QCMs are operated as resonators with resonance frequencies ranging generally between 5 and 30 MHz [43, 44]. As a result of their high Q-factors, QCMs have excellent frequency stability not only in air but also in water [45]. This allows use of QCMs as chemical sensors in both gas and liquid mediums. Additionally, QCMs show a low temperature coefficient of frequency (TCf) if the quartz substrate is cut properly. However, QCMs generally show the lowest mass sensitivity among the acoustic wave devices. In spite of being simple, the fabrication steps of QCMs are not compatible with integrated circuit fabrication, and their sizes limit the arrayability.

The wave propagation is on the surface of the substrate in SAW devices, which utilize comb-like electrodes called inter-digitated transducers (IDTs) for excitation and detection of acoustic waves. Depending on the crystal orientation, substrate or plate geometry, and material properties, IDTs are able to generate a variety of SAWs including Rayleigh-waves, surface-transverse-waves (STWs) (also known as shear-horizontal (SH) waves), Love-waves (LWs), and flexural-plate-waves (FPWs) (also know as Lamb-waves) [44, 46]. SAW devices using these types of acoustic waves can generally be operated in both gas and liquid media with the exception of Rayleigh-wave devices, which are only suitable for gas-phase sensing because of their radiation losses in liquid. Since STW and LW devices require piezoelectric substrates, they are not CMOS-compatible. On the other hand, Rayleigh-wave and FPW devices can be implemented using CMOS-compatible processes with piezoelectric layers patterned on silicon substrates [47].

SAW sensors are typically implemented using two approaches i.e. either as a delay-line or a resonator [39]. Figure 2.2 shows a Rayleigh-wave sensor implemented with the delay-line approach. In this approach, a sensitive coating is placed between two

IDTs. When an AC signal is applied to one of the IDTs, a two-dimensional wave propagating along the surface of the substrate with a depth of approximately one wavelength is generated. The wave reaches the second IDT after some delay and is detected by this IDT. As mentioned before, adsorption of chemical analytes in the sensitive coating decreases the wave velocity resulting in a decrease of the wave propagation time. The resonator approach is similar to the delay-line except for the placement of the IDTs. In the resonator approach, the IDTs are placed in the center of the substrate, and the generated waves are reflected back to the IDTs for detection by gratings implemented on two ends of the substrate [39].

Compared to QCMs, SAW chemical sensors have higher operating frequencies, generally between 100 and 1000 MHz [39, 48]. Moreover, SAW sensors generally show higher mass sensitivities than QCMs because of their surface concentrated acoustic energy and higher resonance frequencies.

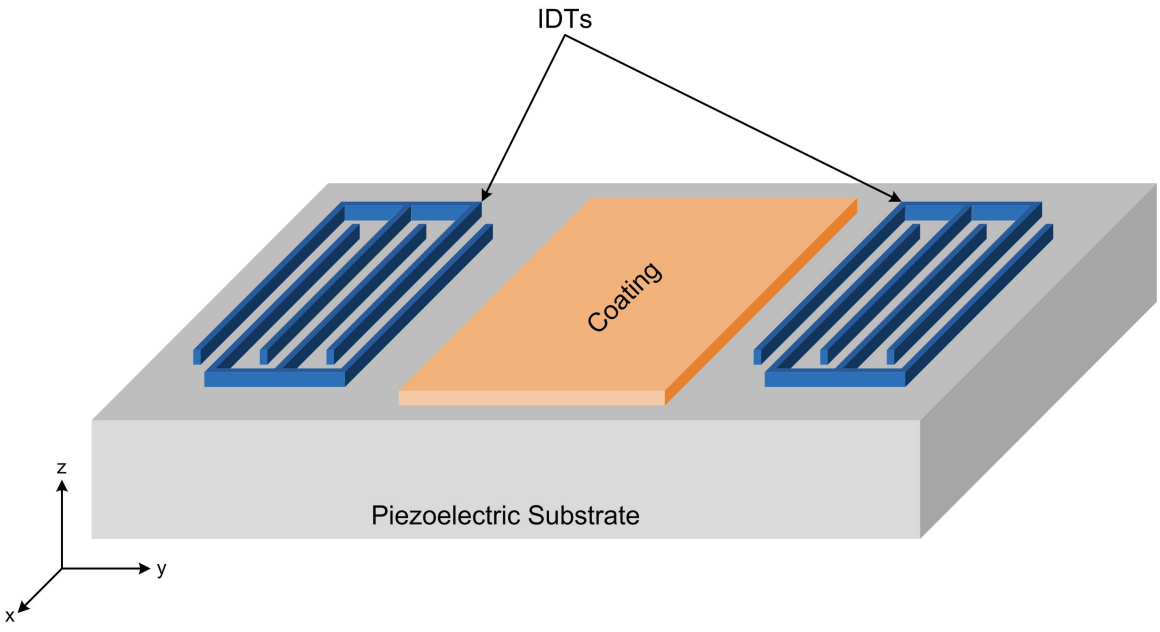

Figure 2.2: Schematic diagram of a Rayleigh-wave SAW sensor implemented with the delay line approach.

Chemical sensing in the gas and liquid phases with acoustic wave devices has been widely investigated. QCM arrays have been used to detect volatile organic compounds (VOCs) in the gas [49-51] and liquid phase [52]. Detection of warfare agents in the gas phase [53] and VOCs in the gas [54] and liquid phase [55] have been shown using single and arrays of SAW devices. However, the high operating frequencies of acoustic wave devices make the design of interface electronics complicated, and result in poor signal-to-noise ratio (SNR) and increased power consumption. Moreover, the relatively large dimensions of these sensors limit the number of elements that can be implemented in sensor arrays. In addition, the piezoelectric substrates used as structural materials in most of these sensors make their fabrication processes more complex and expensive. Because of these disadvantages, silicon-based resonant chemical sensors have gained considerable interest in recent years.

2.1.2 Silicon-based Devices

The most common silicon-based resonant microstructures are microcantilevers, which have been widely used as transducers in mass-sensitive sensors [56]. Figure 2.3 shows a schematic diagram of a microcantilever resonant sensor. The base of the cantilever is attached to the silicon substrate, and the free-standing end is covered with a sensitive coating. The cantilever is actuated at its fundamental resonance frequency that shifts when there is a mass loading as a result of analyte adsorption in the sensitive coating. This microstructure together with suitable excitation and detection elements can be implemented using CMOS-compatible fabrication steps with silicon, silicon dioxide, and silicon nitride as typical structural materials. CMOS-compatible fabrication also allows monolithic integration of the sensor interface circuitry on the sensor chip, if needed.

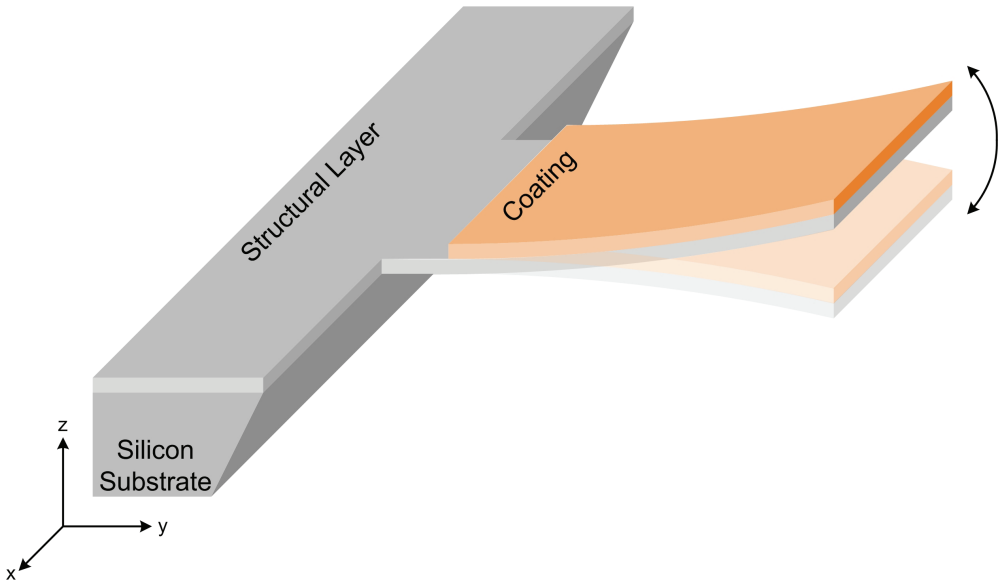

Figure 2.3: Schematic diagram of a silicon-based microcantilever resonant sensor.

Various excitation and detection schemes have been exploited to operate the cantilever at its resonance frequency. The excitation schemes include electrothermal, magnetic, electrostatic, piezoelectric, and optical methods, and the detection schemes comprise capacitive, piezoresistive, and optical readout methods [57]. The optical and piezoelectric techniques are not suitable for integration with CMOS technology and generally increase the cost of the sensor system. Besides, electrostatic excitation and capacitive detection cannot be used in sensing applications in a liquid medium. On the other hand, piezoresistive detection, utilizing integrated resistors typically arranged in a Wheatstone bridge configuration, is both CMOS-compatible and applicable to liquid-phase chemical sensing. Integrated resistors can be implemented with either doped single crystal silicon or metal-oxide-semiconductor (MOS) transistors. The disadvantage of this detection technique is its relatively high power consumption.

Electrothermal excitation is based on the bimorph effect and can be implemented with CMOS-compatible integrated resistors, which are driven with an alternating current

to generate periodic temperature variations. Although a simple method, thermal excitation requires relatively high heating power, a disadvantage for portable sensor applications.

Magnetic actuation utilizes a microfabricated wire loop on the cantilever, which is driven with an alternating current in a static magnetic field to generate an out-of-plane Lorentz force [58]. The magnetic excitation offers lower power consumption compared to thermal excitation. However, it requires a permanent magnet that increases the size of the sensor system.

Microcantilevers have been widely used for gas-phase chemical sensing. Examples include detection of VOCs [59, 60] and chemical warfare agents [61]. However, high viscous damping affects the out-of-plane operation of the cantilever in liquid mediums and hence reduces the sensor resolution because of the reduced Q-factor. Therefore, microcantilevers have been less used for liquid-phase sensing [62].

Microcantilevers can also be operated in a static-bending mode that should not be confused with mass-sensitive operation. In the static mode, instead of a mass change, the interaction of the sensitive layer with chemical species causes a change in surface stress resulting in bending of the microcantilever [56]. These sensors are susceptible to low-frequency (1/f) noise because of the static nature of the measurements, limiting the sensor sensitivity [57].

With many processing steps borrowed from the integrated circuit (IC) technology, fabrication techniques for microelectromechanical systems (MEMS) allow mass production of silicon-based resonant chemical sensors with simple process steps at low cost. Compared to acoustic wave devices, silicon-based resonant sensors typically have smaller dimensions. Reduction in sensor sizes allows implementation of sensor arrays with a large number of elements and detection of smaller masses. Therefore, improved selectivity and better mass sensitivity can be achieved. Because of these advantages,

silicon-based resonant sensors are promising candidates for portable chemical sensor systems and have been utilized in this research.

2.2 Interfacing Techniques

In addition to the characteristics of the sensor, the performance of a chemical sensor system also relies on the sensor interface electronics. The interface electronics detect low-level sensor signals, which are embedded in noise and parasitics, and at the same time actuate the sensor. Consequently, the right design of the interface circuitry ensures the effectiveness of a sensor system and requires the assessment of both the sensor characteristics and the applications in which the sensors are used.

The interaction of the resonant sensor with a measurand, e.g. a chemical analyte causes a change in the resonance frequency, Q-factor, phase, and vibration amplitude of the resonant sensor. Because of the advantages explained in the previous section, the resonance frequency is usually chosen as the output signal of the sensor. Circuitry techniques to monitor frequency output signals from resonant sensors can be divided into two categories: i) open-loop methods and ii) closed-loop methods.

2.2.1 Open-loop Methods

One of the most common open-loop methods is the analysis of the transfer function. Figure 2.4 shows the schematic diagram of this method in which a network analyzer with a signal output (RF-Out), a reference input (R), and a signal input (A) is used. RF-Out applies an AC signal to both the excitation element of the resonator and the R input. The detection signal of the resonator is connected back to the A input of the network analyzer and monitored while the frequency of the AC signal is swept. The network analyzer then determines the transfer function (amplitude and phase) of the

resonator (see Figure 2.5) as the ratio of the detection signal to the excitation signal (A/R).

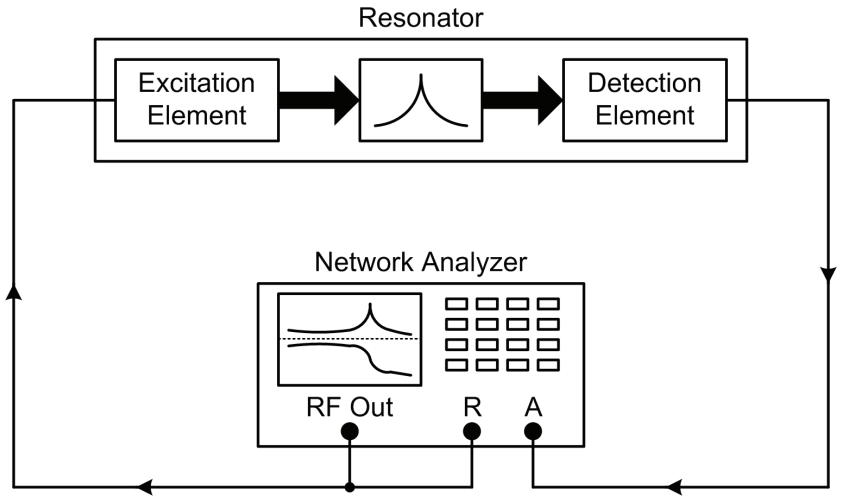

Figure 2.4: Schematic diagram of the transfer function analysis in which a network analyzer with a signal output (RF-Out), a reference input (R), and a signal input (A) is used.

The transfer function analysis provides the amplitude response, phase response, Q-factor, and resonance frequency of the resonator. Figure 2.5 presents a typical transfer function of a resonator. Here, the Q-factor is given by

$$Q = \frac{f_0}{f_U - f_L} = \frac{f_0}{BW}, \tag{2.1}$$

where f_0 is the fundamental resonance frequency of the resonator, BW is the 3dB-bandwidth of the resonance peak, and f_U and f_L are the upper and lower 3-dB cut-off frequencies, respectively. At f_0, the resonator output reaches its maximum amplitude and the phase shift across the resonator is ideally -90º. However, the phase shift may be different from this value because of a distorted phase response generated by parasitic capacitive coupling between the integrated excitation and detection elements [63].

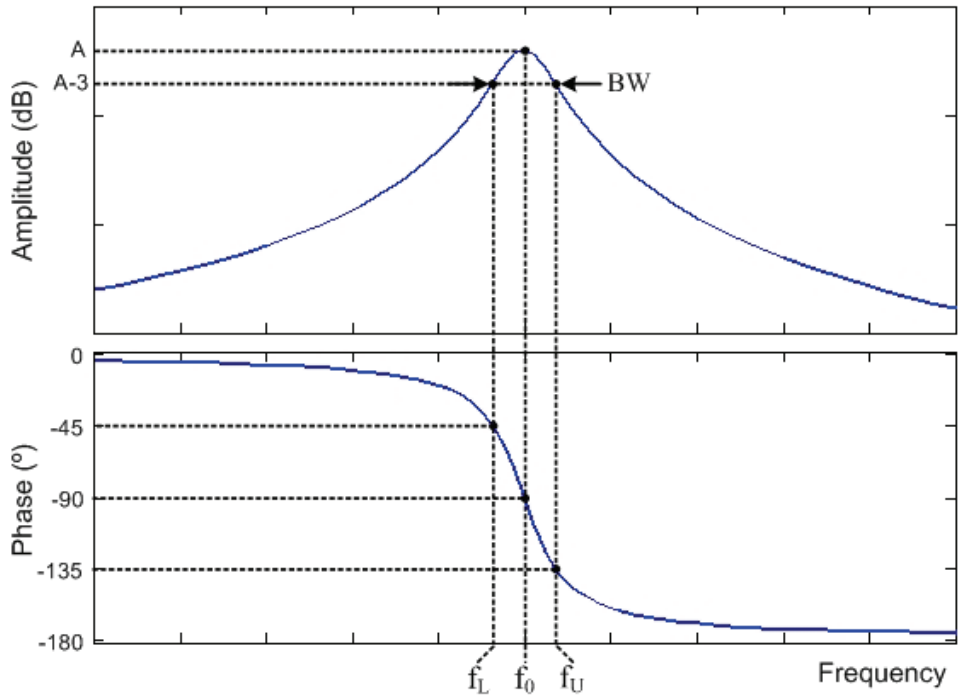

Figure 2.5: Typical transfer function of a resonator.

Although the transfer function analysis allows complete characterization of the resonator at different frequencies, the high cost associated with network analyzers as well as their large dimensions and low speed make this method impractical for portable chemical sensor systems.

Another open-loop interfacing technique is the slope detection method [64]. In this technique, a fixed frequency (f_S) signal source connected to the excitation element drives the resonator at or close to its resonance frequency f_0 as shown in Figure 2.6. In this case, the resonator oscillates at f_S with typical amplitude and phase responses given in Figure 2.7 (blue lines). When there is an external stimulus, e.g. a chemical analyte absorption in the sensitive coating, the resonance frequency shifts from f_0 to f_0'. Because of this frequency shift, there are changes in the amplitude (ΔA) and the phase ($\Delta\phi$) responses of the resonator as shown in Figure 2.7 (red lines), which are monitored as the sensor

outputs. A vector voltmeter can be used to detect these variations relative to the input signal source, or a phase detector together with a voltmeter can be utilized to detect only the phase variations.

Resonant sensors with phase output have been realized in earlier studies [65-67]. In another work, a portable vector voltmeter has been implemented and used in a SAW chemical sensor system to detect VOCs in the liquid phase [68].

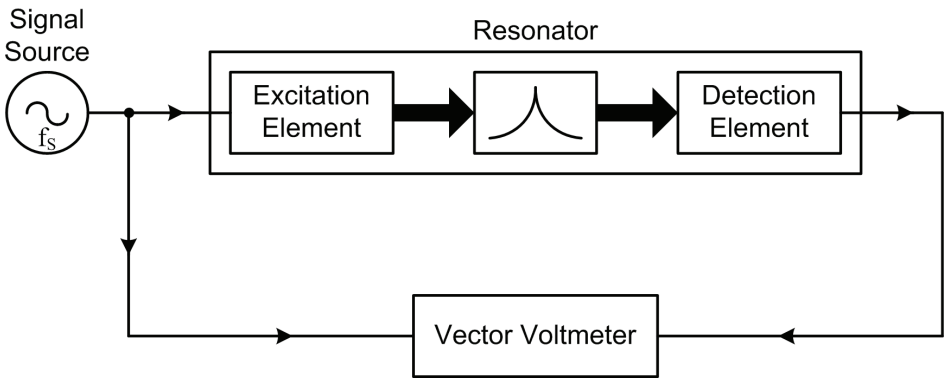

Figure 2.6: Schematic diagram of the slope detection method.

The slope detection method allows simultaneous measurement of the amplitude and phase responses of the resonator. However, since voltmeters are employed in these measurements, they provide lower resolution than frequency measurements because of the inherent lower resolution of voltage measurements [41, 69]. The need for a highly stable and precise signal source is another disadvantage of this method. Moreover, the dynamic range is limited to resonance frequency shifts smaller than the bandwidth of the resonance. Out of this range, the response becomes non-linear.

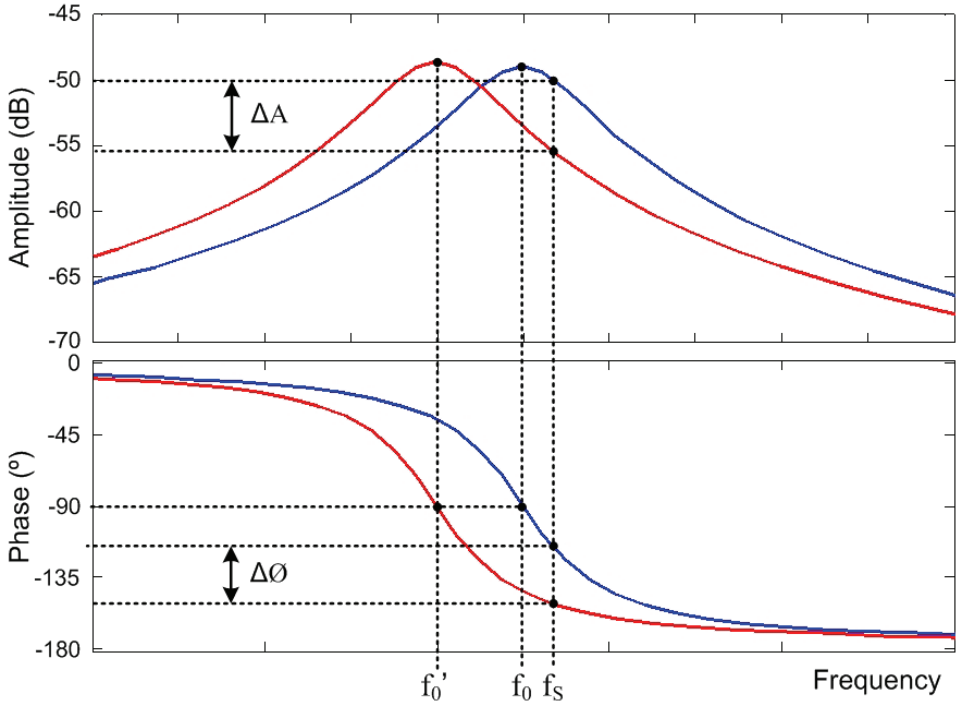

Figure 2.7: Amplitude and phase change in the slope detection method.

2.2.2 Closed-loop Methods

Closed-loop interfacing methods, such as self-oscillation and phase-locked loop (PLL) techniques, track changes in the resonance frequency of a resonant sensor and generate an excitation signal accordingly to sustain oscillation at the resonance frequency. In other words, a feedback control is used in both closed-loop methods.

The self-oscillation technique incorporates the resonator in an amplifying feedback loop as the frequency determining element. In this case, an excitation signal is generated from the output of the resonator by the feedback circuitry. This excitation signal is fed back to the resonator to form an oscillator. If the Barkhausen criteria are met, i.e. the loop gain is greater than unity and the total loop phase shift is 0º, the resonator will oscillate at its resonance frequency.

Figure 2.8 gives the schematic diagrams of two implementations of the self-oscillation technique with an amplitude limiter and an automatic gain controller (AGC). Both implementations include a phase shifter to ensure the 0º phase shift condition. In the implementation (i), the gain condition is fulfilled by an amplifier, and an amplitude limiter is included to regulate the amplitude for stable oscillation. On the other hand, an AGC provides both amplification and amplitude regulation in the implementation (ii). The AGC utilizes an additional feedback loop with a rectifier and a PI controller to adjust the gain of a variable-gain amplifier (VGA).

The self-oscillation technique has been used for atomic force microscopy (AFM) [64, 70] and for chemical sensing with SAW devices [71] and microcantilevers [58, 59].

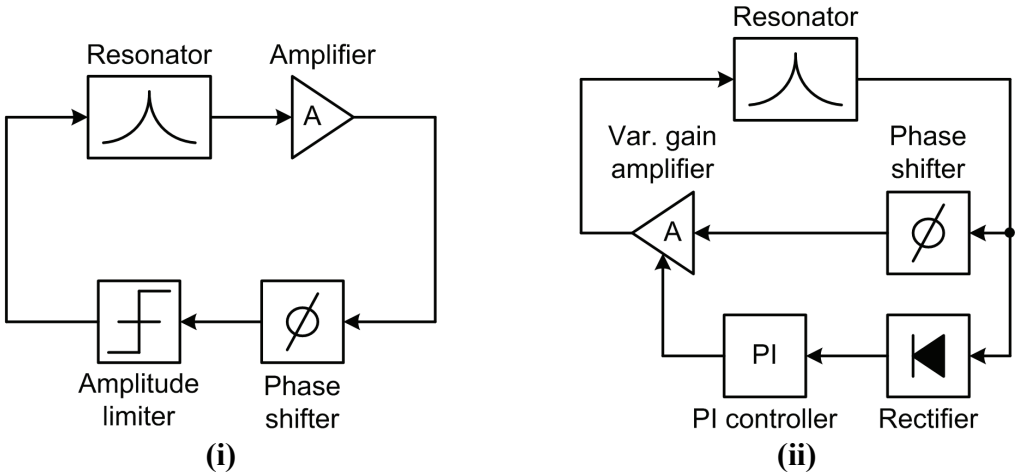

Figure 2.8: Schematic diagrams of two implementations of the self-oscillation technique with (i) an amplitude limiter and (ii) an automatic gain controller (AGC).

In the PLL technique, a resonator is again placed into a feedback loop as shown in Figure 2.9. Unlike the self-oscillation technique, a voltage-controlled oscillator (VCO) is employed to excite the resonator. The phases of the resonator and the VCO are compared by a phase detector (PD) that generates an output voltage proportional to their phase

difference. This output voltage from the PD is fed back to the VCO through a loop filter so that the VCO frequency is controlled to maintain a constant phase shift across the resonator and sustain oscillation at the resonance frequency. Because of the PLL characteristics, this constant phase shift can only be 0º or 90º. Therefore, a phase shifter may be included in the loop to account for possible additional phase shift generated by parasitic couplings. In addition, an amplifier is needed to amplify the low-amplitude output signal of the resonator.

The PLL technique has been used to detect interaction forces in scanning force microscopy (SFM) [72] and to detect mass changes with nanoelectromechanical resonators [73].

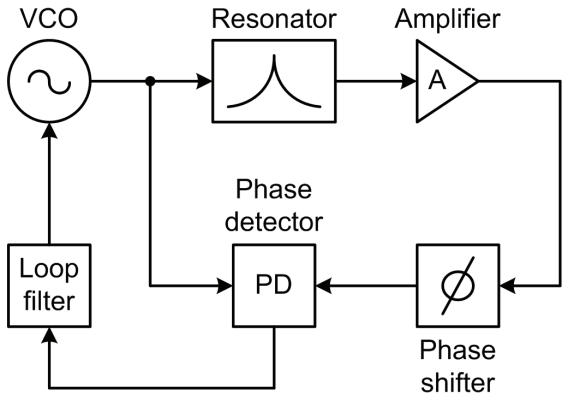

Figure 2.9: Schematic diagram of the PLL technique.

2.2.3 Comparison of Interfacing Methods and Conclusions

Closed-loop methods offer relatively simple and inexpensive circuit implementations, especially at low frequencies. Therefore, they provide superior solutions for portable sensor applications compared to the open-loop methods. Table 2.1 gives a comparison of the interfacing methods for resonant sensors.

Both closed-loop techniques show similar performances. However, the self-oscillation method offers a simpler implementation than the PLL method because of the need for a smaller number of components (e.g., the use of a VCO is avoided in the self-oscillation method). Therefore, the self-oscillation method has been used in this research. The next section explains the design basics of this method.

Table 2.1: Comparison of the interfacing methods for resonant sensors.

Method	**Open-Loop**		**Closed-Loop**	
	Transfer Function	**Slope Detection**	**Self-oscillation**	**PLL**
Information	Resonance Frequency, Q-factor, Amplitude, Phase	Amplitude, Phase	Resonance Frequency	Resonance Frequency
Resolution	Bandwidth Dependent	Bandwidth Dependent	+	+
Integration Compatibility	--	-	+	+
Cost	↑↑	↑	↓	↓

2.3 Oscillator Design Basics

An oscillator is a positive feedback system that amplifies a small initial fluctuation in the system, e.g. its own noise or the power supply turn-on transient, and eventually generates and sustains a periodic signal. Oscillators are essential components of electronic systems used especially in RF, communication, and instrumentation applications, where a reference frequency is needed. In most applications, a frequency-selective block is incorporated in the system to define the oscillation

frequency. The frequency-selective block can be a LC resonant circuit, a mechanical resonator such as quartz crystal resonator, or a dielectric resonator [74].

Figure 2.10 shows the block diagram of a feedback oscillator system where a feedback circuitry is interfaced with a resonator, which is used as the frequency-selective network. With transfer functions $R(\omega)$ and $F(\omega)$ associated with the resonator and the feedback circuitry, respectively, the transfer function of this closed-loop system can be written as

$$\frac{Vout}{Vin} = \frac{R(\omega)}{1 - R(\omega)F(\omega)} . \tag{2.2}$$

Self-oscillation at the resonance frequency ω_0 is sustained if the denominator of Eq. (2.2) vanishes, that is

$$R(\omega_0)F(\omega_0) = 1 . \tag{2.3}$$

This condition is the Barkhausen criterion and is satisfied if the loop gain is greater than or equal to unity, i.e.

$$\left|R(\omega_0)\right| \cdot \left|F(\omega_0)\right| \geq 1 , \tag{2.4}$$

and the total loop phase shift is 0º, i.e.

$$\phi_R(\omega_0) + \phi_F(\omega_0) = 0° , \tag{2.5}$$

where ϕ_R and ϕ_F are the phase shifts across the resonator and the feedback circuitry, respectively. To meet the gain and phase conditions given in the equations above, amplifiers and a phase shifter have to be included in the feedback circuitry.

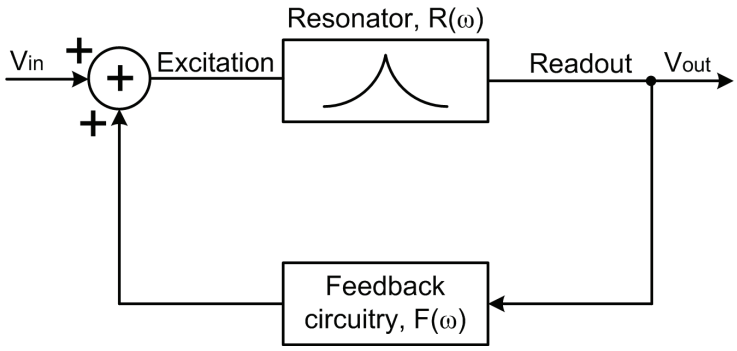

Figure 2.10: Block diagram of a feedback oscillator system with a resonator as the frequency-selective network.

2.3.1 Resonator

A mechanical resonator can be modeled as a second-order harmonic oscillator. In this case, the differential equation describing its force-deflection relation can be written as

$$m\ddot{x} + b\dot{x} + kx = F_e, \tag{2.6}$$

where m is the effective mass, b is the damping coefficient, k is the effective mechanical spring constant, x is the deflection, and F_e is the excitation force generated by the feedback circuitry. If the phase of the feedback circuitry is adjusted with a phase shifter to achieve a total loop phase close to 0º (satisfying Eq. (2.5)), the excitation force will be phase matched with the vibration velocity and is given by

$$F_e = b_e\dot{x}. \tag{2.7}$$

Then, the force-deflection relation becomes:

$$m\ddot{x} + (b - b_e)\dot{x} + kx = 0. \tag{2.8}$$

Equation (2.8) shows that the damping of the resonator can be compensated by the excitation force generated by the interface circuitry. As long as the magnitude of the

excitation force is kept high enough using amplifiers and overcomes the damping (satisfying Eq. (2.4)), self-oscillation at or close to the resonance frequency of the resonator is started. In this case, the resonance frequency is given by

$$f_0 = \frac{1}{2\pi}\sqrt{\frac{k}{m}}\,. \tag{2.9}$$

2.3.2 Gain Control

Even though amplifiers are essential to start self-oscillation, they are not enough to sustain stable oscillation at the resonance frequency. Initially, the loop gain has to be higher than unity to ensure oscillation start-up. In this case, the generated excitation force F_e is larger than the damping force, resulting in a deflection of the resonator. This deflection is converted into an electrical signal by the detection element of the resonator, then amplified by the amplifiers and fed back to the resonator. The excitation mechanism of the resonator converts this amplified signal and generates a larger excitation force, causing a larger deflection and so on. Because of this positive feedback in the loop, unless limited, the oscillation signal amplitude grows to levels that saturate the amplifiers, resulting in distortion. Similarly, if the oscillation amplitude decreases after start-up, the positive feedback will cause the excitation force and thus the deflection to decrease continuously until the oscillation disappears.

To prevent this instability, a gain control mechanism is needed to obtain a high loop gain at the start-up, while maintaining a reduced loop gain during the quasi-stationary phase. The gain control can be obtained with an amplitude limiter or an AGC as shown in Figure 2.8. Both of these have been implemented in this research and are further discussed in Chapter 4.

2.3.3 Phase Control

The phase condition in Eq. (2.5) determines the operating point, in other words, the oscillation frequency. Unless the phase of the feedback circuitry is exactly the same (with opposite sign) as the phase of the resonator at its resonance frequency, the oscillation frequency will be different from the resonance frequency.

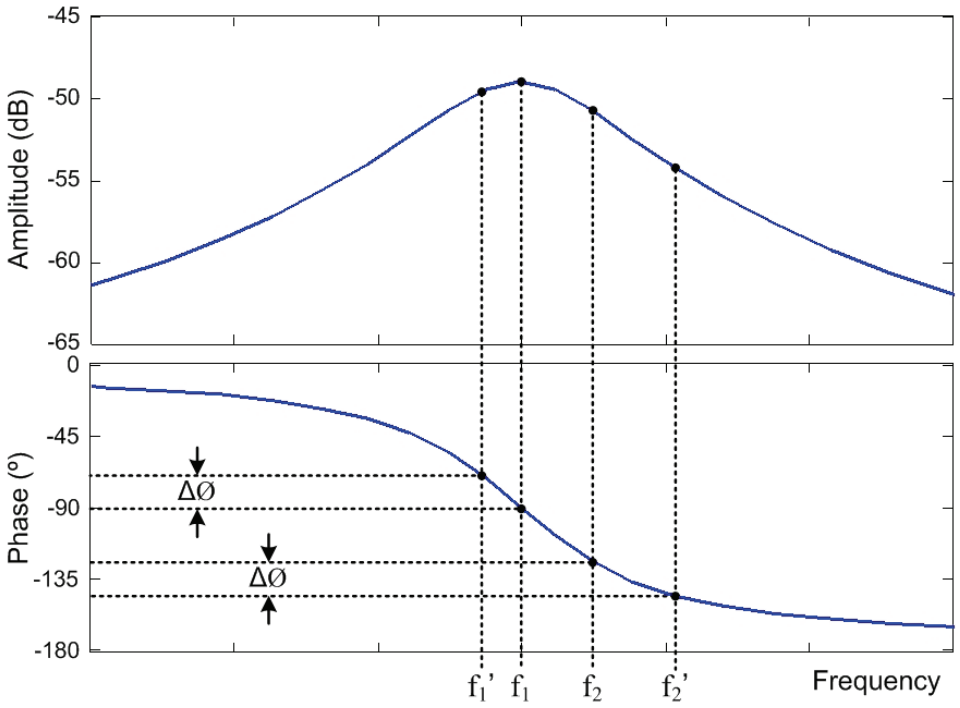

Figure 2.11: Amplitude and phase responses of a resonator.

The loop phase has to be adjusted to ensure an operating point as close as possible to the resonance frequency. This way, the SNR can be improved because of the larger output signal of the resonator at the resonance frequency. Also, the effects of phase variations on the oscillation frequency can be reduced because of the higher slope of the phase response at or close to resonance, resulting in improved frequency stability. To

explain this, the amplitude and phase responses of a resonator are given in Figure 2.11, where two different closed-loop oscillation frequencies, f_1 and f_2, are considered. If there is a constant phase variation of $\Delta\phi$ in the loop, f_1 and f_2 will shift to f_1' and f_2', respectively. The frequency variation is smaller for the operating point closer to the resonance frequency ($f_1 - f_1' < f_2' - f_2$), indicating less dependence on the phase variation.

2.4 Performance Parameters

The performance of a chemical sensor depends on a superposition of the sensitive layer and the transducer characteristics and the performance of the interface electronics. This section summarizes the performance parameters of a mass-sensitive chemical sensor utilizing the self-oscillation method.

2.4.1 Selectivity

Selectivity is the ability of a chemical sensor to detect the analyte of interest in a complex mixture with other analytes causing interference. High selectivity is required especially in environmental monitoring applications where many different chemical species are present. Therefore, chemical sensor research has been focused on obtaining higher selectivity over the last decades [75]. To improve selectivity, two different approaches, shown in Figure 2.12, have been used: (i) utilizing highly specific sensitive layers, and (ii) implementing sensor arrays comprising broadly tuned sensors [6].

In approach (i), the sensitive layer is so specific that it only responds to a single type of chemical analyte. A wide variety of materials have been tried to obtain this kind of perfect chemical recognition [4]. However, with few exceptions, implementing very selective materials is hard. Furthermore, highly selective materials are generally based on strong chemical interactions and do not allow for reversible chemical sensing needed in the majority of environmental applications.

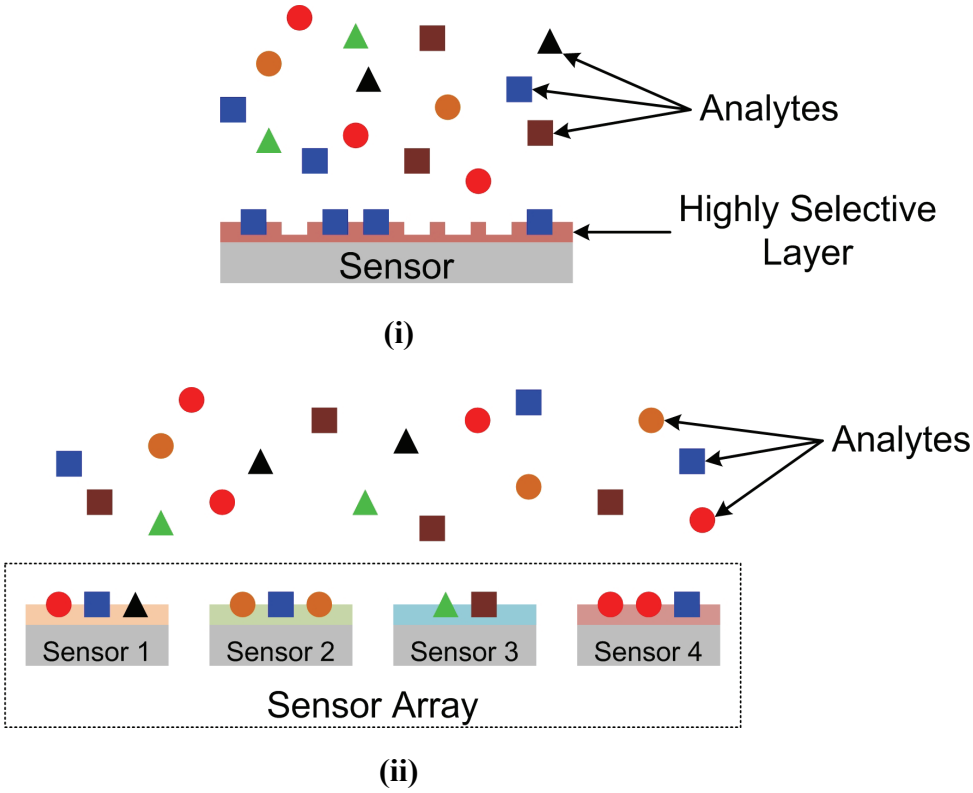

Figure 2.12: Approaches to improve selectivity: (i) utilizing highly specific sensitive layers, and (ii) implementing sensor arrays comprising broadly tuned sensors (modified from [6]).

The other approach to improve selectivity is to utilize sensor arrays where each sensor element is coated with a different sensitive layer that provides a different patterned response to a variety of analytes. In this case, instead of a single data point, multiple data points per analyte are acquired. In this way, additional chemical information is obtained, and selectivity is improved. In sensor arrays, increasing the number of elements results in increased selectivity. In spite of being superior and more flexible, this approach is more complex than approach (i), since it requires complicated pattern recognition algorithms and a higher number of sensor elements.

2.4.2 Sensitivity

The chemical sensor sensitivity is defined as the measured frequency change per analyte concentration (in units of Hz/ppm) and is given by [59]

$$S = \frac{df}{dc} = \frac{df}{d\rho_L} \cdot \frac{d\rho_L}{dc} = G \cdot S_A , \tag{2.10}$$

where f is the resonance frequency, c is the analyte concentration (in units of ppm), and ρ_L is the density of the sensitive layer. Here, the gravimetric sensitivity G depends on the mass-sensing capability of the transducer, and S_A depends on the sorption characteristics of the sensitive film, which is expressed by the partition coefficient. Equation (2.10) shows that the sensor sensitivity can be improved by using highly sensitive coatings, i.e. coatings, which absorb the analytes easily, resulting in a large density change. However, sensitive coatings are generally non-specific, that is, they are sensitive to more than one type of chemical species. Therefore, unwanted interactions with analytes other than the one to be detected are hard to avoid, i.e. cross-sensitivity is a challenge. Increasing G, the gravimetric sensitivity of the transducer, also improves the sensor sensitivity.

2.4.3 Frequency Stability

An oscillator is disturbed by inevitable processes such as random noises and drift caused by environmental effects and aging. Therefore, the frequency and amplitude of the output signal of an oscillator, even the most stable one, are not constant but vary in time. Fluctuations in the peak value of the signal result in amplitude instability. Since the amplitude control mechanism, i.e. amplitude limiter or AGC typically employed in oscillators reduces the amplitude fluctuations [76], and frequency is usually the output parameter in mass-sensitive sensors, the frequency stability is the major concern. The frequency stability can be investigated in two categories: short-term and long-term frequency stabilities.

The short-term frequency stability is a very important characteristic for chemical sensing applications, since it is directly related to the resolution of the sensor, in other words, the minimum detectable mass or analyte concentration change. Fluctuations in the phase (phase noise) cause instabilities of the zero crossings of the oscillator signal. This results in variations in the period of the oscillation and thus generates short-term frequency instability or in other words frequency noise. The sources of phase noise are the white and flicker noises of the resonator, detection element, and circuit blocks [77].

The relation between the phase variations, for instance in the circuitry $\delta\phi_F(f)$, and the frequency noise f_n can be calculated using the phase condition given in Eq. (2.5) as [77, 78]

$$f_n \approx f_0 \frac{\delta\phi_F(f)}{2Q}, \tag{2.11}$$

where Q is the Q-factor of the resonator and is given by [79]

$$Q = \frac{\sqrt{mk}}{b}, \tag{2.12}$$

where m is the effective mass, b is the damping coefficient, and k is the mechanical spring constant of the resonator. Equation (2.11) shows that increasing the Q-factor reduces the effect of the phase variation and hence results in lower frequency noise. The effect of the Q-factor on the frequency noise can be understood by examining Figure 2.13, which gives the amplitude and phase responses of two resonators with different Q-factors. Here, a phase variation of $\Delta\phi$ in the feedback loop will cause a phase variation of $-\Delta\phi$ in the resonator. This variation will result in a shift in the oscillation frequency. This frequency shift is lower for the resonator with higher Q-factor ($f_0 - f_F < f_0 - f_F'$), i.e. a higher Q-factor results in better frequency stability.

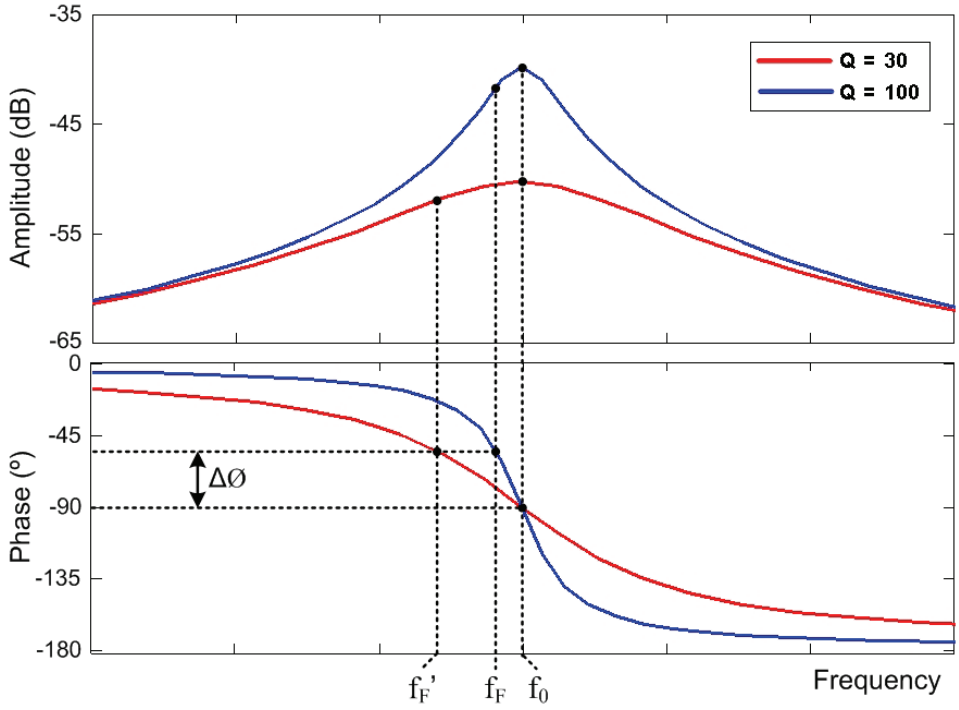

Figure 2.13: Amplitude and phase responses of two resonators with different Q-factors.

The frequency noise can be quantified in both frequency and time domains. In the frequency domain, it is described by a single-sided power spectral density (PSD). A number of models have been proposed to characterize this PSD. These models include the linear-time invariant Leeson's model [80], the linear-time variant-model [76], and empirical models showing the PSD as a sum of power-law spectral densities [81].

In the time domain, the Allan variance [82] is used. To estimate the Allan variance of an oscillator, the oscillation frequency is recorded with a counter at a sampling interval, called gate time τ. Then, the Allan variance, based on differences of two adjacent frequency measurements, is calculated as

$$\sigma^2(\tau,m)=\frac{1}{2m}\sum_{n=1}^{m}(\gamma_{n+1}-\gamma_n)^2\ ,\ \gamma_n=\frac{f_{n+1}-f_n}{f_n}, \tag{2.13}$$

where m is the number of measured data points. For the same oscillator, the PSD and Allan variance are related by [81]

$$\sigma^2(\tau) = 2\int_0^\infty S_y(f)\,|H(f)|^2\,df = 2\int_0^\infty S_y(f)\frac{\sin^4(\pi f\tau)}{(\pi f\tau)^2}df\,, \tag{2.14}$$

where $S_y(f)$ is the one-sided PSD of the frequency noise. In Eq. (2.14), the PSD is shaped with a filter function of $|H(f)|^2$ stemming from the averaging nature of the Allan variance.

Beside short-term variations, the frequency of an oscillator drifts with time and results in long-term frequency instabilities as mentioned before. The reasons for this drift include, but are not limited to, changes in the oscillator's environment, changes in the component characteristics of the oscillator, such as aging, and power supply changes, and low-frequency noise. The drift causes the Allan variance to increase with increasing gate time.

To explain how environmental variations affect the long-term frequency stability, the relative frequency change of a resonant structure is derived from Eq. (2.9) as

$$\frac{\Delta f}{f_0} = -\frac{1}{2}\frac{\Delta m}{m} + \frac{1}{2}\frac{\Delta k}{k}, \tag{2.15}$$

where Δf is the frequency change, Δm is the mass change, and Δk is the stiffness variation of the structure. As observed from Eq. (2.15), changes in mass and stiffness affect the resonance frequency of a microstructure. When the resonator is applied as a mass-sensitive sensor, the stiffness change (second term in Eq. (2.15)) is generally assumed to be negligible compared to the mass change. In this case, the frequency shift is only proportional to the adsorbed mass in the sensitive layer and is given by

$$\frac{\Delta f}{f_0} = -\frac{1}{2}\frac{\Delta m}{m}. \tag{2.16}$$

Nonetheless, environmental disturbances such as variations in temperature, humidity, atmospheric pressure, etc. and aging are also coupled to the resonance frequency shift by causing variations in the stiffness of the resonator, resulting in frequency drift. This frequency drift determines the long-term stability of the resonator and limits the resolution of mass-sensitive microsensors, especially in long-term

monitoring applications with slowly changing analyte signatures. Unfortunately, since the sensor has to be always in interaction with the environment to detect chemical analytes, it is hard to avoid this drift. Therefore, compensation techniques have to be utilized to reduce the stiffness-induced frequency changes. Otherwise, high sensor resolution cannot be achieved.

2.4.4 Limit of Detection

One of the most important performance parameters for a chemical sensor is the limit of detection (LOD). The LOD gives a measure of the minimum detectable analyte concentration or the sensor resolution. In other words, the sensor cannot detect analyte concentrations below the LOD. For mass-sensitive resonant sensors, the LOD (in units of ppm) is expressed by [59]

$$LOD = \frac{\Delta f_{\min}}{S} = 3\frac{\Delta f_n}{S}, \tag{2.17}$$

where S is the sensor sensitivity (see Eq. (2.10)), Δf_{min} is the minimum detectable frequency change, and Δf_n is the frequency output noise estimated by the Allan variance method described before. As seen from Eq. (2.17), the sensor sensitivity should be increased, and frequency noise should be decreased to improve the LOD.

To summarize the performance parameters, Figure 2.14 shows the recorded resonance frequency of a silicon-based resonant chemical sensor as a function of time during a gas-phase chemical measurement and a close-up view showing the short-term frequency fluctuations. Here, the resonator is coated with a chemically-sensitive polymer film, and different concentrations of various VOCs are periodically drafted onto the sensor. At every analyte injection, the frequency shifts down with a sharp transient. For each VOC, the sensor shows a different frequency change. In other words, the sensitivity of the sensor and therefore the LOD for each VOC is different. In approximately 7 hour measurement time, the frequency drifts around 100 Hz, which limits the long-term

frequency stability. In an uncontrolled environment, it would be hard to describe this slow frequency change as drift, since analytes with slowly changing concentrations might generate the same effect. Furthermore, the close-up view shows the instantaneous fluctuations in the frequency. These fluctuations are frequency noise and determine the short-term frequency stability.

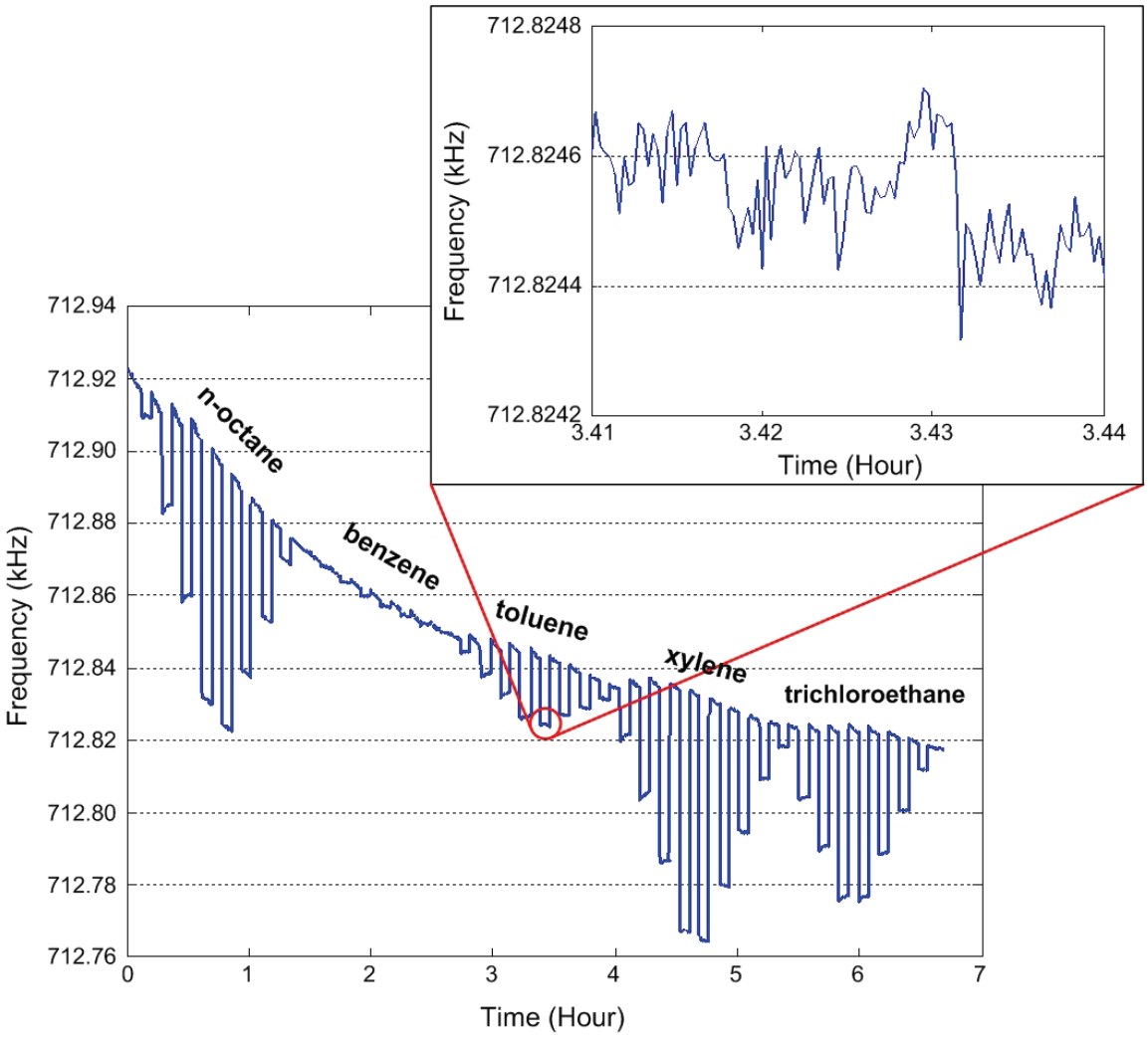

Figure 2.14: Recorded resonance frequency of a silicon-based resonant chemical sensor as a function of time during a gas-phase chemical measurement and close-up view showing short-term frequency fluctuations.

2.5 Integration Considerations

The resolution, stability and sensitivity of a chemical sensor system can be dramatically improved by proper integration of the sensor and the interface circuitry. Methods of integration have to be considered early in the microsystem development to achieve effective and simple packaging. The most commonly used integration method is the hybrid connection of the CMOS-integrated interface circuitry to a sensor chip via wire bonding (see Figure 2.15). Even though this method is easy to implement and allows system modularity, low-level signals from the sensor are affected by noise and electromagnetic interference because of relatively long interconnect wires. Also, the hybrid technique is not practical for interfacing sensor arrays with many inputs/outputs (I/Os).

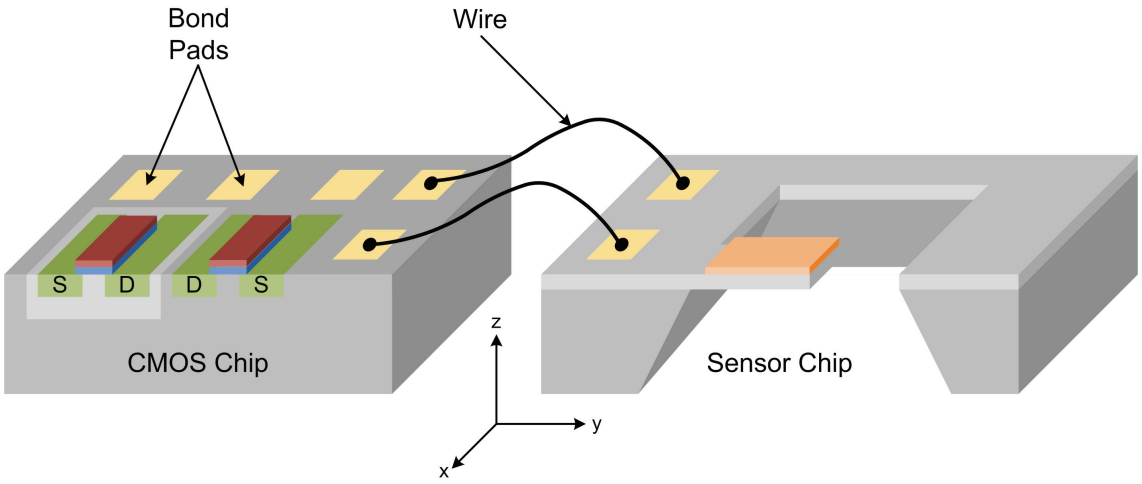

Figure 2.15: Hybrid connection of the interface circuitry implemented on a CMOS chip to a sensor chip via wire bonding.

To reduce the interconnect parasitics, closer integration methods have to be used. These methods include [83]: (i) integration of the sensor on top of the CMOS chip,

(ii) lateral integration of the sensor and the circuitry on the same substrate, and (iii) vertical integration of the sensor chip on top of the CMOS chip via flip-chip bonding (see Figure 2.16). Methods (i) and (ii) require fabrication compatibility between the sensor and CMOS chips. Because of this compatibility issue, compromises have to be made in both the sensor and circuit designs. In addition, lateral integration (method (ii)) can be inefficient in terms of real estate since the sensor and especially sensor arrays might consume substantial CMOS surface area.

On the other hand, vertical integration with flip-chip bonding provides fabrication flexibility. Since CMOS and sensor chips are fabricated separately and bonded via chip-bonding techniques in this method, the most suitable fabrication technology can be utilized for each chip. This way, the requirement for fabrication compatibility between the sensor and CMOS chips can be avoided. Moreover, this method allows individual testing of the sensor and CMOS chips and thus simplifies testing procedures. Also, bonding only pre-tested and known to work chips increases system yield. Furthermore, this approach offers modular systems in which different sensor designs can be assessed by bonding them to a standardized CMOS chip with the necessary circuitry. Because of these advantages, the vertical integration method allows for a cost-effective microsystem implementation.

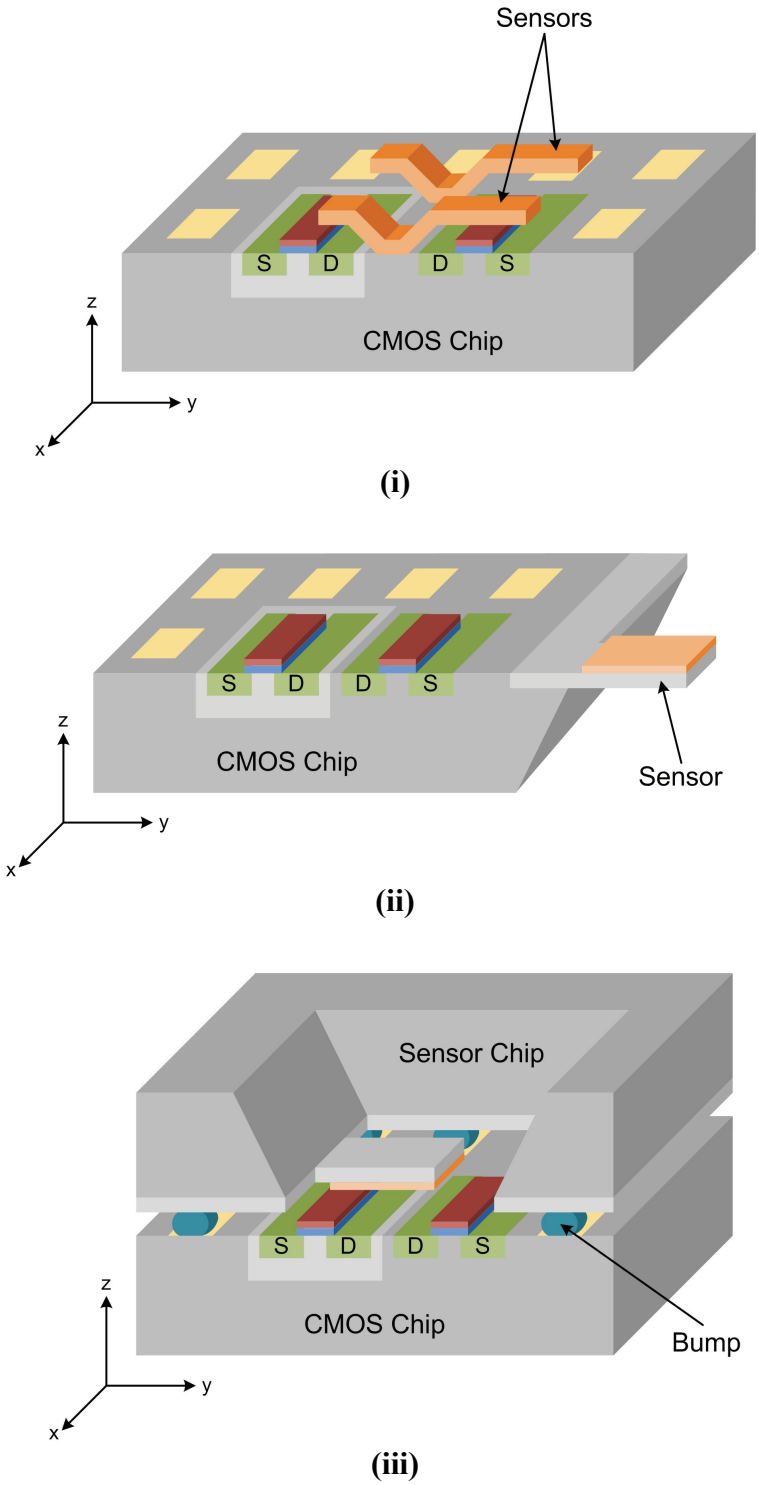

Figure 2.16: Possible methods for close integration of sensor and CMOS chips: (i) integration of sensor on top of CMOS chip, (ii) lateral integration of sensor and circuitry on the same substrate, and (iii) vertical integration of sensor chip on top of CMOS chip via flip-chip bonding.

CHAPTER 3

SILICON-BASED CHEMICAL MICROSYSTEM OVERVIEW

The chemical microsystem implemented in this research is based on the integration of a silicon-based resonant microstructure and a CMOS application-specific integrated circuit (ASIC). The resonant microstructure is the transduction element in the system, and the CMOS ASIC includes the sensor interface electronics.

This chapter provides an overview of the implemented microsystem. First, the resonant microstructures used in this work are presented, and their integrated excitation and detection mechanisms are explained. Then, the subsystems of the interface electronics are described.

3.1 Silicon-based Resonant Microstructures

Two types of resonant microstructures are used in this research: cantilever [34] and disk-shape resonators [35]. Figure 3.1 shows SEM images of these resonant microstructures, which are fabricated using a CMOS-compatible fabrication process with crystalline silicon being the main structural material. In addition, silicon dioxide and silicon nitride films are used for insulation and passivation.

To operate the microresonators at their resonance frequencies, integrated excitation and detection elements have been incorporated. Because of its simplicity and efficiency, an electrothermal excitation mechanism has been implemented using diffused heating resistors. These resistors are placed such that the fundamental in-plane vibration mode can be excited most efficiently (see FEM simulation results showing the total displacements in Figure 3.2). In this case, the microresonators primarily shear the surrounding media instead of compressing it; hence, the viscous damping is reduced

compared to the more common out-of-plane vibration modes. Therefore, in-plane-mode operation results in improved Q-factors and thus improved short-term frequency stabilities compared to operation in out-of-plane modes.

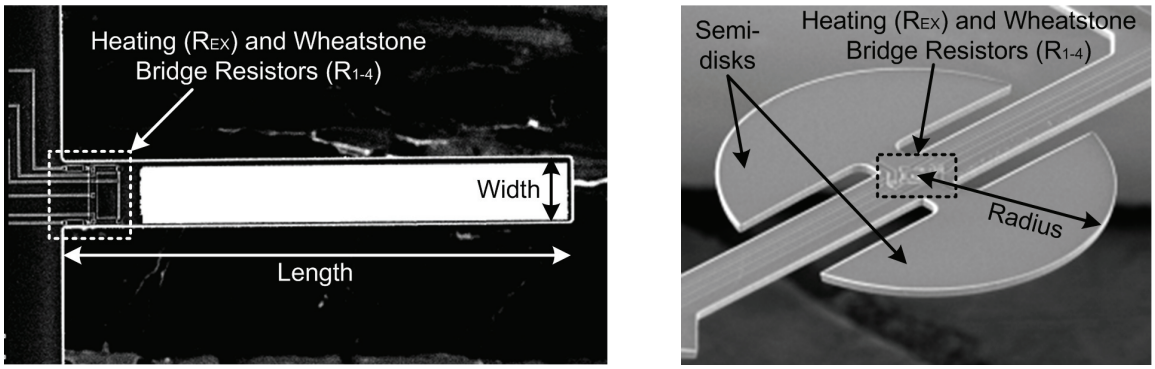

(i) **(ii)**

Figure 3.1: SEM images of the (i) cantilever and (ii) disk-shape resonant microstructures.

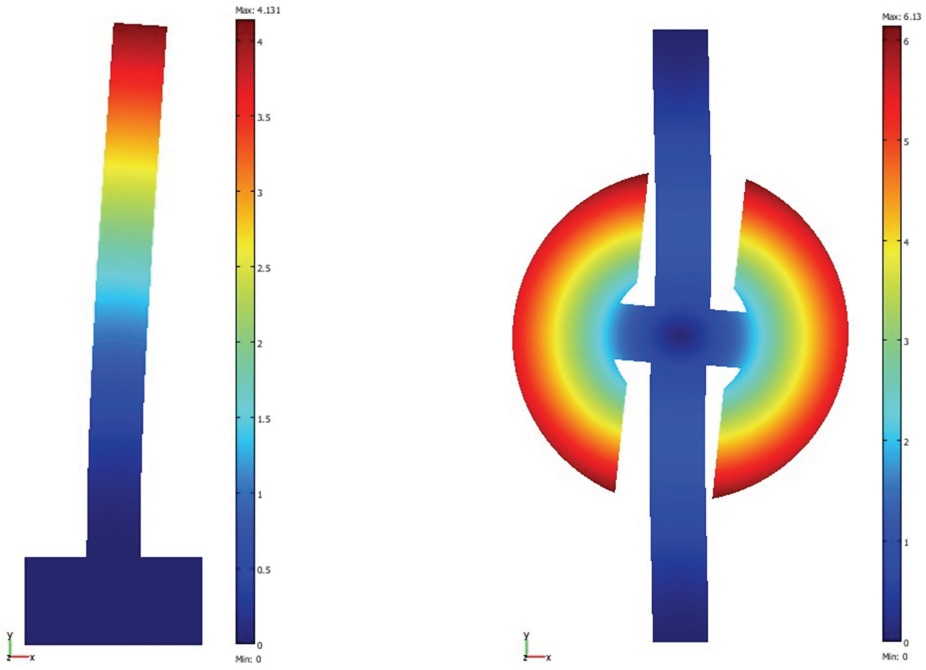

(i) **(ii)**

Figure 3.2: FEM simulation results showing the desired in-plane mode shapes of a (i) cantilever and a (ii) disk-shape microresonator. The color coding represents the total displacement.

To sense the microresonator vibration, silicon piezoresistors arranged in a Wheatstone bridge configuration are used as detection elements. To obtain maximum piezoresistive sensitivity and efficiently suppress out-of-plane modes, the piezoresistors are placed at the clamped end of the cantilever and at the center of the anchor beam of the disk-shape microresonators, where the stress due to vibrations is the highest.

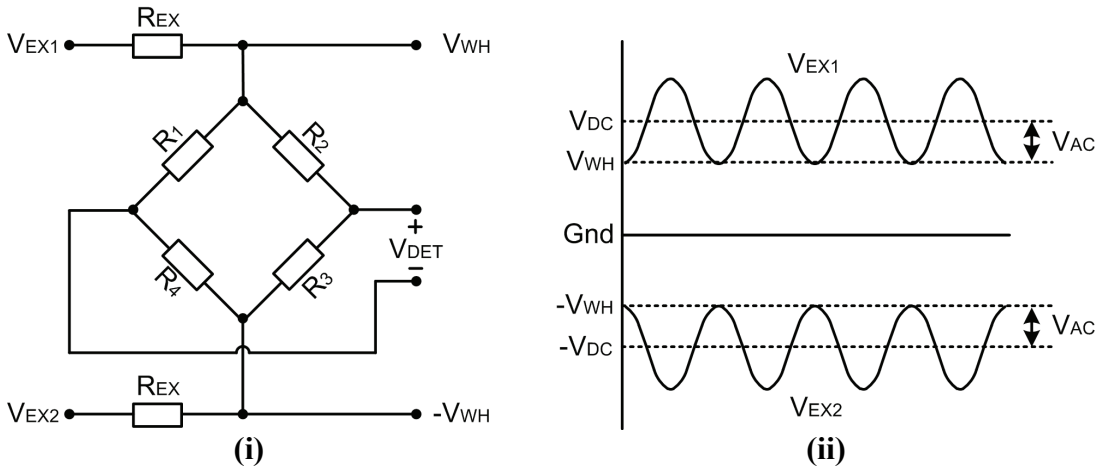

Figure 3.3: (i) Schematic diagram of the excitation and detection elements of the microresonators and (ii) out-of-phase excitation signals (V_{EX1} and V_{EX2}).

Figure 3.3 (i) shows the schematic diagram of the excitation and detection elements of the microresonators. Here, R_{EX} are the heating resistors, and $R_{1\text{-}4}$ are the Wheatstone bridge resistors. To actuate the disk-type microresonators at their fundamental in-plane resonance frequencies, out-of-phase AC signals superimposed on DC offsets (V_{DC} and $-V_{DC}$) have to be applied to the heating resistors as excitation signals (V_{EX1} and V_{EX2}), as shown in Figure 3.3 (ii). In the case of cantilevers, only one heating resistor is used. With the superimposed DC offset, the excitation signal and the heating power generated on a heating resistor are, respectively, given by

$$V_{EX} = V_{DC} + V_{AC}\cos\omega t\,, \tag{3.1}$$

$$P = \frac{V_{EX}^{\,2}}{R_{EX}} = \frac{V_{DC}^{\,2}}{R_{EX}} + \frac{V_{AC}^{\,2}}{2R_{EX}} + \frac{2V_{DC}V_{AC}}{R_{EX}}\cos\omega t + \frac{V_{AC}^{\,2}}{2R_{EX}}\cos 2\omega t\,. \tag{3.2}$$

The first two terms in Eq. (3.2) constitute the static heating power resulting in a static temperature elevation in the microstructure. The desired dynamic heating power component at the excitation frequency ω is the third term in Eq. (3.2), which is directly proportional to the applied DC offset. Therefore, the effect of the unwanted dynamic power component at the frequency of 2ω (fourth term in Eq. (3.2)) can be reduced by increasing the DC offset ($V_{DC} > V_{AC}$).

The Wheatstone bridge is biased with DC voltages V_{WH} and $-V_{WH}$ as shown in Figure 3.3 (i). The deflection of the microresonator results in an opposite-sign resistance change in the two diagonal resistor pairs of the Wheatstone bridge. In other words, when the resistances of R_1 and R_3 increase, the resistances of R_2 and R_4 decrease, or vice versa. Assuming matched resistors with a resistance of R, the resulting differential output voltage is given by

$$V_{DET} = 2V_{WH}\frac{\Delta R}{R}\,, \tag{3.3}$$

where ΔR is the resistance change in each resistor as a result of the deflection of the microstructure. The differential read-out mechanism doubles the output voltage compared to that of a single-ended counterpart, while canceling out any common-mode resistance change originating from, e.g., environmental effects, such as temperature variations. On the other hand, a perfect matching of the Wheatstone bridge resistors is impossible; hence, an offset voltage at the output is inevitable and has to be taken into account in the design of the interface electronics.

To be able to properly design the interface electronics, open-loop transfer characteristics of the microresonators are examined. For open-loop characterization, DC offset voltages are added to the AC excitation signals generated by a network analyzer

(Agilent 4395A) and applied to the heating resistor(s) of the microresonator. The Wheatstone bridge is biased and the differential output voltage of the Wheatstone bridge is converted into a single-ended signal by using a buffer amplifier. The buffered signal is connected back to the network analyzer to obtain the open-loop transfer characteristic of the microresonator. Figure 3.4 shows typical measured amplitude and phase transfer characteristics of a disk-type microresonator. The amplitude response varies with the device dimensions and Wheatstone bridge bias voltage. In other words, the signal attenuation by the microresonators is not constant. In addition, the phase response usually shows deviations from the theoretical value of -90º at the resonance frequency and varies from resonator to resonator, because of fabrication-induced variations and parasitic couplings between the excitation and detection elements [63].

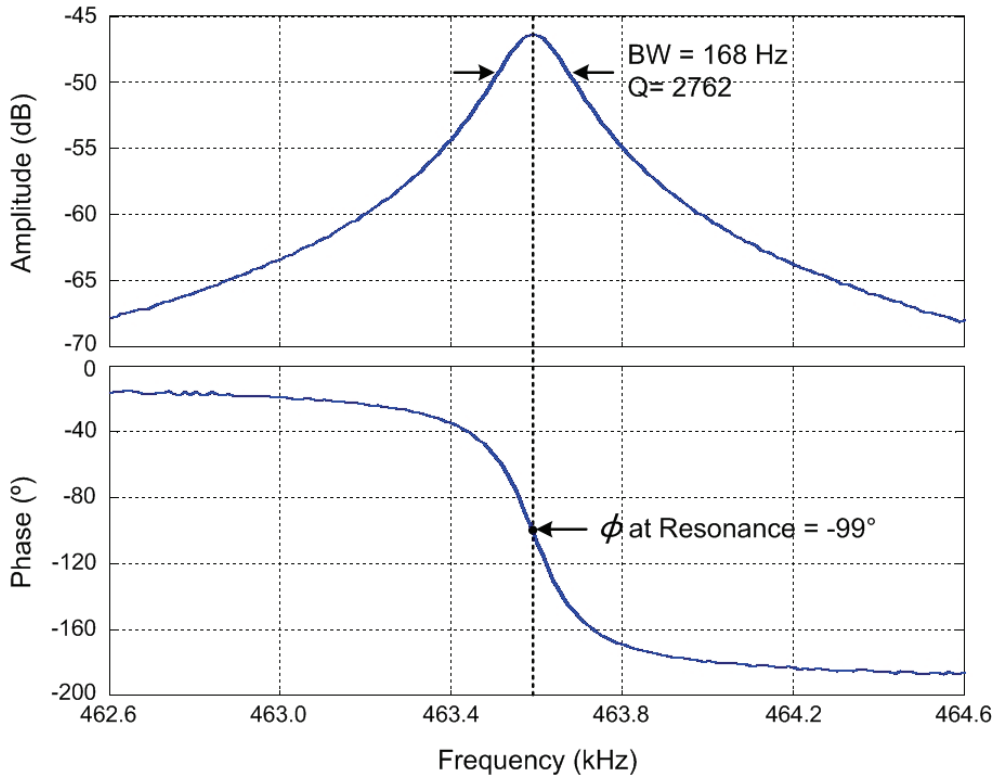

Figure 3.4: Typical measured amplitude and phase transfer characteristics of a disk-type microresonator.

Table 2.1 summarizes the key mechanical and electrical parameters of the microresonators that can be used in chemical sensing measurements.

Table 3.1: Key mechanical and electrical parameters of the microresonators that can be used in chemical sensing measurements.

<table>
<tr><th rowspan="2">Parameter</th><th colspan="4">Value</th></tr>
<tr><th colspan="2">Cantilever Resonator</th><th colspan="2">Disk-type Resonator</th></tr>
<tr><td rowspan="3">Device Dimensions</td><td>Width</td><td>45 – 90 μm</td><td>Radius</td><td>120 – 150 μm</td></tr>
<tr><td>Length</td><td>0.2 - 1 mm</td><td rowspan="2">Thickness</td><td rowspan="2">5 - 20 μm</td></tr>
<tr><td>Thickness</td><td>5 - 20 μm</td></tr>
<tr><td>Resonance Frequency</td><td colspan="2">100 kHz – 1 MHz*</td><td colspan="2">200 kHz – 1 MHz</td></tr>
<tr><td>Q-factor (in air)</td><td colspan="2">800 – 4200</td><td colspan="2">1500 – 5800</td></tr>
<tr><td>Attenuation (in air)</td><td colspan="4">40 – 80 dB</td></tr>
<tr><td>Heating Resistance R_{EX}</td><td colspan="4">400 – 600 Ω</td></tr>
<tr><td>Wheat. Bridge Resistance $R_{1\text{-}4}$</td><td colspan="4">400 – 600 Ω</td></tr>
<tr><td>Wheatstone Bridge Bias V_{WH}</td><td colspan="4">1 – 1.5 V</td></tr>
<tr><td>DC Offset V_{DC}</td><td colspan="4">1.5 – 4.5 V</td></tr>
<tr><td>AC Excitation Amplitude V_{AC}</td><td colspan="4">0.2 – 1 V</td></tr>
</table>

* Fabricated cantilevers exhibit resonance frequencies up to 2.2 MHz. Beyond 1 MHz, the cantilevers show very high attenuation and therefore are not used in closed-loop operation.

For array operation, a sensor chip includes eight microresonators as shown in Figure 3.5. Four of these microresonators are wire bonded in a 28-pin DIL package and therefore, four microresonators can be operated at a given time.

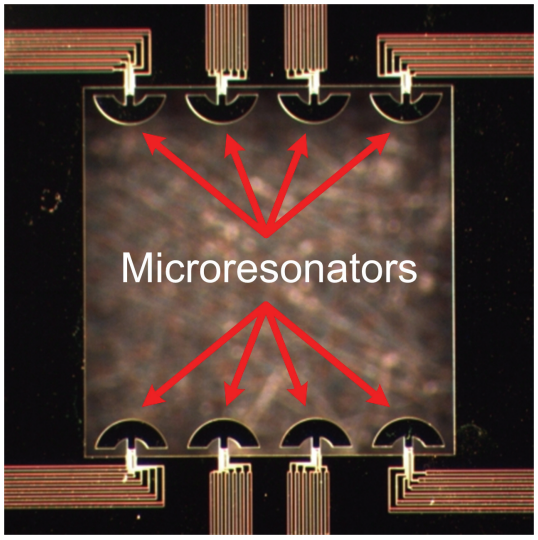

Figure 3.5: Micrograph of the sensor chip including eight microresonators.

3.2 Description of Electronic System

Interface circuits can be realized using off-chip general purpose ICs. Although these ICs can show high performance in terms of noise and speed, they increase the system size and might consume high power. In contrast, system size can be reduced by implementing an ASIC that includes all necessary circuitry on a single chip. In this way, each circuit block can be designed optimally to improve the system performance and reduce power consumption. Therefore, ASICs are more suitable for portable sensor systems than off-chip ICs.

In this work, two different CMOS-integrated ASICs have been implemented. The basic functionality of both designs is similar. However, by the addition of several control circuitries, the second design, ASIC_v2, has been improved based on the findings from the first design, ASIC_v1, to obtain improved frequency stability and lower power consumption. Figure 3.6 shows the micrographs of the fabricated CMOS chips, ASIC_v1 and ASIC_v2. ASIC_v1 has been fabricated using the AMIS 0.5µm 3M2P CMOS process and measures 2700 µm x 1850 µm. Besides, ASIC_v2 has been using the TI

0.35µm 4M2P BiCMOS technology, and the chip size is 2500 µm x 1500 µm. This thesis focuses on ASIC_v2, but compares the two chips where different circuit topologies have been used to obtain the same functionality.

Figure 3.7 shows the schematic diagram of the integrated CMOS interface and control electronics in ASIC_v2. The shaded blocks in this figure have been implemented off-chip. ASIC_v2 includes several closed-loop interface and control blocks to not only start and sustain the oscillation of the microresonator, but also improve the performance of the overall chemical microsystem. These blocks are briefly described in the following sections. (A detailed description of the circuitry is found in Chapter 4.)

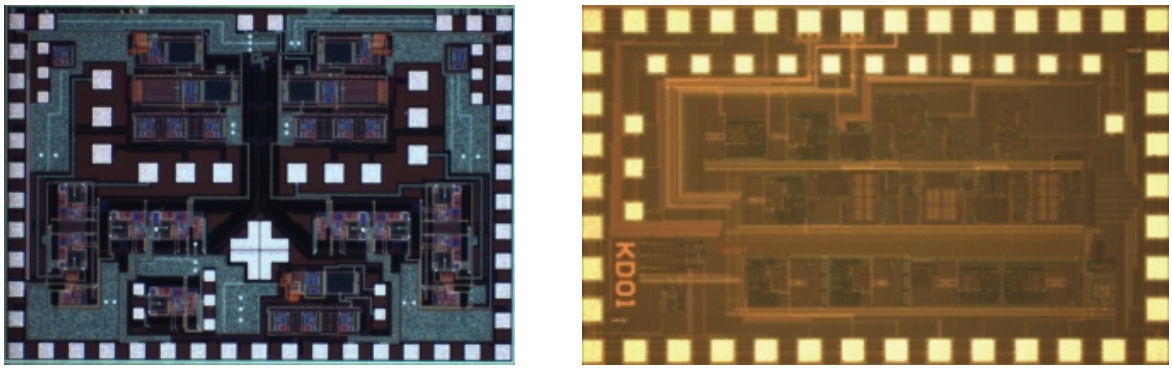

(i) **(ii)**

Figure 3.6: Micrographs of the fabricated CMOS chips, (i) ASIC_v1 and (ii) ASIC_v2.

3.2.1 Main Feedback (MF) Loop

The main feedback (MF) loop is responsible for generating the excitation signals to start and sustain self-oscillation of the resonator with an oscillation frequency at or close to the (in-plane) resonance frequency of the resonator. To do this, the feedback circuitry amplifies and phase shifts the signal from the resonator and then feeds this processed signal back to the resonator.

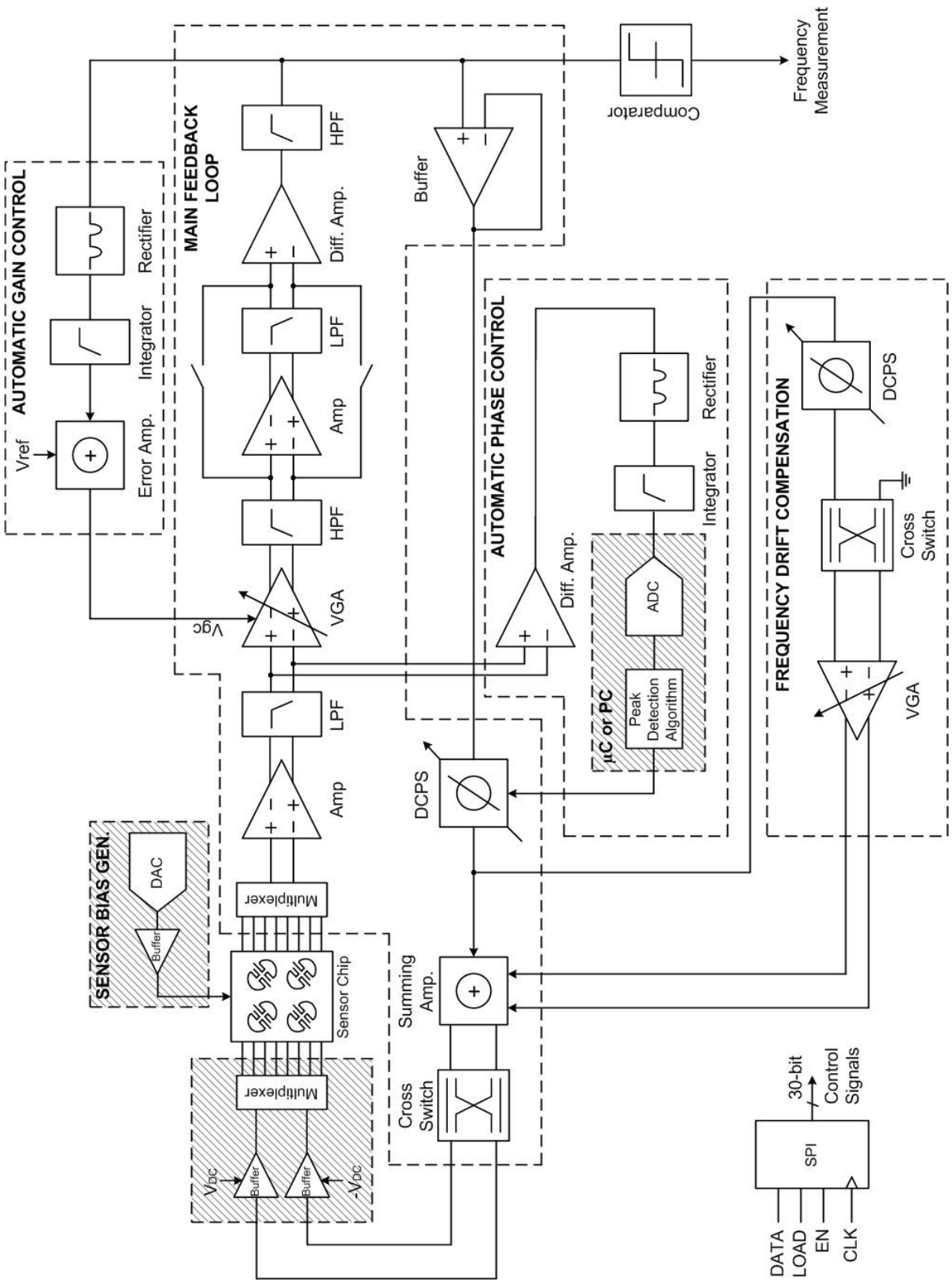

Figure 3.7: Schematic diagram of the integrated CMOS interface and control electronics.

For amplification, the MF loop includes a series of gain stages to obtain an overall loop gain greater than or equal to unity. Since the attenuation of the microresonator is not constant but varies from design to design, the gain provided by the gain stages has to be variable. Table 3.1 shows that the signal attenuation by the resonators ranges between 40 dB and 80 dB. Thus, in total, the gain stages have to provide a maximum amplification of 80 dB with a tunable range of 40 dB.

Another important point in the MF loop operation is the phase adjustment. Proper phase adjustment is very critical in starting and sustaining self-oscillation. The phase shift at the resonance frequency varies from resonator to resonator. In addition, the circuit blocks in the MF loop might also add a phase shift and change the total-loop phase. Therefore, a phase shifter is included to ensure a total loop phase of 0º and obtain an operating point as close as possible to the resonance frequency.

3.2.2 Automatic Gain Control (AGC) Loop

In feedback circuitry design, sustaining a stable self-oscillation is as prominent as starting it. A stable oscillation is obtained by controlling the amplitude of the oscillation. Without an amplitude control, the positive feedback introduced by the MF loop will cause the oscillation amplitude either to increase to levels that saturate the amplifiers, resulting in distortion or to decrease until the oscillation disappears. Therefore, ASIC_v2 uses an AGC loop to maintain a stable oscillation amplitude. The AGC loop monitors the oscillation amplitude in the MF loop and accordingly adjusts the gain of a variable-gain amplifier (VGA) in the MF loop to keep the oscillation amplitude constant.

3.2.3 Automatic Phase Control (APC) Loop

As mentioned before, proper phase control is very important in achieving better frequency stability and hence better resolution. ASIC_v2 incorporates an automatic phase

control (APC) loop to adjust the loop phase and ensure an operating point as close as possible to the resonance frequency. As the operating point approaches the resonance frequency with the phase adjustment, the oscillation amplitude increases (see Figure 3.4). Therefore, to sustain oscillation at the resonance frequency, the APC loop monitors the oscillation amplitude and tunes the phase in the MF loop with the phase shifter until a maximum amplitude is obtained.

3.2.4 Frequency Drift Compensation (FDC) Loop

The resonance frequency of a microresonator is affected by changes in its mass and stiffness as described in Chapter 2. If the microresonator is used as a mass-sensitive sensor, stiffness-induced resonance frequency changes caused by environmental disturbances and aging have to be compensated for to obtain a high sensor resolution by improving the long-term frequency stability. ASIC_v2 uses a controlled stiffness modulation generated by a frequency drift compensation (FDC) loop to achieve this compensation. Thereby, the FDC loop tracks the resonator's Q-factor, which is solely obtained from frequency measurements without need for additional sensing devices. The measured Q-factor is then used to compensate for the frequency drift using the relation between Q-factor and resonance frequency obtained through an initial calibration step.

CHAPTER 4

INTEGRATED INTERFACE AND CONTROL ELECTRONICS

The operation of the integrated electronics (see Figure 3.7) can be explained as follows: one of the four microresonators on the sensor chip is selected and connected to the CMOS ASIC by using the input multiplexer. The piezoresistive Wheatstone bridge of the selected microresonator is biased by an off-chip bias circuitry composed of a digital-to-analog converter (DAC) and a buffer amplifier. A series of four gain stages amplifies the readout signal from the Wheatstone bridge. The AGC circuit controls the gain of the 2nd gain stage to maintain a stable oscillation amplitude. Low-pass filters (LPFs) after the 1st and 3rd gain stages reduce high-frequency signal coupling into the bandwidth (BW) of interest. High-pass filters (HPFs) are also implemented after the 2nd and 4th gain stages to remove any DC offset and flicker noise of these gain stages. The amplified and filtered signal is then fed to a phase shifter. The APC circuit controls the phase shifter and tunes the phase until a maximum oscillation amplitude is achieved. The gain stages and the phase shifter are used to ensure that the overall system acts as a positive feedback loop at or close to the resonance frequency. The phase-tuned signal is then applied to a summing amplifier. The summing amplifier adds the signals from the MF loop and the FDC circuit. The FDC circuit is used to compensate for the frequency drift caused by environmental disturbances. A cross-switch implemented after the summing amplifier changes the polarity of the excitation signals if needed. Thereafter, DC-offset voltages are added to the excitation signals by summing amplifiers implemented with off-chip components. The excitation signals are then applied to the heating resistors. A comparator is also included to convert the sine-wave oscillation signal into a square-wave signal so that it can be directly interfaced to a frequency

counter. As power supply voltages, ±1.65 V are selected. The common-mode voltage (V_{cm}) in the entire system is 0 V.

The following sections describe each block of the integrated electronics in detail and provide simulation and measurement results.

4.1 Gain Stages

When the microresonator is oscillating at its resonance frequency, the Wheatstone bridge resistances are modulated proportional to the vibration amplitude. This resistance modulation unbalances the bridge, causing a low-amplitude differential voltage across the bridge. This differential voltage is the output signal of the resonator to be detected and is amplified by the four gain stages of ASIC_v2 to start oscillation by overcoming the attenuation of the resonator. Since the resonance frequency is different for different resonators, the 3-dB bandwidth of the gain stages have to be at least 1 MHz (the highest sensor operation frequency) to make the amplification independent of the resonator used.

One of the most widely used amplifier types for interfacing a Wheatstone bridge output is the instrumentation amplifier (in-amp) consisting of three operational amplifiers (op-amps) [84], which is utilized as the 1st gain stage in ASIC_v1 [85]. The 3-op-amp in-amp uses a closed-loop amplifier topology in which resistors are employed to set the gain by a negative feedback. Typically, the op-amps of the in-amp include more than one stage to both increase the open-loop gain and be able to drive the feedback resistors. This multi-stage architecture of the op-amps results in a multi-pole frequency response that limits the 3-dB bandwidth of the op-amps at a given power consumption. Furthermore, the in-amp may suffer from stability problems that can occur because of insufficient phase margin (PM) of the op-amps. On the contrary, the negative feedback in the closed-loop topology improves the gain linearity of the 3-opamp in-amp and makes its gain less sensitive to variations in temperature, active device operating conditions, and transistor parameters [86, 87]. However, since the output signal of the implemented

microsystem is a frequency and not a voltage, variations and nonlinearity in the gain of the amplifiers are not very critical and are compensated with the AGC circuit. Therefore, open-loop amplifiers are implemented in the first three gain stages of the ASIC_v2 to obtain the necessary 3-dB bandwidth with lower power consumption and overcome possible stability problems.

Fully-differential amplifiers offer higher SNR because of their larger output voltage swing and are less susceptible to common-mode noise than their single-ended counterparts [86, 88]. Therefore, unlike for ASIC_v1, a fully-differential topology is employed in the first three gain stages of ASIC_v2, where the signal amplitude is low and thus more vulnerable to noise.

4.1.1 First Gain Stage

Fabrication-induced mismatches between the Wheatstone bridge resistors result in a DC-offset component added to the low-amplitude differential AC readout signal of the resonator. In addition, CMOS amplifiers suffer from input offset voltages originating from mismatches in their device parameters. As a result, the offset voltage at the input of the 1st gain stage is on the order of tens of millivolts, which reduces the dynamic range or even can saturate the amplifier. Therefore, an offset compensation technique has to be employed.

Various offset compensation techniques including auto-zeroing and chopping have been proposed in the literature [89, 90]. Although these techniques reduce the input-referred amplifier offset to microvolt levels, they do not compensate for the offset voltage of the sensor and also require relatively complicated and area- and power-consuming circuitry.

Figure 4.1 presents the block diagram of the 1st gain stage showing the concept of the implemented offset compensation method [91, 92]. In this method, the output signal of the main amplifier is low-pass filtered to extract the low-frequency component of the

signal. This low-frequency signal is then amplified by an auxiliary amplifier to generate an error signal proportional to the total offset voltage at the output of the main amplifier. This error signal is connected to the nulling port to cancel the offset voltage at the main amplifier input. With this closed-loop operation, both amplifier and sensor offsets can be compensated without disturbing the high-frequency sensor signal.

In this topology, the main amplifier determines the high-frequency characteristics of the gain stage. In contrast, the offset compensation loop comprising the LPF, the auxiliary amplifier, and the nulling port forms a low-frequency path and determines the low-frequency characteristics. Since this loop cannot distinguish low-frequency (1/f) noise from offset, the implemented offset compensation method also shapes the 1/f noise of the main amplifier.

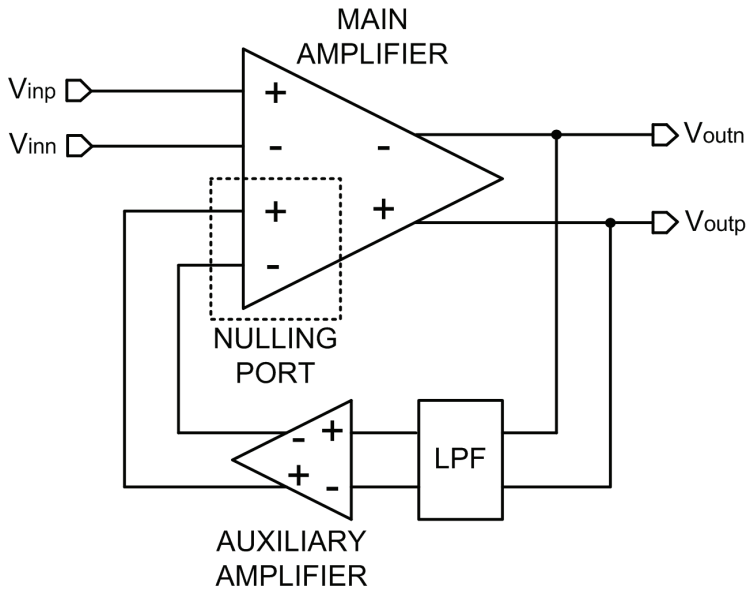

Figure 4.1: Block diagram of the 1st gain stage showing the concept of the offset compensation method used.

Figure 4.2 shows the schematic diagram of the 1st gain stage, and Table 4.1 gives the device parameters and the bias currents used. The main amplifier is implemented with a differential pair consisting of NMOS input transistors M_{n3} and M_{n4}, which are biased with a current source M_{n0}. An additional differential pair M_{n5} and M_{n6} biased with a current source M_{n1} is connected in parallel with the main input pair to form the nulling port [93, 94]. The auxiliary amplifier is also realized using a differential pair with M_{n7} and M_{n8} as the NMOS input transistors and M_{n2} as the current source. All of the differential pairs use resistive loads. The resistances of the loads and the bias currents are selected to set the gain of the differential pairs while obtaining approximately 0 V CM voltages at the outputs of the differential pairs. Utilizing resistive loads instead of MOS loads avoids the need to use a common-mode feedback (CMFB) circuitry that would increase the power and area consumption. Also, since resistors do not suffer from 1/f noise [2], resistive loads offer improved noise performance compared to MOS loads.

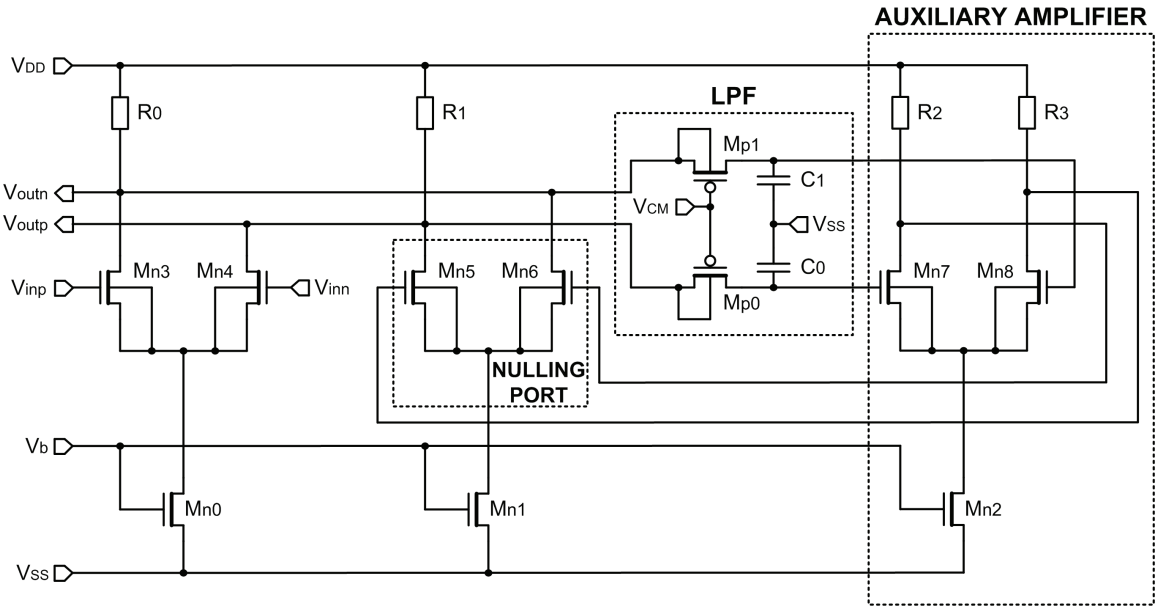

Figure 4.2: Schematic diagram of the 1st gain stage.

When the inputs V_{inp} and V_{inn} are at the same CM potential, the offset voltage of the main amplifier produces a difference ΔI in the drain currents of M_{n3} and M_{n4}. An error signal is generated by the auxiliary amplifier in response to this current difference. Applying this error signal to the nulling port produces a difference $-\Delta I$ in the drain currents of M_{n5} and M_{n6}, which is summed with the drain currents of M_{n3} and M_{n4} to make them equal. This way, the offset current and thus the offset voltage is cancelled.

Table 4.1: Device parameters and bias currents in the 1st gain stage.

Device	**Parameter**	
	W / L (µm)	**Bias Current (µA)**
M_{n0}	60 / 2	120
M_{n1}	20 / 2	40
M_{n2}	40 / 2	80
M_{n3}, M_{n4}	72 / 3	60
M_{n5}, M_{n6}	24 / 3	20
M_{n7}, M_{n8}	48 / 3	40
M_{p0}, M_{p1}	4 / 20	
	Resistance (kΩ)	
R_0, R_1	20	80
R_2, R_3	40	40
	Capacitance (pF)	
C_0, C_1	10	

The LPF is implemented with a first-order RC filter. The 3-dB cut-off frequency of the LPF has to be very low to avoid any disturbance that can be caused by the offset compensation circuitry on the high-frequency sensor signal. When the area consumption is considered, this very low cut-off frequency is impractical to realize with passive

resistors and capacitors in CMOS technology. Therefore, PMOS transistors M_{p0} and M_{p1} acting as pseudoresistors [95] are used to realize a very high-resistance resistor that makes the 3-dB cut-off frequency of the LPF approximately 16 mHz.

At low-frequencies, the gain is reduced by the offset compensation circuitry and expressed at DC as

$$A_v = \frac{A_{v,m}}{A_{v,LPF} A_{v,nl} A_{v,aux}} = \frac{g_{m,m} R_0}{(g_{m,nl} R_0)(g_{m,aux} R_2)} = \frac{g_{m,m}}{g_{m,nl} g_{m,aux} R_2}, \quad (4.1)$$

where $A_{v,m}$, $A_{v,nl}$, $A_{v,aux}$, $A_{v,LPF}$ are the gains of the main, nulling, and auxiliary amplifiers, and the LPF, respectively, and $g_{m,m}$, $g_{m,nl}$, $g_{m,aux}$ are the transconductances of the input transistors of the main, nulling, and auxiliary amplifiers, respectively. With $g_{m,m}$ = 550 µS, $g_{m,nl}$ = 182 µS, $g_{m,aux}$ = 365 µS, and R_2 = 40 kΩ, the DC gain is calculated as A_v = -13.7 dB. As the gain of the LPF decreases with increasing frequency, the effect of the offset compensation circuitry on the gain of the main amplifier is reduced. Therefore, in the sensor operation BW (100 kHz – 1 MHz), the gain is determined by the main amplifier and is expressed as

$$A_v = -g_{m,m} R_0, \quad (4.2)$$

where $g_{m,m}$ is the transconductance of the input transistors of the main amplifier. With $g_{m,m}$ = 550 µS and R_0 = 20 kΩ, the gain is calculated as A_v = 20.8 dB.

Figure 4.3 shows the measured amplitude and phase transfer characteristics of the 1st gain stage obtained using a network analyzer. Since the network analyzer did not allow low noise data points at low frequencies, the low-frequency portion ranging from 1 mHz to 1 kHz of this figure is formed using the extracted data points from the simulations. The measured gain of 19.6 dB in the sensor operation BW (100 kHz - 1 MHz) and simulated gain of -13.5 dB at DC are in good agreement with the calculated values.

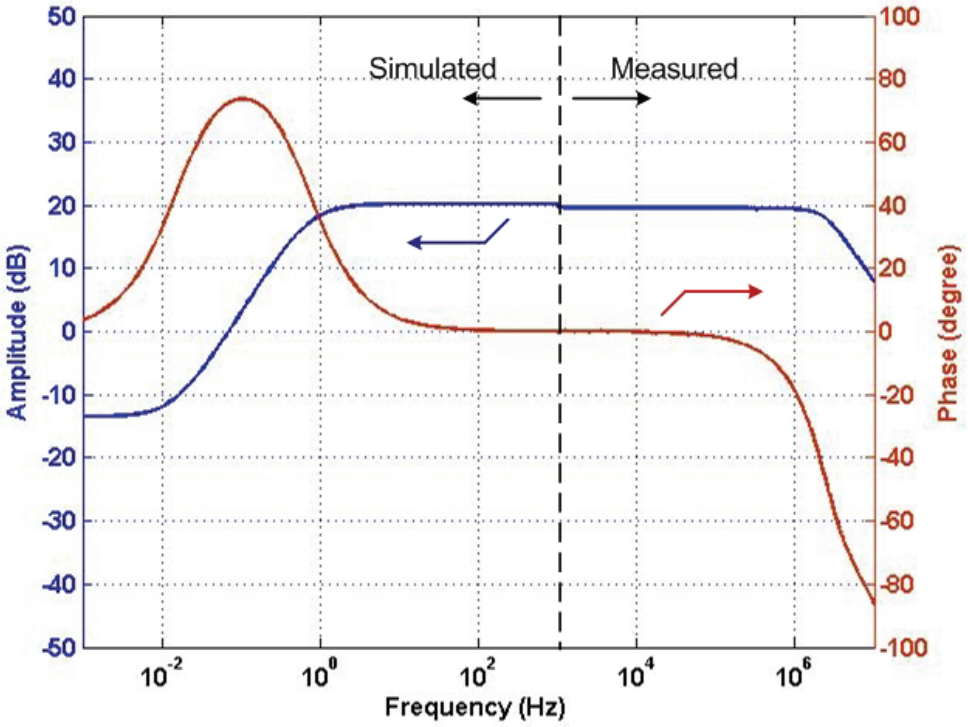

Figure 4.3: Amplitude and phase transfer characteristics of the 1st gain stage. The low frequency portion (10^{-3} – 10^{3} Hz) is from simulation; the high frequency portion (10^{3} - 10^{7} Hz) is measured.

Figure 4.4 presents simulation results showing the output noise of the 1st gain stage with (blue line) and without (red line) the offset compensation circuitry. The low-frequency noise shaping because of the offset compensation circuitry is clearly observed in this figure. The decrease in the offset and very low-frequency noise with the offset compensation method comes at the expense of an increased thermal noise at high frequencies, increasing from 80 nV/√Hz to approximately 400 nV/√Hz. Despite this thermal noise increase, the oscillation can be easily sustained, since the differential signal amplitude at the Wheatstone bridge output of the microresonator is typically high enough. However, increased thermal noise deteriorates the short-term frequency stability.

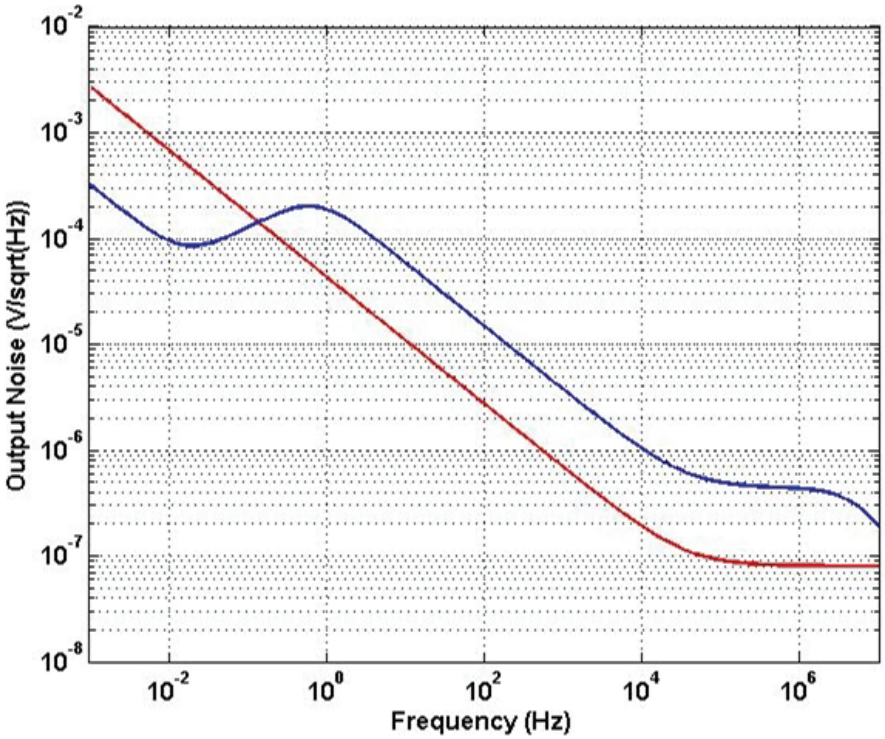

Figure 4.4: Simulated output noise of the 1st gain stage with (blue line) and without (red line) the offset compensation circuitry.

4.1.2 Second Gain Stage

The 2nd gain stage uses a VGA to obtain the gain tuning needed for oscillation amplitude regulation. Figure 4.5 shows the schematic diagram of this VGA, and Table 4.2 gives the device parameters and the bias currents used. The VGA is implemented with a differential amplifier with a source degeneration resistor [96]. The differential amplifier is formed with NMOS input transistors M_{n2} and M_{n3} and resistive loads R_0 and R_1, and is biased with NMOS transistors M_{n0} and M_{n1}. Similar to the 1st gain stage, the CM output voltage is set by the load resistors instead of a CMFB circuitry.

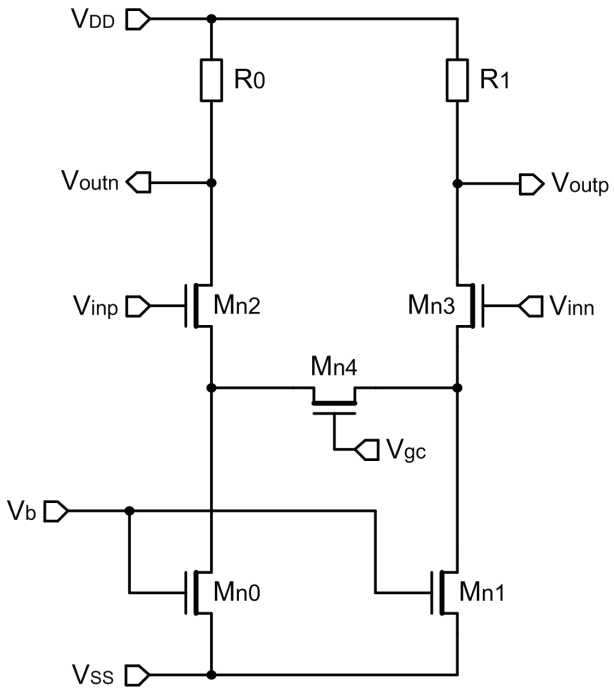

Figure 4.5: Schematic diagram of the VGA of the 2nd gain stage.

Table 4.2: Device parameters and bias currents for the VGA of the 2nd gain stage.

Device	**Parameter**	
	W / L (μm)	**Bias Current (μA)**
M_{n0}, M_{n1}	80 / 2	160
M_{n2}, M_{n3}	384 / 3	160
M_{n4}	12 / 2	
	Resistance (kΩ)	
R_0, R_1	10	160

The source degeneration resistor is implemented with an NMOS transistor M_{n4} operating in its linear region. In this case, the gain expression of the VGA is given by

$$A_v = -\frac{g_{m,in}R_0}{1 + g_{m,in}R_{n4}/2}, \tag{4.3}$$

where $g_{m,in}$ is the transconductance of the input transistors, and R_{n4} is the resistance of the source degeneration resistor expressed as [87]

$$R_{n4} = \frac{1}{\mu_n C_{ox} \frac{W}{L}(V_{gs,n4} - V_{th,n4})} = \frac{1}{\mu_n C_{ox} \frac{W}{L}(V_{gc} - V_{s,n4} - V_{th,n4})}, \tag{4.4}$$

where μ_n is the surface mobility, C_{ox} is the capacitance per unit area of the gate oxide, W is the effective channel width, L is the effective channel length, and $V_{th,n4}$ is the threshold voltage of M_{n4}. Equation (4.4) shows that changing the gate voltage of M_{n4} (V_{gc}) results in a change in the resistance R_{n4}. As can be observed from Eq. (4.3), this resistance change alters the gain. Therefore, the AGC circuit controls V_{gc} to regulate the oscillation amplitude.

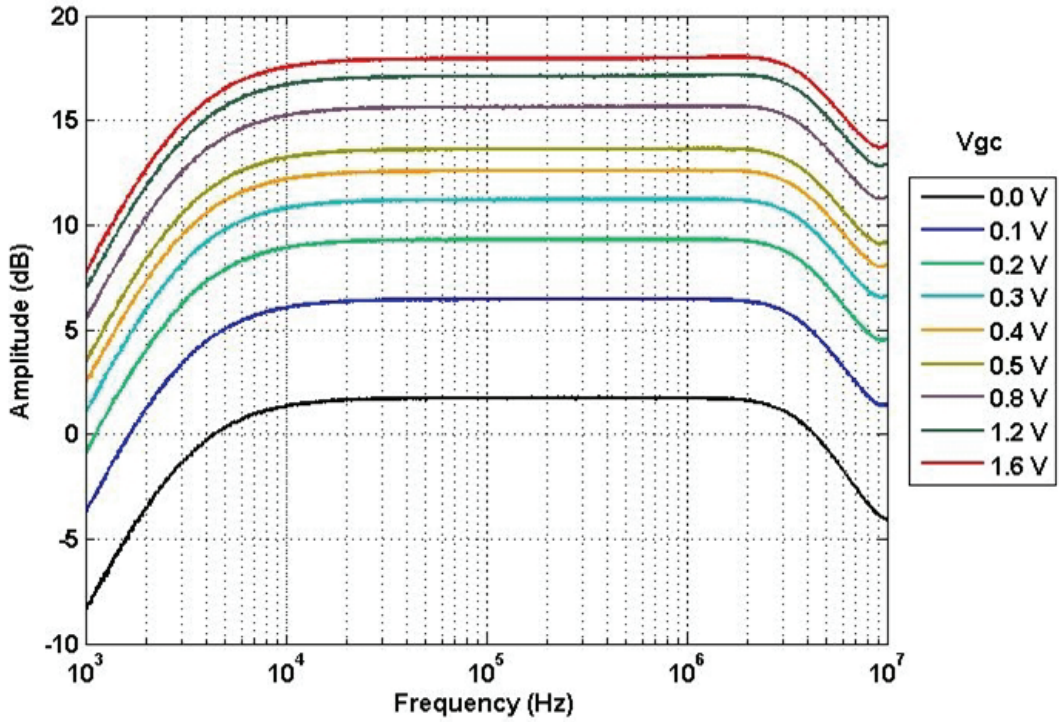

Figure 4.6: Measured amplitude transfer characteristics of the 2nd gain stage for different V_{gc} values.

Figure 4.6 presents the measured amplitude transfer characteristics of the 2nd gain stage for different V_{gc} values with a HPF connected at its output. By changing V_{gc} between 0 V and 1.6 V, the gain can be varied between 2 dB and 18 dB, respectively, in the sensor operation BW.

4.1.3 Third Gain Stage

The 1st gain stage amplifier is reused to realize the 3rd gain stage, which can be enabled or disabled by means of transmission gates (see Figure 3.7) to obtain an additional 20 dB of gain tuning range.

4.1.4 Fourth Gain Stage

Figure 4.7 shows the schematic diagram of the 4th gain stage that uses a closed-loop non-inverting amplifier topology to convert the fully-differential readout signal into a single-ended one. A differential difference amplifier (DDA) [97, 98] with two differential inputs and a single-ended output is employed as the op-amp. The fully-differential input signal is connected to the positive terminals of the differential inputs of the DDA. The closed-loop gain is set by the ratio of the two feedback resistors R_0 and R_1 connected to one of the negative terminals of the differential inputs of the DDA and is given by

$$A_v = 1 + \frac{R_1}{R_0}. \tag{4.5}$$

Figure 4.8 presents the measured amplitude and phase transfer characteristics of the 4th gain stage. In the sensor operation BW, the gain is approximately 20 dB with the chosen resistance values of R_0 = 5 kΩ and R_1= 45 kΩ.

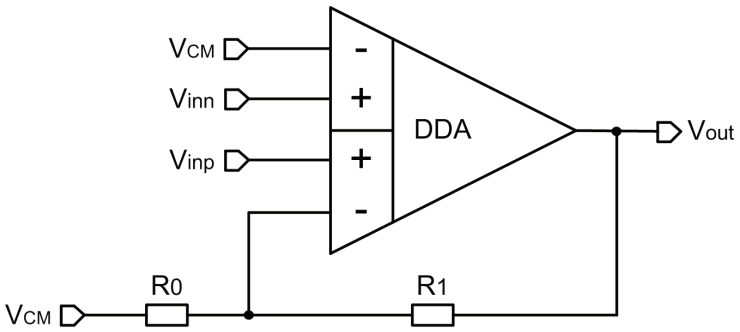

Figure 4.7: Schematic diagram of the 4th gain stage.

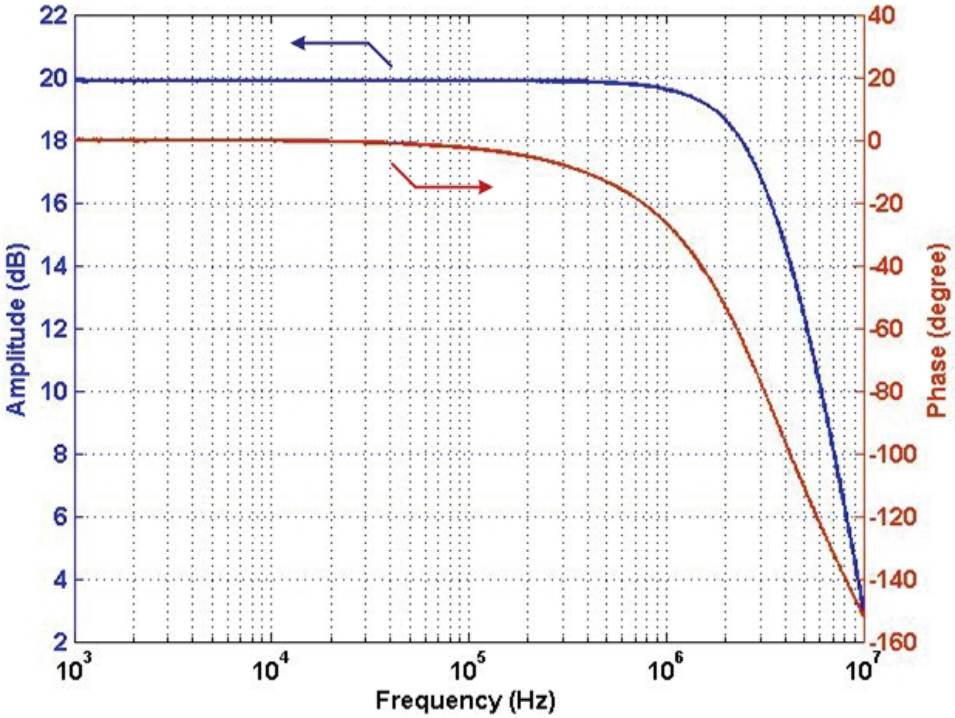

Figure 4.8: Measured amplitude and phase transfer characteristics of the 4th gain stage.

Figure 4.9 shows the schematic diagram of the DDA, and Table 4.3 summarizes the device parameters and the bias currents used. The DDA has a two-stage amplifier topology. The input stage is implemented with two input differential pairs consisting of PMOS transistors $M_{p0\text{-}3}$ and their NMOS active loads M_{n0} and M_{n1}. These differential

pairs are biased with PMOS transistors M_{p4} and M_{p5}. The output of the input stage is connected to the output stage that is included to be able to drive the feedback resistors. The output stage is realized with a common-source amplifier comprised of M_{n2} and its active load M_{p6}. The overdrive voltages of the output stage transistors M_{n2} and M_{p6} are designed to be approximately 0.2 V so that the output voltage can reach a level that is one overdrive voltage less than the supply voltages (approximately ±1.63 V). A compensation capacitor C_C and resistor R_C ensure the stability of the DDA.

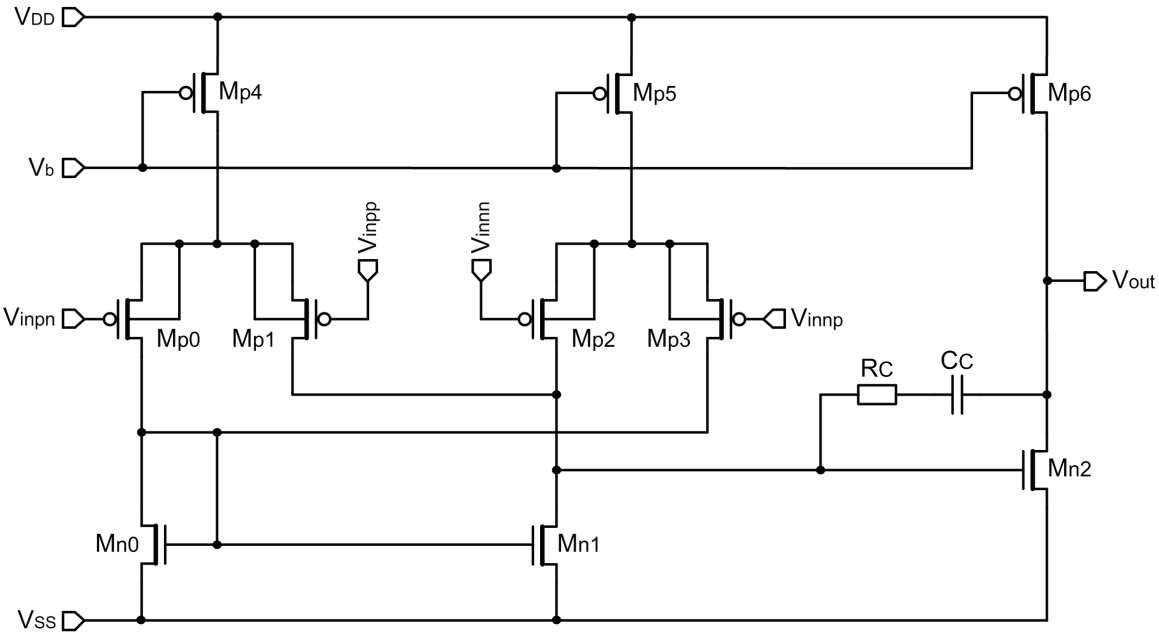

Figure 4.9: Schematic diagram of the differential difference amplifier (DDA) used for the 4th gain stage.

The performance parameters, namely the open-loop gain, PM, GBW, and current dissipation of the DDA are obtained through simulations as 86 dB, 47°, 22.6 MHz, and 0.37 mA, respectively, with a 5 pF load connected to its output.

Table 4.3: Device parameters and bias currents for the DDA of the 4th gain stage.

Device	**Parameter**	
	W / L (µm)	**Bias Current (µA)**
M_{n0}, M_{n1}	80 / 2	80
M_{n2}	90 / 2	180
M_{p0}, M_{p1}, M_{p2}, M_{p3}	140 / 2	40
M_{p4}, M_{p5}	160 / 2	80
M_{p6}	360 / 2	180
	Resistance (kΩ)	
R_C	1	
	Capacitance (pF)	
C_C	2	

In summary, the gain stages provide an overall amplification between 41.6 dB and 79.2 dB across the sensor operation BW with a current dissipation of approximately 1.3 mA. Also, it is important to note that the gain stages add a frequency-dependent phase shift and therefore vary the total loop phase. The effect of this phase shift on the self-oscillation is reduced by the phase shifter and the high Q-factor of the microresonators.

4.2 Filters

First-order RC filters are used to implement the LPFs after the 1st and 3rd gain stages to reduce high-frequency signal coupling and the HPFs after the 2nd and 4th gain stages to remove the DC-offset and flicker noise of these gain stages. The 3-dB cut-off frequencies of the HPF and the LPF are measured approximately as 3.1 kHz and 14.2 MHz, respectively. Thus, the filters do not affect the amplitude and phase transfer characteristics of the feedback loop in the desired operation BW (100 kHz – 1 MHz).

4.3 Amplitude Control

To limit the oscillation amplitude for stability, ASIC_v1 uses a comparator with hysteresis that converts the sinusoidal oscillation signal into an amplitude-limited square-wave [85]. The resulting square-wave signal is used to generate out-of phase AC excitation signals. In this case, the excitation level is adjusted by changing the amplitude of the square-wave. The resulting square-wave excitation signal is composed of harmonics at odd multiples of the resonance frequency and has sharp transition edges. Because of its high Q-factor, the resonator is usually able to filter out these higher-order harmonics. However, since the excitation lines are implemented in close proximity to the readout lines on the microresonator because of area limitations, the transitions of the square-wave signal generally cause coupling artifacts on the readout signal of the resonator. When the Q-factor and signal amplitude of the resonator are low, for instance when the resonator is used for chemical detection in liquid environment, higher-order harmonics and coupling artifacts become more pronounced and deteriorate the frequency stability. To overcome these problems caused by the square-wave excitation signals, ASIC_v2 utilizes an AGC circuit instead of an amplitude limiter to replace square-wave excitation signals with sinusoidal ones.

AGC circuits have been employed with electrostatically transduced MEMS resonators to keep their oscillation amplitude constant [99-101]. In this work, a similar architecture is used to implement the AGC loop as shown in Figure 4.10. Here, the output signal of the 4th gain stage is connected to a level detector composed of a rectifier and an integrator. The input signal of the AGC is first half-wave rectified by the rectifier. The integrator then low-pass filters this rectified signal to generate a DC voltage proportional to the oscillation amplitude. The simulated rectified and filtered waveforms at points A and B in Figure 4.10, respectively, are shown in Figure 4.11 when a 600 mV_{pp} sinusoidal input signal at 500 kHz is applied. The error amplifier compares the DC voltage at the level detector output with a reference value V_{ref} to generate a control voltage (V_{gc}), which

is connected to the gate of the source degeneration NMOS transistor M_{n4} to adjust the gain of the 2nd gain stage.

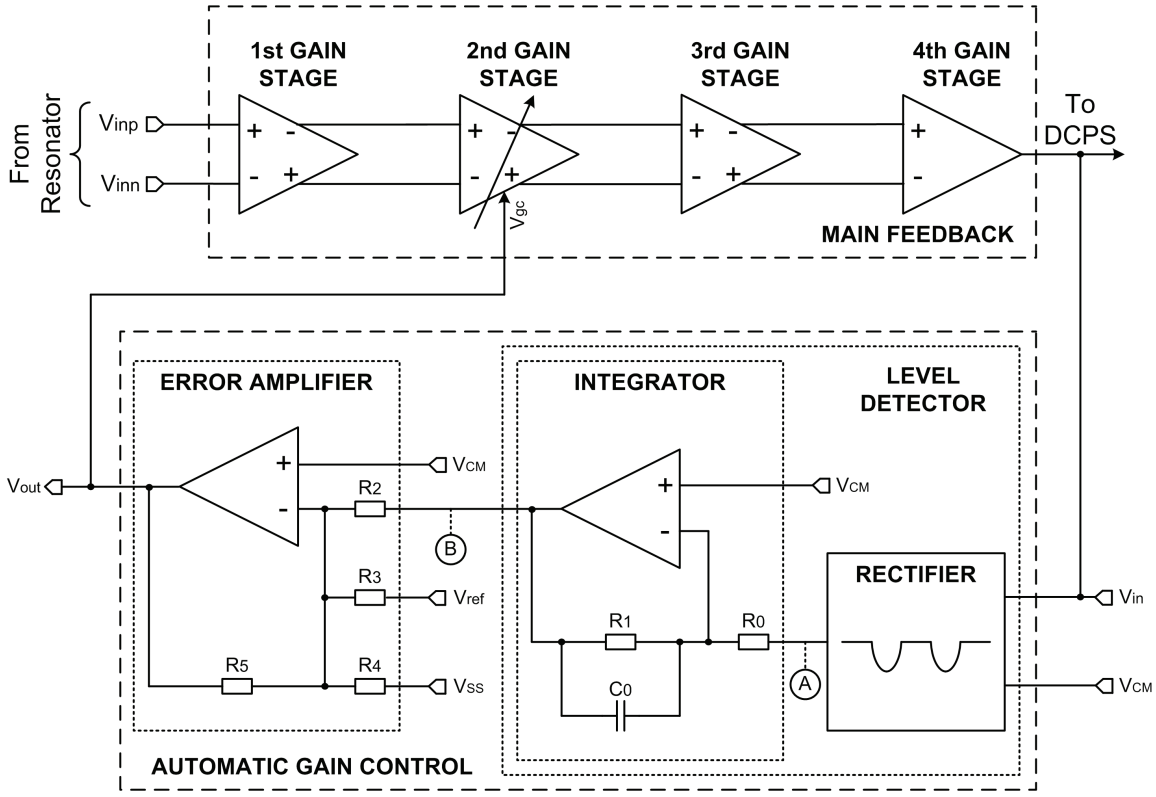

Figure 4.10: Schematic diagram of the AGC circuit.

The output voltage of the AGC circuit, equal to V_{gc}, is given by

$$V_{out} = V_{gc} = -(A_{v,level} V_{in} + V_{ref} + V_{SS}) , \tag{4.6}$$

where $A_{v,level}$ is the gain of the level detector, V_{in} is the input voltage of the AGC circuit, and V_{SS} = -1.65 V is the negative supply voltage. During startup, when there is no oscillation, V_{in} is zero. In this case, the control voltage V_{gc} and therefore the amplification from the 2nd gain stage are at their maximum for a given V_{ref}. As the oscillation amplitude grows, V_{in} increases, and hence, V_{gc} decreases. This way, the gain of the 2nd

gain stage decreases until it reaches an equilibrium at which the oscillation amplitude stays constant at a level set by V_{ref}.

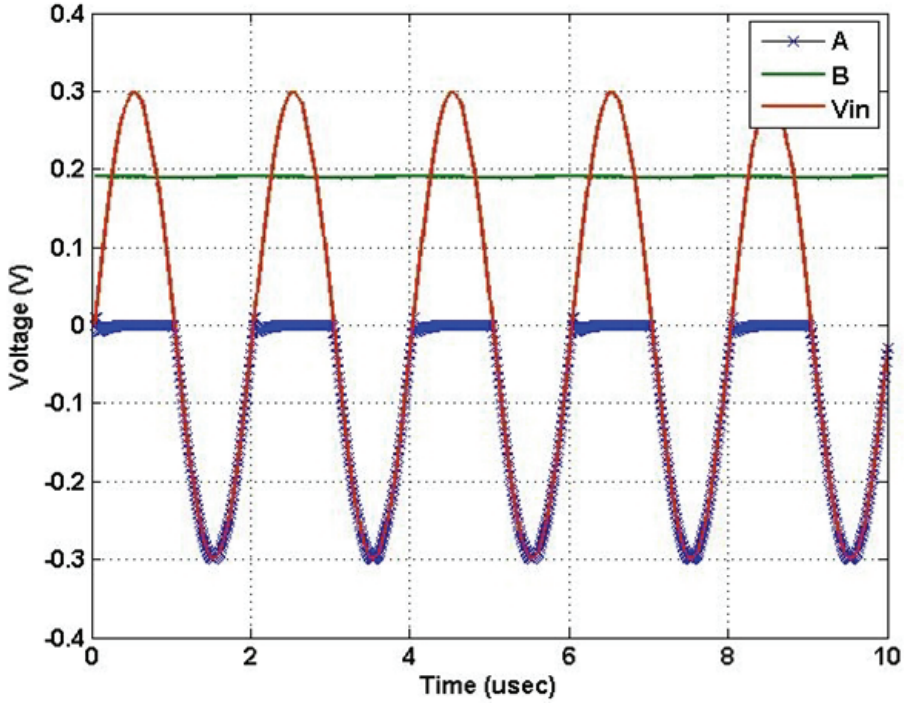

Figure 4.11: Simulated waveforms at points A and B in Figure 4.10 when a 600 mV_{pp} sinusoidal input signal at 500 kHz is applied.

Figure 4.12 shows the schematic diagram of the rectifier, and Table 4.4 gives the device parameters and the bias currents used. A differential pair implemented with NMOS input transistors M_{n1} and M_{n2} and PMOS active loads M_{p0} and M_{p1} is used as a comparator, which compares the input signal with the CM level of 0 V. By sizing M_{n1} and M_{n2} with a mismatch, an intentional offset is generated to make the comparator insensitive to noise. The output of the comparator (drain of M_{p1}) is connected to two inverters that control a transmission gate formed with M_{p2} and M_{n3}. When the input signal is positive, the output of the comparator becomes negative and the transmission

gate is turned off. Therefore, the output of the rectifier is at 0 V. On the other hand, a negative input signal makes the output of the comparator positive and thus turns on the transmission gate. In this case, the input signal is connected to the output of the rectifier through the transmission gate. In this way, half-wave rectification is obtained as shown by the blue line in Figure 4.11.

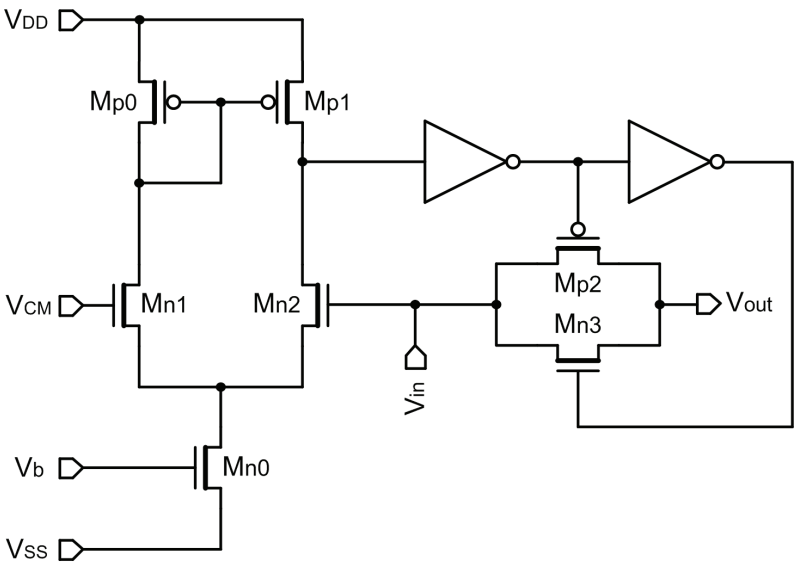

Figure 4.12: Schematic diagram of the rectifier used in the AGC circuit.

Table 4.4: Device parameters and bias currents of the rectifier used in the AGC circuit.

Device	**Parameter**	
	W / L (µm)	**Bias Current (µA)**
M_{n0}	200 / 2	50
M_{n1}	40 / 1	26
M_{n2}	36 / 1	24
M_{p0}	2 / 0.4	26
M_{p1}	2 / 0.4	24
M_{p2}, M_{n3}	1 / 0.4	

The integrator is implemented using a first-order active LPF with a gain of 6 dB and a 3-dB cut-off frequency of 1.7 kHz. Besides, a summing amplifier with a gain of 0 dB is used to implement the error amplifier. A basic Miller-compensated two-stage op-amp is used to realize both the integrator and the error amplifier.

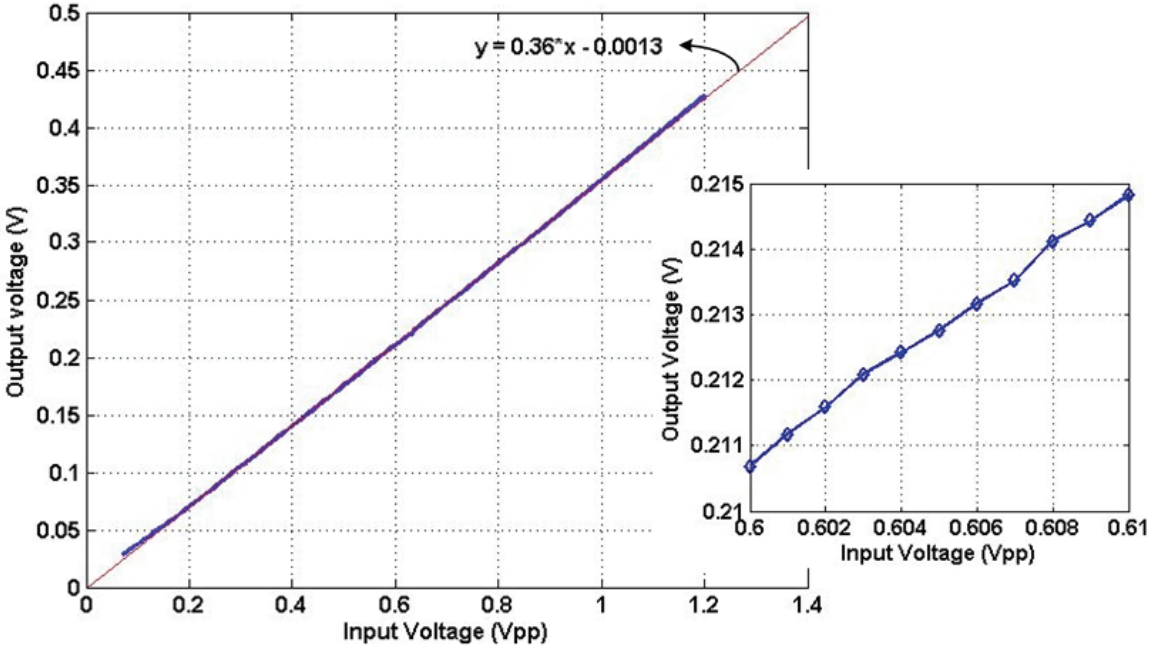

Figure 4.13: Measured input-output transfer characteristic of the level detector and (inset) response of the level detector to 1 mV change in the input amplitude for a 500 kHz input signal with variable amplitude.

Figure 4.13 shows the measured input-output transfer characteristic of the level detector when the amplitude of a 500 kHz sinusoidal input signal is swept from 70 mV_{pp} to 1.2 V_{pp}. From this measurement, the maximum deviation of the level detector output from a linear fit is extracted, and accordingly the nonlinearity of the level detector is estimated as 1.4 %. Additionally, the inset of Figure 4.13 verifies that the level detector can sense changes as small as 1 mV in the input amplitude. The output of the level

detector (blue line) in response to a 500 kHz sinusoidal input signal, amplitude-modulated with a triangular wave (red signal), is given in Figure 4.14. To find the level detector gain as a function of frequency, the input signal frequency is swept from 100 kHz to 1 MHz. As a result, the gain of the level detector is found to increase approximately 0.025 % with every 1 kHz change in the input signal frequency, which is acceptable for AGC loop operation.

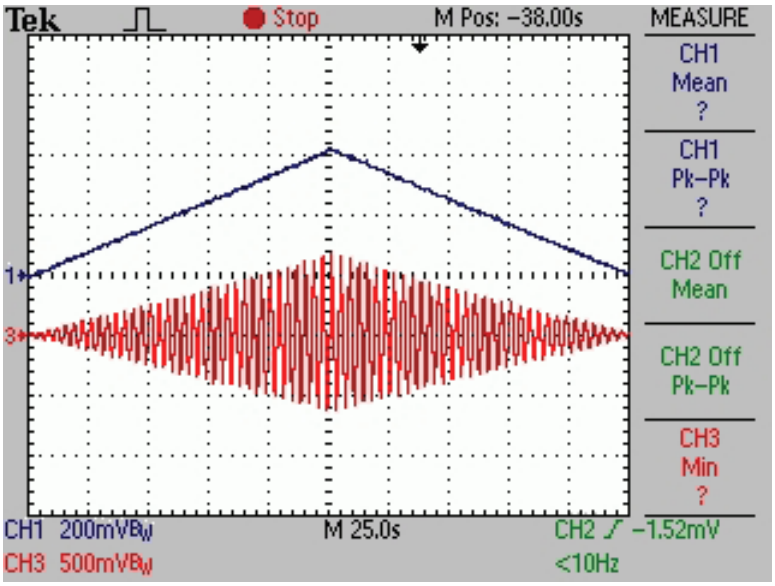

Figure 4.14: Output of the level detector (blue line) in response to a 500 kHz sinusoidal input signal, amplitude modulated with a triangular wave (red signal).

4.4 Phase Adjustment

Both ASIC_v1 and ASIC_v2 use a first-order all-pass filter as a phase shifter [102] to introduce a frequency-dependent delay while keeping the amplitude of the input signal constant. Figure 4.15 shows the schematic diagram of the digitally-controlled phase shifter (DCPS) implemented in ASIC_v2.

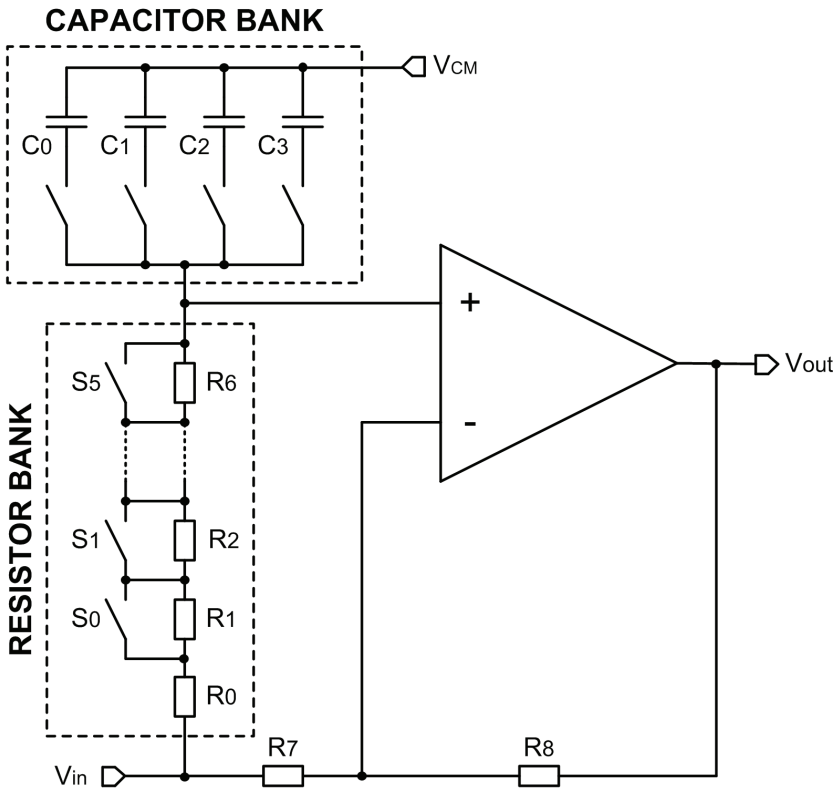

Figure 4.15: Schematic diagram of the digitally-controlled phase shifter (DCPS) implemented in ASIC_v2.

The transfer function of the DCPS with equal feedback resistors of $R_7 = R_8 = 11$ kΩ is given by

$$T(j\omega) = -\frac{1 - j\omega R_{eq} C_{eq}}{1 + j\omega R_{eq} C_{eq}}, \quad |T(j\omega)| = 1, \tag{4.7}$$

$$\theta(j\omega) = -2\arctan(\omega R_{eq} C_{eq}), \tag{4.8}$$

where R_{eq} is the equivalent resistance of the resistor bank, and C_{eq} is the equivalent capacitance of the capacitor bank. By changing R_{eq} and C_{eq}, the phase of the input signal can be varied as shown by Eq. (4.8).

The capacitor bank, which is manually controlled with switches, is implemented using off-chip components, since very large capacitors are impractical to realize on-chip. The resistor bank includes 7 resistors. The transmission gates $S_{0\text{-}5}$, which are controlled

by a 6-bit digital control code, enable/disable 6 of these resistors. This way, 64 different resistance values between 2.25 kΩ and 20.23 kΩ with steps of 281 Ω can be selected in the resistor bank, resulting in a step size as low as approximately 0.1º at a given frequency. (As a note, ASIC_v1 uses discrete off-chip capacitors and a potentiometer instead of capacitor and resistor banks.)

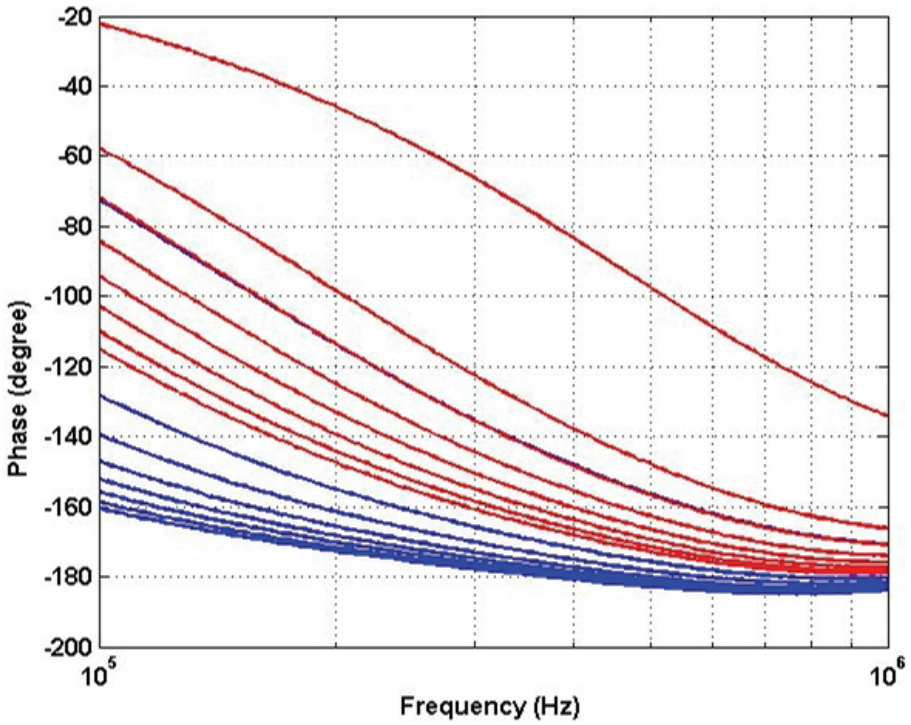

Figure 4.16: Measured phase transfer characteristics of the DCPS for 8 different digital control codes (i.e. resistance as R_{eq}) when C_{eq} is 120 pF (red lines) and 470 pF (blue lines).

Figure 4.16 presents the measured phase transfer characteristics of the DCPS for 8 different digital control codes when C_{eq} is 120 pF (red lines) and 470 pF (blue lines). For a selected capacitor, increasing the digital control code decreases R_{eq}, resulting in a decrease in the phase shift. The phase shift variation that can be obtained by only

changing the digital control code is limited at a given frequency. When the limit is reached, a different capacitor must be selected to extend the range of achievable phase shift.

When the attenuation from the resonator is high, e.g. during operation in liquid, the oscillation signal amplitude has to be large enough to sustain oscillations. In this case, an op-amp that has a large input/output (I/O) voltage range is needed to realize the phase shifter and the buffer, which is included to drive the phase shifter.

A class-AB rail-to-rail I/O op-amp [103] is implemented and used in the phase shifter and the buffer. Figure 4.17 shows the schematic diagram of this class-AB op-amp, and Table 4.5 summarizes the device parameters and the bias currents used. A rail-to-rail CM input range is achieved by using both an NMOS input pair M_{n1} and M_{n2}, which can reach positive supply voltage, and a PMOS input pair M_{p1} and M_{p2}, which can reach negative supply voltage. The input pairs are biased with transistors M_{n0} and M_{p0}. The transistors $M_{p5\text{-}6}$ and $M_{n5\text{-}6}$ are the cascode transistors. The class-AB output stage, which can supply high drive currents to low resistive loads without consuming a high quiescent power, consists of the transistors $M_{p7\text{-}12}$ and $M_{n7\text{-}12}$. The transistors M_{p12} and M_{n12} are the common-source output transistors. Floating class-AB control is formed by M_{p8} and M_{n8}, which are biased by the stacked diode connected transistors $M_{p10\text{-}11}$ and $M_{n10\text{-}11}$, respectively. The quiescent currents in the output transistors are determined by two translinear loops formed with M_{p8}, M_{p10}, M_{p11}, M_{p12} and M_{n8}, M_{n10}, M_{n11}, M_{n12}. A floating current source to bias the current mirror in the cascoded branch is implemented using the transistors M_{p7} and M_{n7}. Finally, a compensation network is implemented with R_C and C_C to ensure the stability of the op-amp.

The performance parameters, namely the open-loop gain, PM, GBW, and current consumption of the class-AB op-amp are obtained through simulations as 132 dB, 67°, 18.9 MHz, and 0.58 mA respectively, when a 5 pF load is connected at its output.

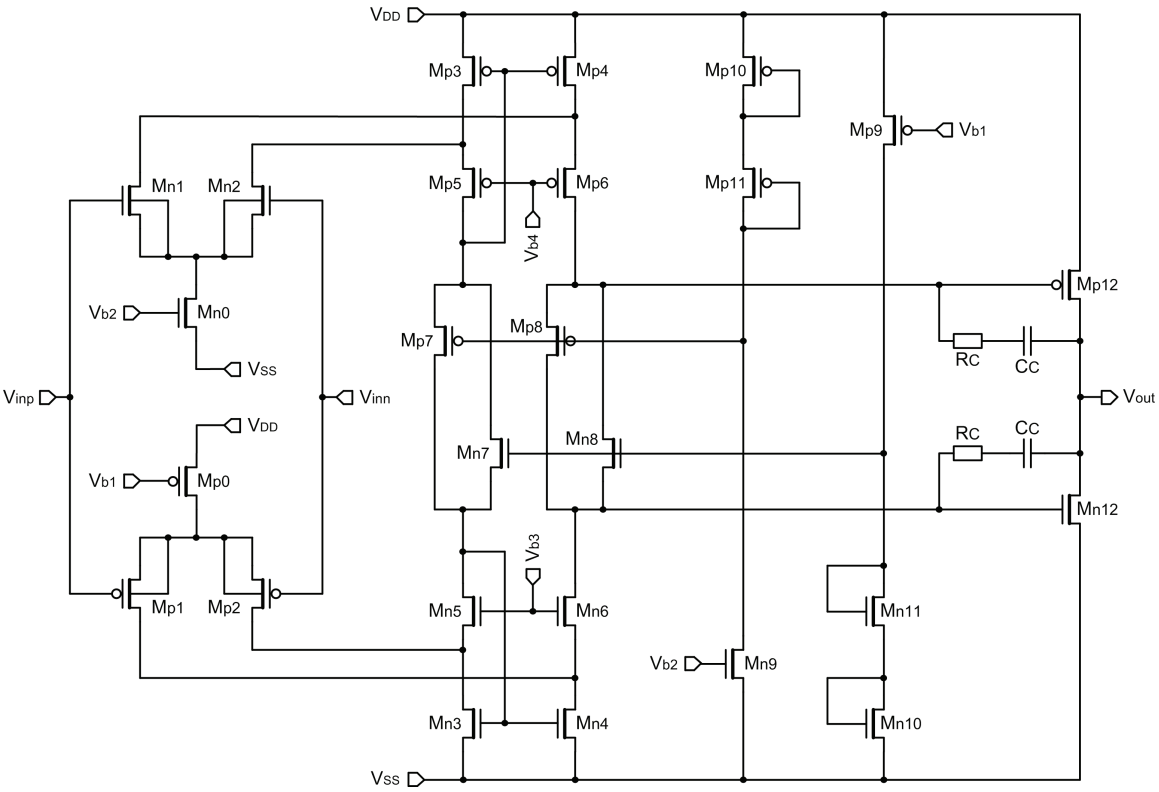

Figure 4.17: Schematic diagram of the class-AB rail-to-rail I/O op-amp used in the DCPS.

To achieve an operating point as close as possible to the resonance frequency, an automatic-phase control (APC) algorithm is implemented in ASIC_v2 with an APC circuit. Figure 4.18 presents the flow chart of this algorithm, which uses an iterative procedure, and Figure 4.19 shows the schematic diagram of the APC circuit. The output of the 1st gain stage is interfaced to an amplifier in the APC circuit. This amplifier is the same as the one used in the 4th gain stage and converts the fully-differential signal at the output of the 1st gain stage into a single-ended one with a gain of 20 dB. Then, the amplitude level of this amplified signal is detected by a level detector, the same as the one used in the AGC circuit. The detected level is interfaced to a PC through a data acquisition (DAQ) card. A Labview program on the PC executes the APC algorithm, in which the PC adjusts the digital control code of the DCPS to shift the phase.

Table 4.5: Device parameters and bias currents of the class-AB rail-to-rail I/O op-amp used in the DCPS.

Device	**Parameter**	
	W / L (µm)	**Bias Current (µA)**
M_{n0}	50 / 2	100
M_{n1}, M_{n2}	128 / 2	50
M_{n3}, M_{n4}	55 / 2	110
M_{n5}, M_{n6}	30 / 1	60
M_{n7}, M_{n8}	30 / 2	30
M_{n9}, M_{n10}	5 / 2	10
M_{n11}	10 / 2	10
M_{n12}	90 / 2	180
M_{p0}	200 / 2	100
M_{p1}, M_{p2}	512 / 2	50
M_{p3}, M_{p4}	220 / 2	110
M_{p5}, M_{p6}	120 / 1	60
M_{p7}, M_{p8}	120 / 2	30
M_{p9}, M_{p10}	20 / 2	10
M_{p11}	40 / 2	10
M_{p12}	360 / 2	180
	Resistance (kΩ)	
R_C	1.5	
	Capacitance (pF)	
C_C	6	

At every code change, the current oscillation amplitude is compared with the previous one associated with the previous code. If the current amplitude is greater than or equal to the previous one, the code is decremented again. This operation is repeated until the oscillation amplitude is maximized. Once the maximum is obtained, the digital control code is held constant.

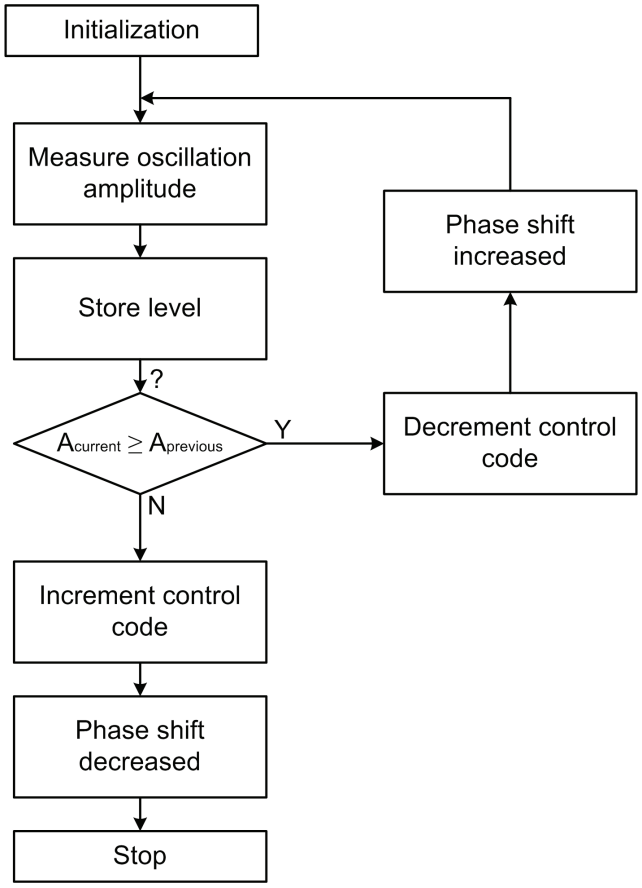

Figure 4.18: Flow chart showing the implemented APC algorithm.

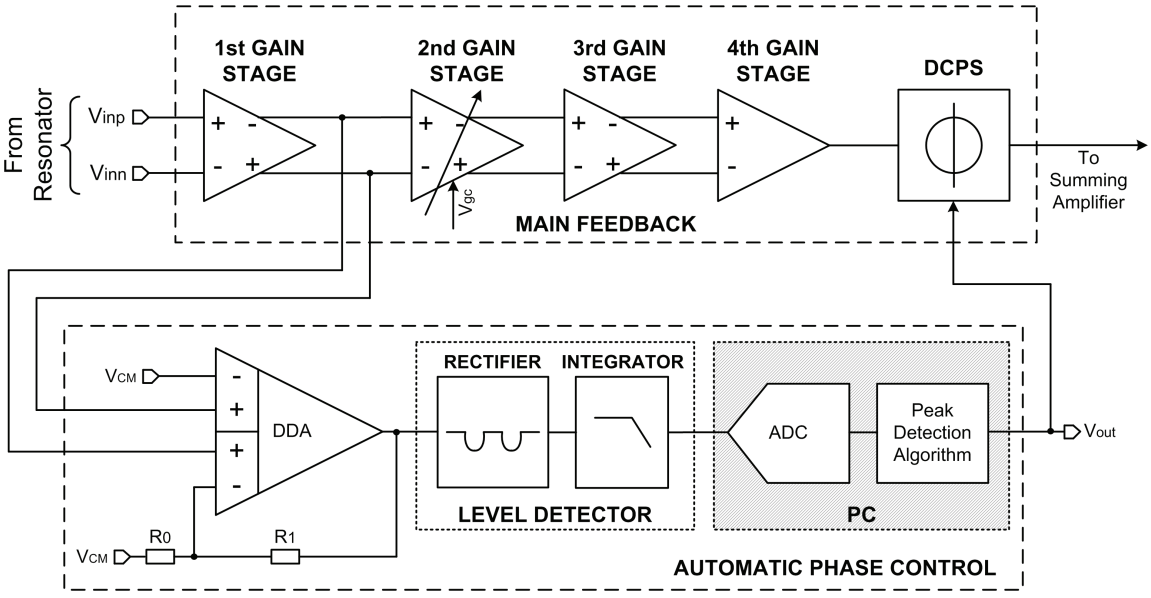

Figure 4.19: Schematic diagram of the APC circuit.

Both the AGC and the APC loop have an influence on the oscillation amplitude. The AGC loop directly adjusts the oscillation amplitude, whereas the APC loop changes the oscillation amplitude through phase variations. Since the oscillation amplitude is a reference measure in both loops, they may interfere with each other and disturb the operation of the MF loop.

To check if there is interference between the control loops, the case when both loops are in operation should be examined. When the APC loop changes the phase of the DCPS, the signal amplitudes at the outputs of the 1st and 2nd gain stages increase. The AGC loop monitors the 2nd gain stage output and tries to counteract this increase by decreasing the amplification of the 2nd gain stage. If the increase in the 1st gain stage output amplitude is small, the AGC loop keeps the 2nd gain stage output amplitude constant. However, in this case, the operation of the AGC loop does not affect the APC loop, since the AGC loop does not control the amplitude of the 1st gain stage output, which is monitored by the APC loop to adjust the phase. The APC loop continues to change the phase, resulting in a further increase of the amplitude of the 1st gain stage output. If this amplitude increase is higher than the possible amplification change obtained by the ACG loop, the AGC loop cannot hold the oscillation amplitude constant. In this case, the oscillation amplitude increases. However, the AGC loop still functions properly and sustains the oscillation at a new equilibrium amplitude level. To sum up, the AGC and APC loops do not affect the operation of each other. (This is experimentally verified in Section 4.6, Figure 4.26.)

4.5 Summing Amplifier

A summing amplifier is implemented after the phase shifter to add signals from the MF loop and the FDC circuit, which is explained in Chapter 6 in detail. Figure 4.20 shows the schematic diagram of the summing amplifier that uses a fully-differential

architecture. Here, the main oscillation signal is connected to V_{in}, and the signals from the FDC circuit are connected to V_{comp1} and V_{comp2}.

The gain expression for the main oscillation signal V_{in} is given by

$$A_v = -\frac{R_2}{2R_0}. \tag{4.9}$$

By selecting R_2 = 20 kΩ and R_0 = 10 kΩ, the summing amplifier generates fully-differential out-of-phase excitation signals (see Figure 3.3 (ii)) with the same amplitudes as that of the single-ended oscillation signal at the output of the phase shifter.

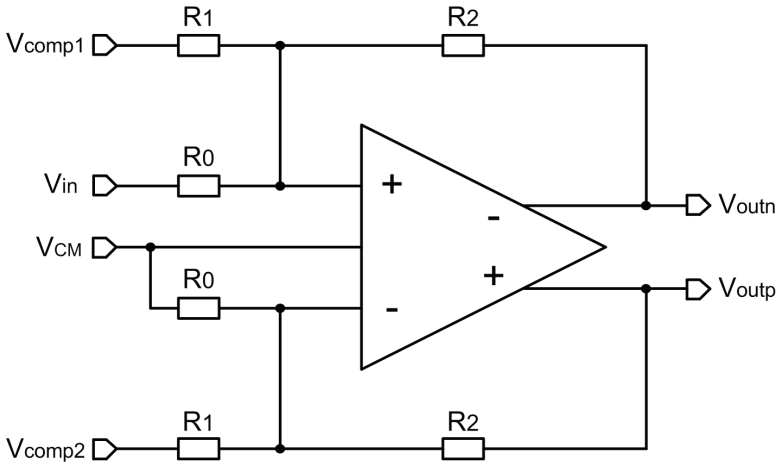

Figure 4.20: Schematic diagram of the summing amplifier.

The summing amplifier uses a fully-differential folded-cascode op-amp. Figure 4.21 shows the schematic diagram of this op-amp, and Table 4.6 gives the device parameters and the bias currents used. Since the input ports of the op-amp are always at the CM voltage of 0 V, there is no need for a rail-to-rail input stage. Therefore, the input stage is formed with a PMOS input pair M_{p1} and M_{p2}, which is biased with a PMOS transistor M_{p0}. The transistors $M_{p5\text{-}6}$ and $M_{n2\text{-}3}$ are the cascode transistors. Two

common-source output stages are implemented with transistors M_{n4} and M_{n5} and their PMOS active loads M_{p7} and M_{p8}, respectively, to drive the feedback resistors while achieving maximum output swing (one overdrive voltage less than the supply voltages). Compensation networks formed with R_C and C_C ensure the stability of the op-amp.

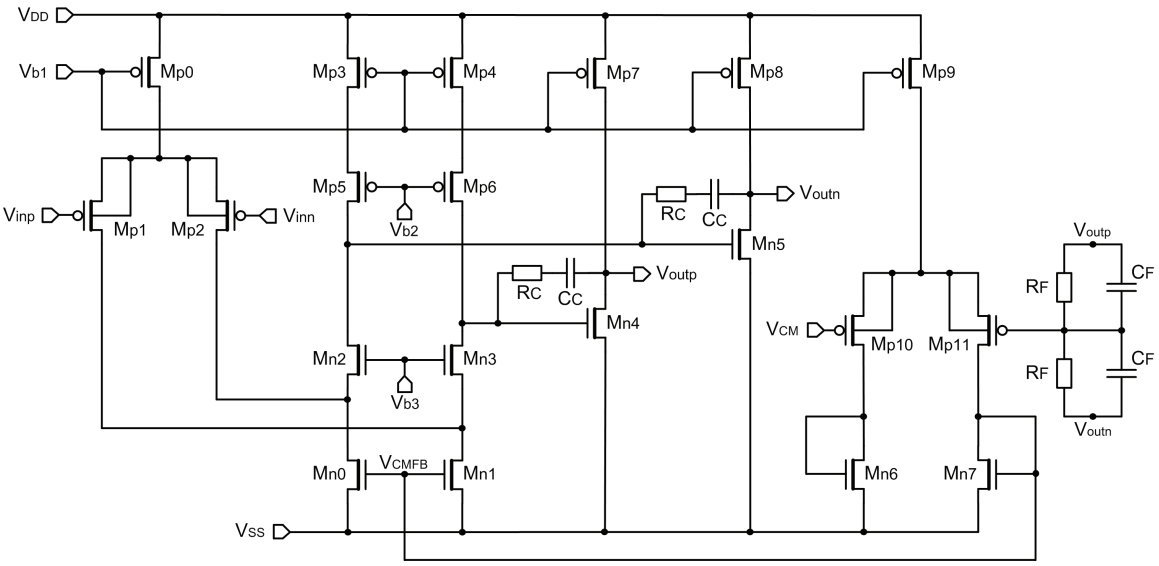

Figure 4.21: Schematic diagram of the fully-differential folded-cascode op-amp used in the summing amplifier.

The fully-differential topology requires a CMFB circuitry to set the output CM voltage level. The CMFB circuitry [104] includes a resistor divider, implemented with resistors R_F, to detect the output CM level and a differential amplifier, implemented with a PMOS differential pair M_{p10} and M_{p11} and NMOS active loads M_{n6} and M_{n7}. The differential amplifier compares the detected output CM level to the voltage V_{CM} and accordingly produces a voltage V_{CMFB} that adjusts the current through M_{n0} and M_{n1} to keep the output CM voltage equal to V_{CM}. The capacitors C_F are used to maintain stability of the CMFB loop.

The performance parameters such as open-loop gain, PM, GBW, and current consumption of this op-amp are obtained through simulations as 119.5 dB, 80°, 12.8 MHz, and 0.75 mA, respectively, with a 5 pF load connected at its output. Besides, with open-loop gain, PM, and GBW of 60 dB, 64°, and 13.7 MHz, respectively, the CMFB circuitry is able to stabilize the output CM level in the GBW of the op-amp.

Table 4.6: Device parameters and bias currents of the fully-differential folded-cascode op-amp used in the summing amplifier.

Device	**Parameter**	
	W / L (µm)	**Bias Current (µA)**
M_{n0}, M_{n1}	60 / 2	120
M_{n2}, M_{n3}	30 / 1	60
M_{n4}, M_{n5}	100 / 2	200
M_{n6}, M_{n7}	10 / 2	20
M_{p0}	240 / 2	120
M_{p1}, M_{p2}	160 / 2	60
M_{p3}, M_{p4}	120 / 2	120
M_{p5}, M_{p6}	120 / 1	60
M_{p7}, M_{p8}	400 / 2	200
M_{p9}	80 / 2	40
M_{p10}, M_{p11}	60 / 1	20
	Resistance (kΩ)	
R_C	1.2	
R_F	3300	
	Capacitance (pF)	
C_C	6	
C_F	0.2	

4.6 Operation of Hybrid-Connected System

A custom-made printed circuit board (PCB), shown in Figure 4.22, was built to operate ASIC_v2 together with a microresonator. ASIC_v2 die is wire bonded in a 44-pin leaded chip carrier (LDCC) package, which is inserted into a socket on the front side of the PCB. A 28-pin dual in-line (DIL) package is used for the sensor chip. The packaged sensor chip is connected to the PCB via a zero insertion force (ZIF)-socket on the backside of the PCB. The placement of the sensor on the backside allows the easy connection of the PCB to the measurement chamber, which is described in Chapter 5.

The PCB includes the necessary off-chip electronics to operate ASIC_v2 and control it by a PC via a DAQ card (PCI NI-6251, National Instruments). A four-output DAC is included to generate the Wheatstone bridge bias voltages, the DC-offset voltages, and the AGC reference voltage (V_{ref}). Two summing amplifiers add the DC-offset voltages to the out-of-phase AC excitation signals from ASIC_v2. The DC shifted excitation signals are applied to one of the four resonators on the sensor chip through manual switches. A Labview program controls the DAQ card to produce control signals for ASIC_v2 and the DAC. Level translators are incorporated to convert the signals from the DAQ card with CMOS logic voltage levels into ±1.65 V to be able to interface with ASIC_v2. (A schematic diagram of the off-chip electronics is given in Appendix A.)

The PCB is powered with ±6 V. The supply voltages ±1.65 V to power ASIC_v2 are generated with regulators. ASIC_v2 consumes a current of 5 mA, resulting in a power consumption of 16.5 mW. Although ASIC_v2 possesses more circuitry with the inclusion of additional control loops compared to ASIC_v1, it consumes 3 times less current than ASIC_v1, which dissipates a current of 15 mA. Moreover, ASIC_v2 features a power down mode. When this mode is enabled, the current and power dissipations decrease to 0.4 mA and 1.32 mW, respectively.

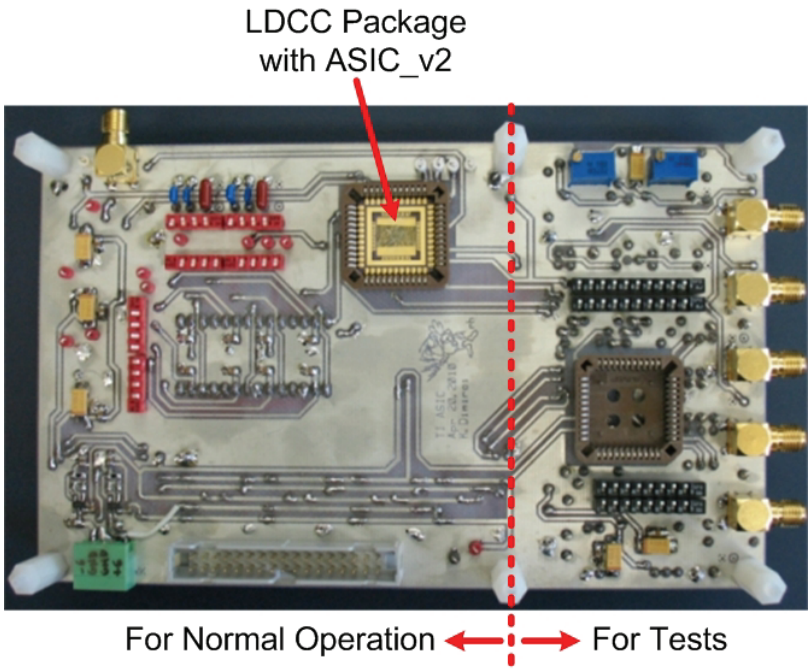

(i)

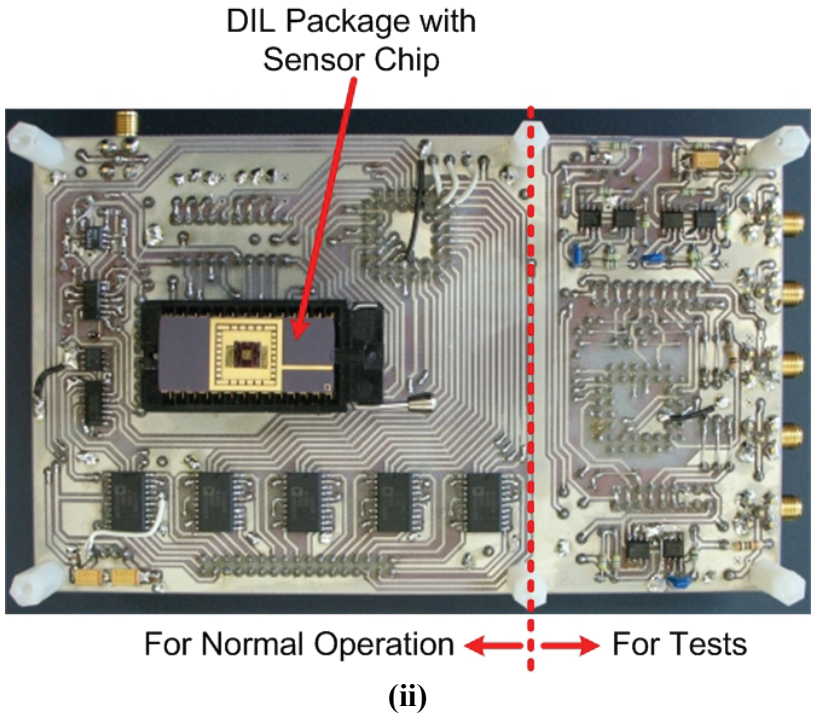

(ii)

Figure 4.22: (i) Front side and (ii) backside views of the custom-made printed circuit board (PCB) including off-chip electronics to control and test ASIC_v2.

With the off-chip electronics on the PCB, the power consumption of the implemented system increases to 117.6 mW. Since commercial ICs with low current consumption are employed to realize the off-chip electronics (4.8 mA in total), this power consumption increase is mostly because of the increase in the power supply voltages from ±1.65 V to ±6 V. There are two reasons for utilizing ±6 V: (i) to be able to generate DC-offset voltages large enough to actuate the resonator in liquid environment, and (ii) to be able to interface the system with the DAQ card. Therefore, if the system is only used for gas-phase chemical sensing and is interfaced with a microcontroller instead of a DAQ card, the power consumption can be further reduced significantly. It should be noted that the current power consumption of ASIC_v2 is of the order of the power consumption of the microresonator (5 – 20 mW) with its thermal excitation and piezoresistive detection resistors.

The closed-loop operation of microresonators in air by ASIC_v2 in their low- and high-frequency ranges is verified by Figure 4.23, which shows the DC-shifted out-of-phase excitation signals when ASIC_v2 is interfaced to resonators with resonance frequencies of 382.5 kHz and 795 kHz. In both cases, the DC-offset voltage is adjusted to ±1.5 V, and the Wheatstone bridge is biased with ±1 V. With these bias voltages, the attenuations from the resonators with resonance frequencies of 382.5 kHz and 795 kHz have been measured with a network analyzer approximately as 55 dB and 60 dB, respectively. Hence, the gain stages have to provide gains of at least 55 dB for the 382.5 kHz operation and at least 60 dB for the 795 kHz operation. The reference voltage of the AGC circuit (V_{ref}) is set to 1.4 V and 1.2 V, yielding the excitation amplitudes around 580 mV_{pp} and 800 mV_{pp} for the operation at 382.5 kHz and 795 kHz, respectively. By decreasing V_{ref}, the excitation amplitude can be increased, or vice versa.

In addition, the start-up of the oscillation is demonstrated in Figure 4.24, which shows one of the excitation signals (blue line) and the level detector output of the APC circuit (red line) when the resonator with a resonance frequency of 382.5 kHz is used. To

start the oscillation, the 3rd gain stage is enabled, which increases the total loop gain 20 dB. The start-up time in this case is below 15 ms.

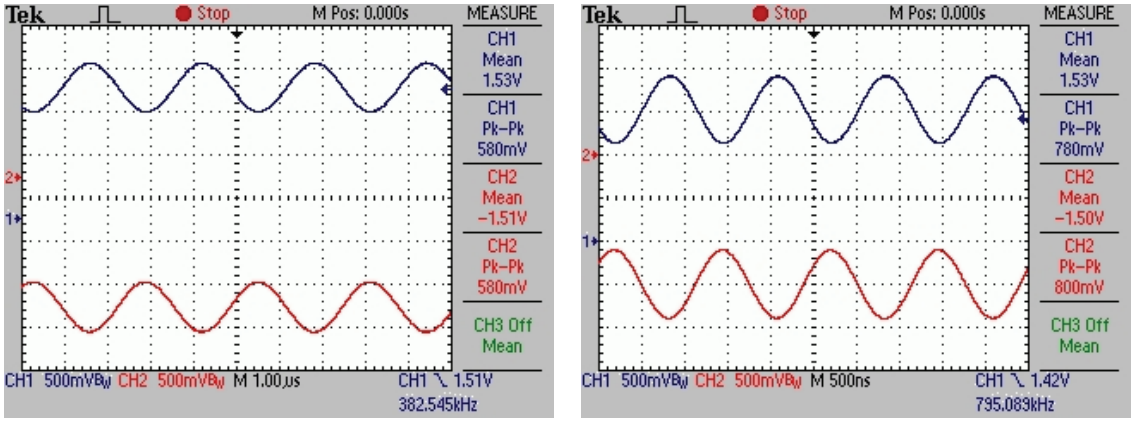

(i) **(ii)**

Figure 4.23: DC-shifted out-of-phase excitation signals when ASIC_v2 is interfaced to resonators with resonance frequencies of (i) 382.5 kHz and (ii) 795 kHz.

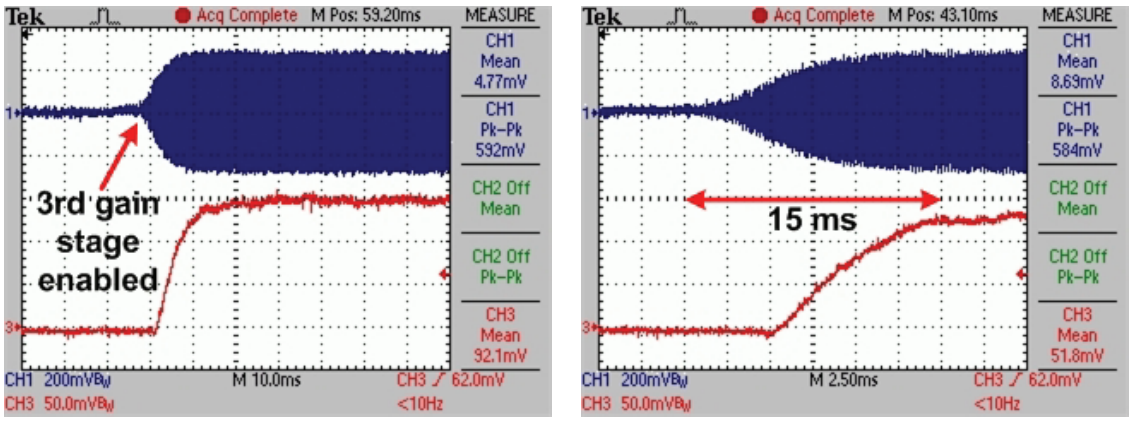

(i) **(ii)**

Figure 4.24: (i) One of the excitation signals (blue line) and the level detector output of the APC circuit (red line) during start-up of the oscillation and (ii) close-up view.

For comparison, the closed-loop operation signals of ASIC_v1 when interfaced to a resonator with a resonance frequency of 283.8 kHz in air are shown in Figure 4.25. As

can be seen from this figure, the square-wave excitation signals result in a distorted readout signal with coupling artifacts at the sharp transients of the square-waves, as described in Section 4.3. With the addition of the AGC loop in ASIC_v2, sine-wave excitation signals are obtained. Therefore, the distortion in the closed-loop oscillation signal is prevented as can be seen in Figure 4.23.

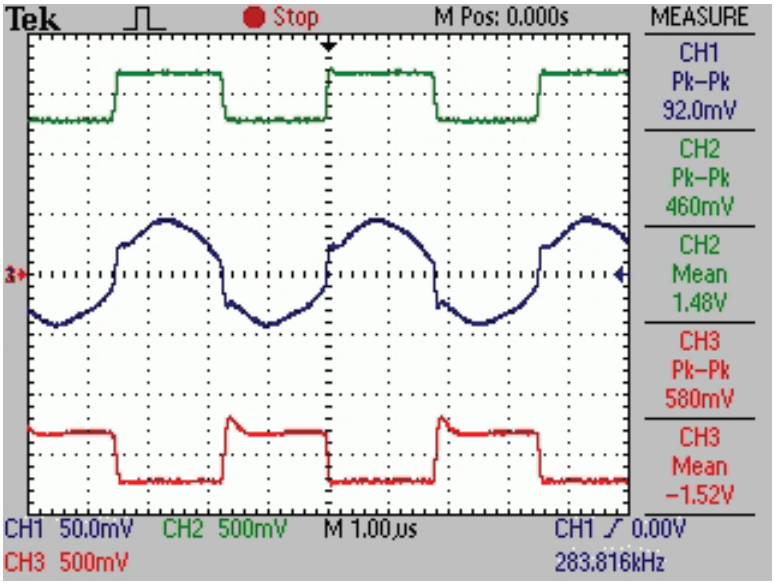

Figure 4.25: DC-shifted out-of-phase square-wave excitation signals (green and red lines) when ASIC_v1 is interfaced to a resonator with resonance frequency of 283.8 kHz in air and the readout signal (blue line) after the 1st gain stage.

The proper operation of the APC loop is verified by Figure 4.26, which shows the increase in the level detector output (red line) and one of the excitation signals (blue line) as the APC loop adjusts the phase by decreasing the digital control code. The APC loop stops and holds the previous digital control code when the maximum oscillation amplitude is obtained.

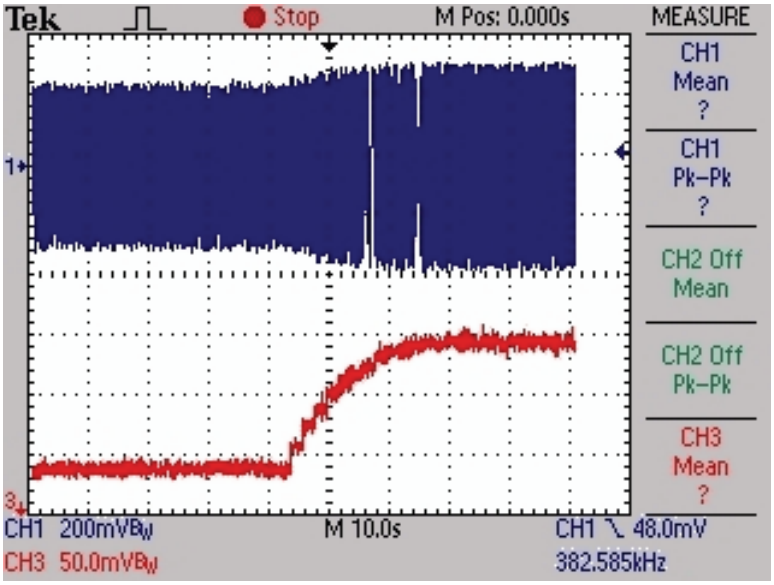

Figure 4.26: The increase in the level detector output (red line) and one of the excitation signals (blue line) as the APC loop adjusts the phase by decrementing the digital control code.

To estimate the obtainable frequency stability for a resonator operating in air, the closed-loop oscillation frequency is recorded using a frequency counter (53131A, Agilent) with a gate time of 1 sec. The recorded data is then used to calculate the Allan variance with the Eq. (2.13) given in Section 2.4.

Figure 4.27 shows the recorded oscillation frequency with a gate time of 1 sec when ASIC_v2 is interfaced to an uncoated disk-type resonator with a resonance frequency of 377.1 kHz and a Q-factor of 2850 in air. From this measurement, the Allan variance is calculated for different gate times and shown in Figure 4.28. To obtain the Allan variance for gate times larger than 1 sec, neighboring data points from the measured data have been averaged.

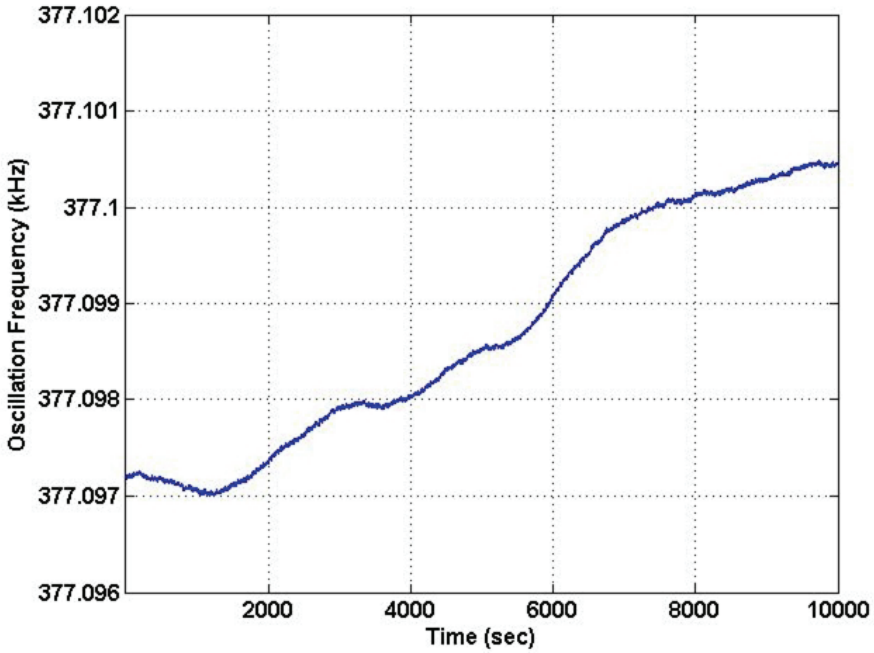

Figure 4.27: The recorded closed-loop oscillation frequency when ASIC_v2 is interfaced to an uncoated disk-type resonator with a resonance frequency of 377.1 kHz and a Q-factor of 2850 in air.

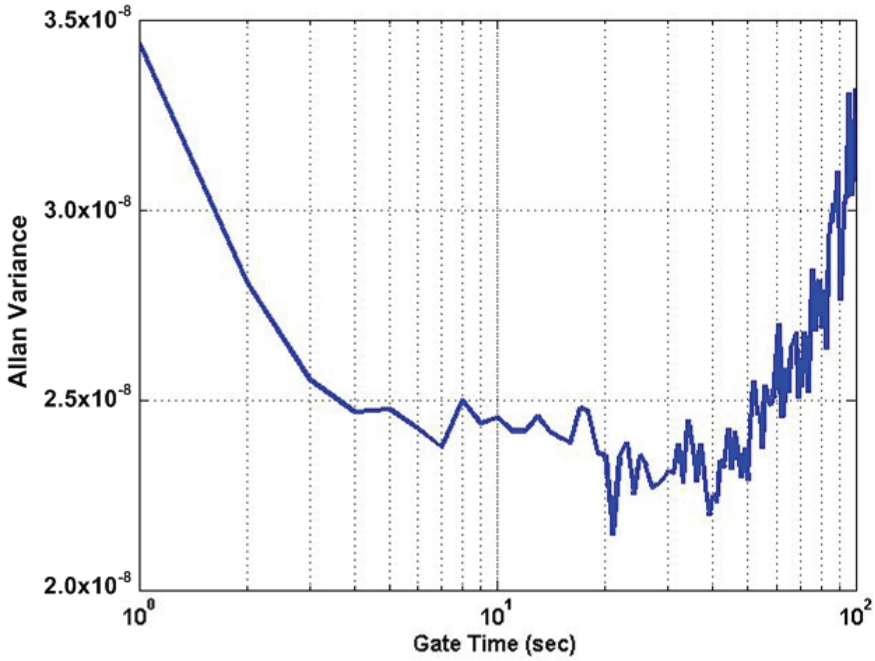

Figure 4.28: Allan variance of an uncoated disk-type resonator with a resonance frequency of 377.1 kHz and a Q-factor of 2850 in air when connected to ASIC_v2 as a function of gate time.

The thermal noise of the microsystem determines the short-term frequency stability. In other words, the Allan variance for small gate times, i.e. the portion of the Allan variance curve in Figure 4.28 up to a gate time of 5 sec, depends on the thermal noise performance. On the other hand, the Allan variance for larger gate times depends on both the flicker noise in the system and the environmental disturbances (e.g. temperature).

The silicon-based cantilever and disk-shape resonators have been used in the gas- and liquid-phase chemical measurements using off-chip electronics implemented on a PCB in previous studies [105, 106]. However, the power consumption and size of the off-chip electronics have been preventing implementation of a portable chemical sensor system. To compare the performance of the CMOS-integrated interface circuits implemented in this work and the off-chip electronics, the same uncoated disk-type resonator with a resonance frequency of 377.1 kHz and a Q-factor of 2850 in air is interfaced to both ASIC_v1 and the off-chip electronics, and the closed-loop oscillation frequency is recorded using a frequency counter (53131A, Agilent) with a gate time of 1 sec as shown in Figure 4.29 and Figure 4.30. It should be noted that the frequency stability is a measure of the system performance. In other words, the noise of both the microresonator and the interface electronics determine the frequency stability. Therefore, a fair performance comparison between the interface electronics is attempted by incorporating the same resonator in the measurements.

From these measurements, the Allan variance is calculated for different gate times and shown in Figure 4.31 for all three interface electronics. To obtain the Allan variance for gate times larger than 1 sec, neighboring data points from the measured data have been averaged.

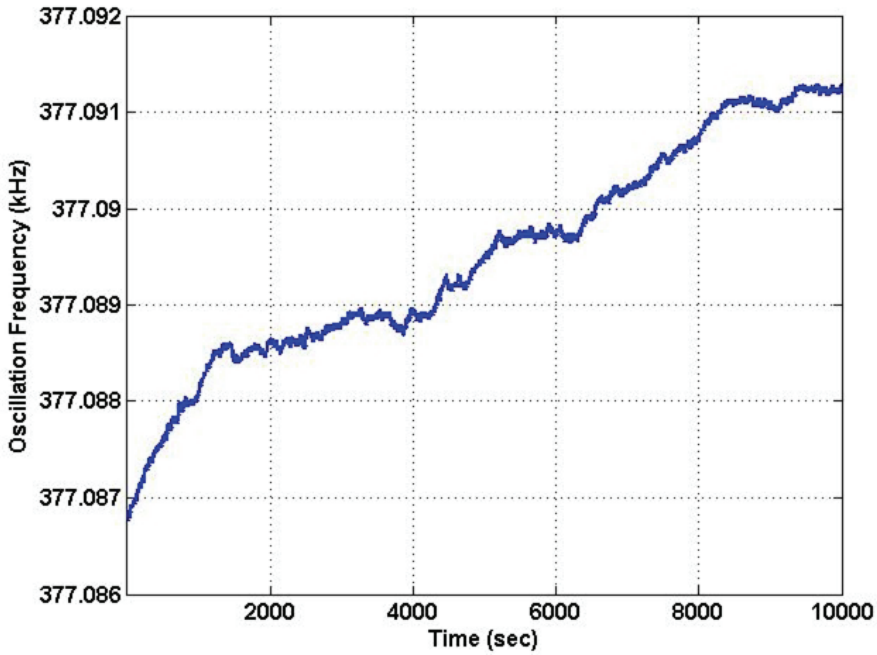

Figure 4.29: The recorded closed-loop oscillation frequency when ASIC_v1 is interfaced to an uncoated disk-type resonator with a resonance frequency of 377.1 kHz and a Q-factor of 2850 in air.

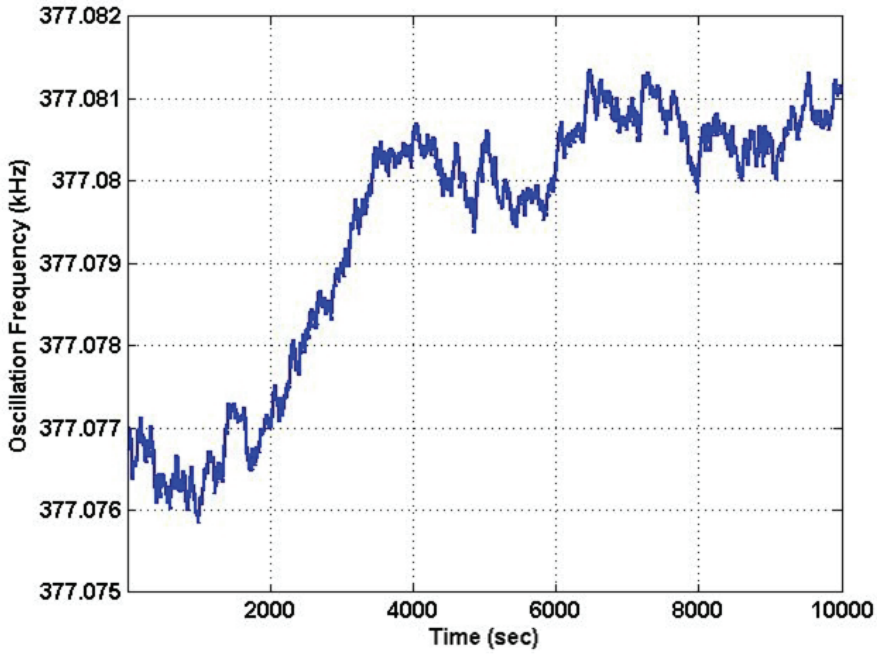

Figure 4.30: The recorded closed-loop oscillation frequency when off-chip electronics are interfaced to an uncoated disk-type resonator with a resonance frequency of 377.1 kHz and a Q-factor of 2850 in air.

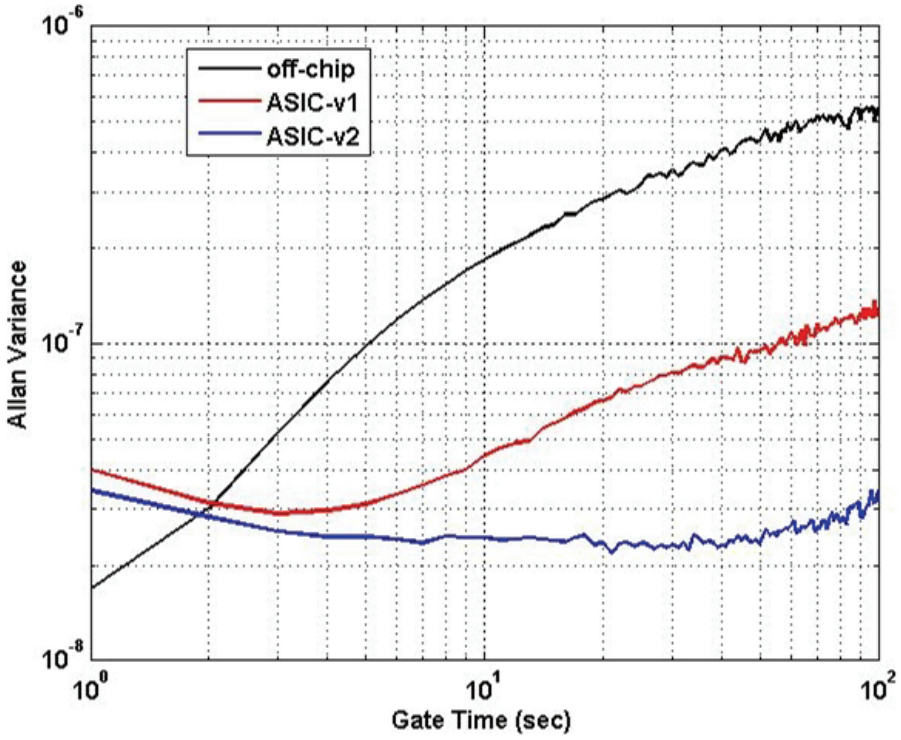

Figure 4.31: Allan variance of an uncoated disk-type resonator with a resonance frequency of 377.1 kHz and a Q-factor of 2850 in air connected to the off-chip electronics, ASIC_v1, and ASIC_v2 as a function of gate time.

As can be observed from Figure 4.31, the off-chip electronics show the best short-term frequency stability (for a gate time of 1 sec), since discrete amplifiers have better noise performance because of their BJT input stages and higher current dissipation. In addition, ASIC_v1 and ASIC_v2 have similar short-term frequency stability performances. For gate times greater than 4 sec, the greater increase in the Allan variance for the off-chip electronics compared to ASIC_v1 and ASIC_v2 is due to the fact that environmental disturbances, e.g. temperature, create a larger effect because of the larger area of the PCB on which the off-chip electronics is implemented. The effect of environmental disturbances is comparable for ASIC_v1 and ASIC_v2, because the die sizes of these two chips are almost the same. In this case, the 1/f noise in the system determines the long-term frequency stability and affects the Allan variance for larger gate

times [107, 108]. Since ASIC_v2 has lower 1/f noise compared to that of ASIC_v1, a reduced Allan variance is obtained for ASIC_v2 for large gate times.

Table 4.7 summarizes the measurement results mentioned above and gives a performance comparison between the CMOS-integrated electronics and off-chip electronics when interfaced with the same resonator.

Table 4.7: Performance comparison between CMOS-integrated electronics and off-chip electronics when interfaced with the same resonator (f = 377.1 kHz, Q = 2850 in air).

		Off-Chip	**ASIC_v1**	**ASIC_v2**
Allan Variance	**Gate Time = 1 sec**	1.67×10^{-8}	4.03×10^{-8}	3.42×10^{-8}
	Gate Time = 10 sec	18.4×10^{-8}	4.29×10^{-8}	2.43×10^{-8}
	Gate Time = 100 sec	55.2×10^{-8}	12.2×10^{-8}	3.45×10^{-8}
Frequency Stability	**Gate Time = 1 sec**	6.3 mHz	15.2 mHz	12.9 mHz
	Gate Time = 10 sec	69.5 mHz	16.2 mHz	9.2 mHz
	Gate Time = 100 sec	208.4 mHz	45.9 mHz	13 mHz
Power Consumption	**Chip Only**	N/A	75 mW (±2.5 V)	16.5 mW (±1.65 V)
	System	2.8 W (±5 V & ±10 V)	95 mW (±2.5 V)	117.6 mW (±6 V)

In summary, when compared to off-chip electronics, the CMOS-integrated interface circuits implemented in this work show comparable noise performance with much less power consumption (more than an order of magnitude) and therefore allow the future integration of the entire system in a compact package resulting in reduced system

cost. In addition, with an Allan variance of 3.4 x 10^{-8} obtained with a gate time of 1 sec, ASIC_v2 shows almost a 3 times better short-term frequency stability than an oscillator microsystem utilizing a cantilever-type microresonator [109].

Finally, the influence of the phase adjustment on the short-term frequency stability is investigated and presented in Table 4.8. Here, the digital code of the DCPS of ASIC_v2 is changed to operate the uncoated disk-type resonator at different oscillation frequencies. The relative phase shift represents the phase change with respect to the optimal phase adjustment in the main feedback loop. At the optimum phase adjustment, the oscillation frequency is as close as possible to the resonance frequency of the resonator; therefore, the best short-term frequency stability is obtained at this operating point. As the oscillation frequency moves away from the resonance frequency, the frequency stability deteriorates. This measurement demonstrates the importance of the phase adjustment to achieve better frequency stability.

Table 4.8: Influence of the phase adjustment on short-term frequency stability and oscillation frequency.

Relative Phase Shift	**Short-Term Frequency Stability**	**Oscillation Frequency**
-16.6°	49 mHz	377054 Hz
-10.7°	27 mHz	377071 Hz
-5.4°	18.4 mHz	377086 Hz
-3.6°	15.8 mHz	377090 Hz
optimal	12.9 mHz	377097 Hz
4.8°	14.7 mHz	377115 Hz
7.3°	19.4 mHz	377125 Hz
10.3°	45.9 mHz	377140 Hz

CHAPTER 5

GAS-PHASE CHEMICAL SENSING

This chapter presents the application of the implemented silicon-based microsystem in gas-phase chemical sensing experiments. To evaluate the performance of the microsystem as a chemical sensor, a gas-phase chemical measurement setup was constructed. The operation principle and implementation of this setup are described in Section 5.1. With this setup, gas-phase chemical measurements were performed. Section 5.2 summarizes the measurement results, in which the implemented microsystem is used to detect different concentrations of VOCs.

5.1 Measurement Setup

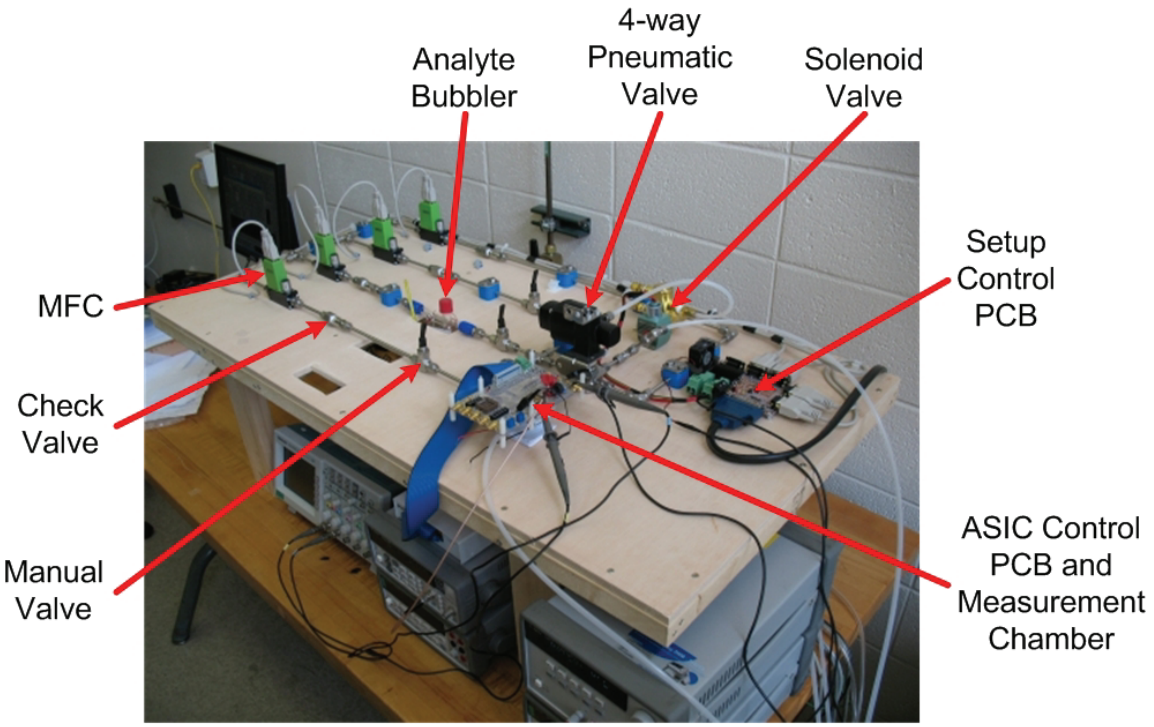

Figure 5.1: Photo of the gas-phase chemical measurement setup.

Figure 5.1 shows a photo of the gas-phase chemical measurement setup, which is able to provide analytes and their mixtures at desired concentrations. The setup is controlled by a PC through a DAQ card and a Labview program, which allows automated measurements.

5.1.1 Operation Principle

This section describes two methods of generating different analyte concentrations for gas-phase chemical sensor testing. Both methods can be utilized in the implemented measurement setup. The first method, shown in Figure 5.2, uses an analyte from a gas cylinder with a known initial concentration of c_i. The analyte is diluted with carrier gas piped through the reference line to obtain a final analyte concentration of c_a. Two mass-flow controllers (MFCs) adjust the analyte and carrier gas flow rates as m_a and m_c, respectively. In this case, the final analyte concentration of c_a is expressed by:

$$c_a = c_i \frac{m_a}{m_c + m_a}. \tag{5.1}$$

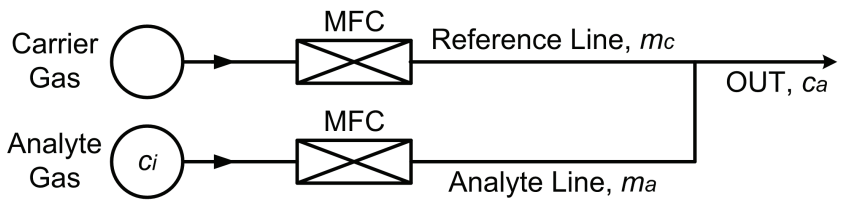

Figure 5.2: Block diagram of gas mixing system consisting of carrier and analyte gas cylinders.

In spite of being simple, this method has three shortcomings. First, the analyte gas has to be streamed through the MFC, which might damage the MFC, if the MFC materials are not compatible with the analyte gas. Second, the final analyte concentration

range is limited by the full-scale (FS) flow ranges of the MFCs for a given initial analyte concentration of the gas cylinder. Finally, analyte cylinders have to be switched each time a different analyte is tested.

Figure 5.3 shows the second method, which uses an analyte bubbler to generate a temperature-dependent initial analyte concentration $c_b(T)$. Figure 5.4 shows a schematic of the analyte bubbler made out of glass. The bubbler contains quartz sand soaked with liquid analyte. A carrier gas is streamed through the quartz sand and becomes loaded with analyte, generating saturated analyte vapor at the output of the bubbler. In this case, the concentration of the analyte in the carrier gas stream depends on the temperature-dependent saturation vapor pressure $p_a(T)$ of the analyte, which is given by the Antoine equation [110] (in units of mmHg)

$$\log p_a(T) = A - \frac{B}{C+T}, \tag{5.2}$$

where T is the temperature, and A, B, and C are analyte specific constants. The saturation vapor pressure $p_a(T)$ of the analyte is equal to its partial pressure in the analyte gas stream, which can be converted into the initial analyte concentration $c_b(T)$ in units of parts-per-million (ppm) with the relation [111]:

$$c_b(T) = 10\, p_a(T). \tag{5.3}$$

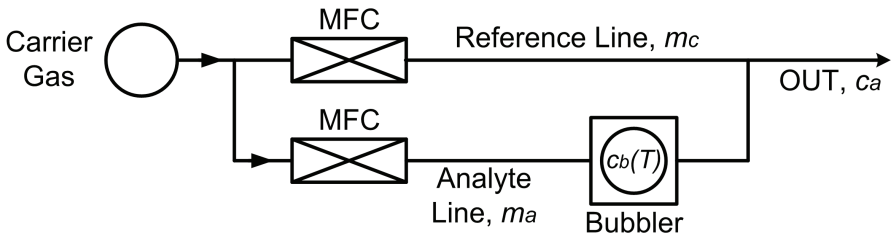

Figure 5.3: Block diagram of gas mixing system based on analyte-filled bubblers.

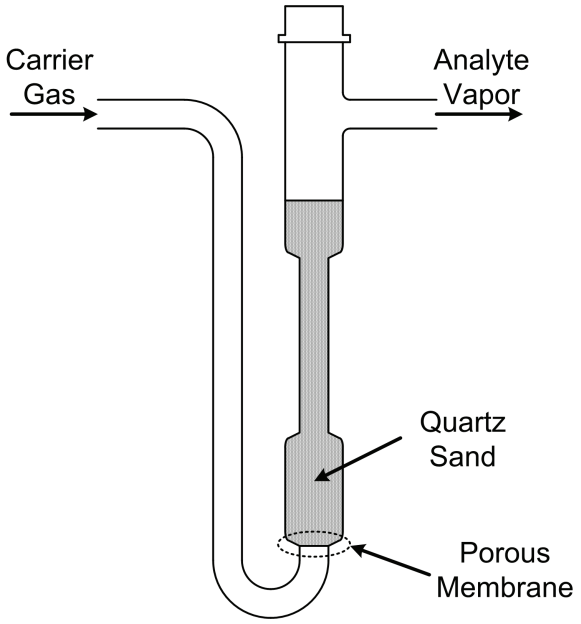

Figure 5.4: Schematic diagram of the bubbler.

The initial analyte concentration $c_b(T)$ is then diluted with carrier gas piped through the reference line to obtain a final analyte concentration of c_a. Two MFCs adjust the carrier gas flows in the analyte line and the reference line as m_a and m_c, respectively. In this case, the final analyte concentration c_a is expressed by:

$$c_a = c_b(T)\frac{m_a K}{m_c + m_a K} = c_b(T)\frac{m_a\left(1+\frac{p_a(T)}{p_{air}}\right)}{m_c + m_a\left(1+\frac{p_a(T)}{p_{air}}\right)}, \tag{5.4}$$

where p_{air} is the air pressure (approximately 10^5 Pa), and K is a correction factor included to account for the flow rate change in the analyte line as a result of the added analyte from the bubbler [111].

Despite being more complicated to implement compared to the first method, the bubbler technique is more flexible since a wide range of analyte concentrations can be obtained by only changing the temperature of the bubbler. Also, different analytes can be easily tested by refilling the bubbler with the desired liquid analyte. However, the bubbler

technique is limited to analytes that are in their liquid phase at the temperature of the bubbler.

In the implemented setup, the bubbler is immersed in a water bath. The water bath has a large thermal time constant, which prevents abrupt changes in the temperature of the bubbler and therefore stabilizes the bubbler temperature. Since the water bath is currently not temperature controlled, the bubbler temperature is fixed at room temperature.

5.1.2 Implementation

Figure 5.5 presents a schematic diagram of the implemented measurement setup, which is composed of two analyte lines, L1 and L2, and two carrier gas lines, L3 and L4. Nitrogen (ultra high purity grade, Airgas) is used as a carrier gas, which is supplied by a gas cylinder. The output pressure of the carrier gas cylinder is held at approximately 2.5 bar to overcome pressure drops in the system because of the MFCs, the analyte bubbler, and the measurement chamber. Analyte line L1 is connected to an analyte gas cylinder to generate analyte concentrations based on the first method explained in the previous section. In this case, the analyte gas must be compatible with the materials in the MFC in order to not damage it. The second analyte line L2 uses the second method and thus employs a bubbler to create saturated vapor of the analyte. Carrier gas line L3 is used to dilute the analyte to establish the desired concentration for both methods. Finally, carrier gas line L4 provides the reference gas to the measurement chamber in the purge mode.

A 4-way pneumatic valve (SS-43YF2-31S, Swagelok) sequentially connects the analyte gas and the carrier gas to the measurement chamber. During the analyte mode, the analyte gas is applied to the chamber, while the carrier gas is exhausted. During the purge mode, the 4-way valve switches, and carrier gas purges the measurement chamber. The 4-way valve provides sharp transients in the analyte concentrations and makes the setup suitable to study transient effects in the tested chemical sensors. A solenoid valve (8321

G001, Asco Valve) controls the pressured air to switch the 4-way valve. A flow meter is connected to the output of the setup to measure the overall flow through the measurement chamber.

The carrier and analyte lines can be closed with manual valves (SS-1GS4, Swagelok). Check valves are included to prevent the back flow of gases to the MFCs and to avoid pressure spikes that might occur and affect the flow through the MFCs when the 4-way valve is switched. The setup is constructed using Swagelok fittings. The analyte and carrier gases from the cylinders are carried using tygon PVC tubing. Polyethylene tubing is used for exhaust and air lines. The rest of the setup employs 316 stainless steel tubing with an outer diameter of 1/4 inches.

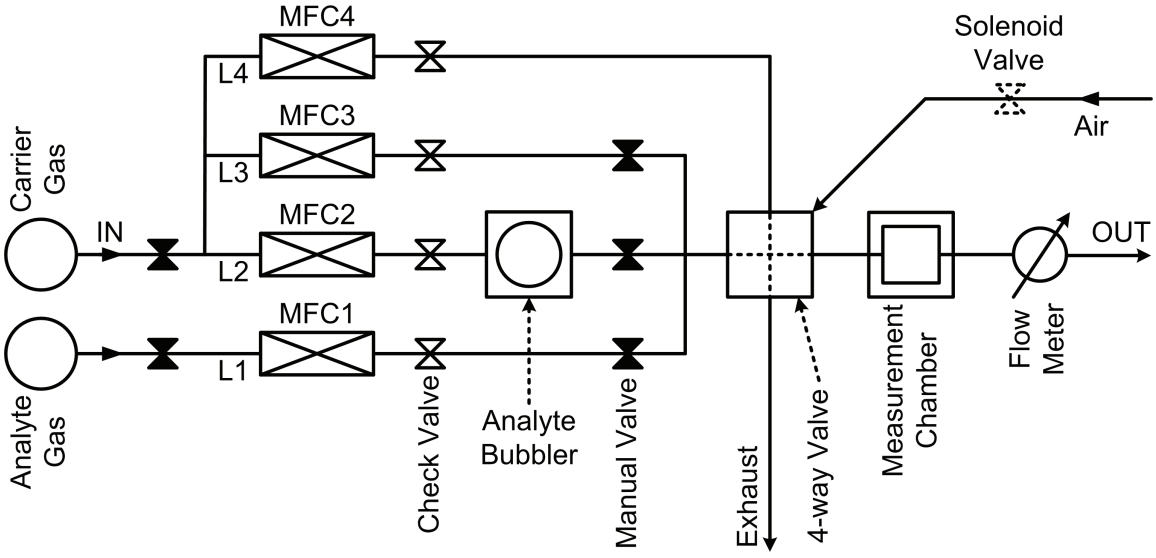

Figure 5.5: Schematic diagram of the chemical measurement setup.

Four MFCs (SFC4100 UA6 N2, Sensirion) adjust the gas flow rates in the analyte and carrier lines. For the analyte lines L1 and L2, MFCs (MFC1 and 2) with a full-scale flow rate of 50 ml/min are used. The carrier lines L3 and L4 utilize MFCs (MFC 3 and 4)

with a full-scale flow rate of 200 ml/min. The setup uses a maximum total flow of 200 ml/min. The minimum flows of the MFCs are limited to 10 % of FS, when the accuracy and repeatability specifications of the MFCs are considered [112]. In this case, assuming a 200 ml/min total flow, the minimum analyte concentration that can be obtained is 2.5 % of the saturated analyte vapor concentration in the bubbler.

5.1.3 Measurement Chamber

A gas-tight measurement chamber was designed and fabricated in the machine shop of the School of Mechanical Engineering at Georgia Tech. Figure 5.6 shows photos of the measurement chamber, which is composed of two pieces, a bottom and a top manifold.

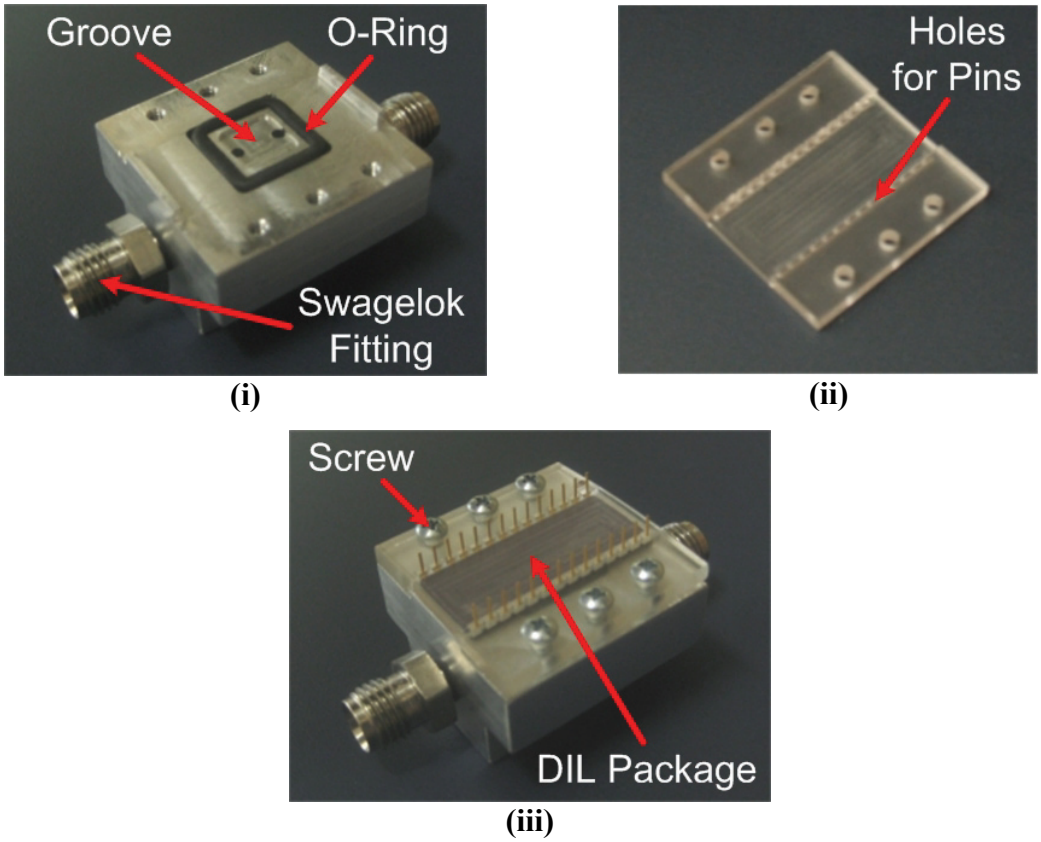

Figure 5.6: Photo of the two-piece measurement chamber: (i) bottom manifold with the o-ring, (ii) top manifold on which the resonator chip is mounted on a 28-pin DIL package, and (iii) the two manifolds screwed together with inserted sensor package.

The bottom manifold is made of aluminum and contains a trench where a chemically-resistant Viton o-ring is placed. The resonator chip is mounted in a 28-pin DIL package, which is mounted on the top manifold. The pins of the DIL package go through holes in the top manifold for electrical connections. Since the top manifold is never in contact with the analyte, it is made of acrylic for electrical insulation and easy fabrication. The top manifold together with the DIL package is flipped and placed on top of the bottom manifold (see Figure 5.6 (iii)). In this way, the edges of the cavity of the DIL package (see Figure 5.7 (i)) align with the o-ring. Using six screws, the top manifold is pressed down to obtain a gas-tight connection. The measurement chamber is connected to the stainless steel tubing of the measurement setup using Swagelok fittings.

Flow channels in the bottom manifold allow the gas flow through the measurement chamber as illustrated in Figure 5.7 (i), which shows the schematic diagram of the measurement chamber. The volume of the chamber, which is approximately 0.2 ml is determined by the cavity of the DIL package, where the sensor chip is placed, and the groove in the bottom manifold. This volume directly affects the transient response of the sensor. The chamber is designed to keep the chamber volume as small as possible to minimize the response time of the sensor and at the same time to allow uniform flow of the gas through the chamber, which is verified by the finite-element simulations carried out with COMSOL as shown in Figure 5.7 (ii). In this simulation, a constant normal inflow velocity is applied to the inlet. The outlet pressure is set to zero. The chamber is assumed to be filled with air except the place where the sensor chip is located. The velocity fields in the unit of m/s are shown as slices in this figure.

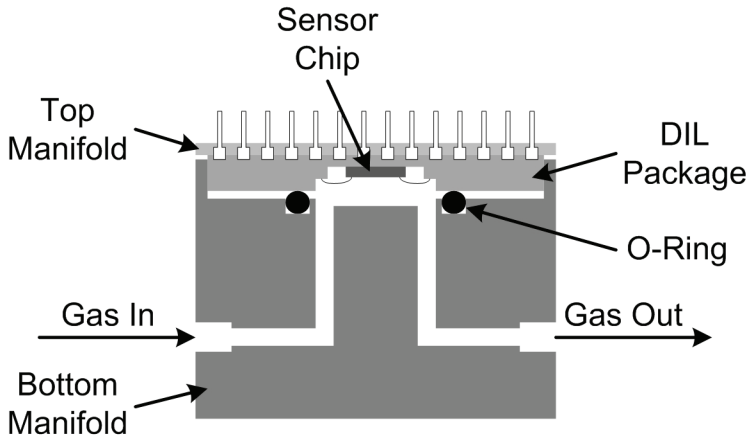

(i)

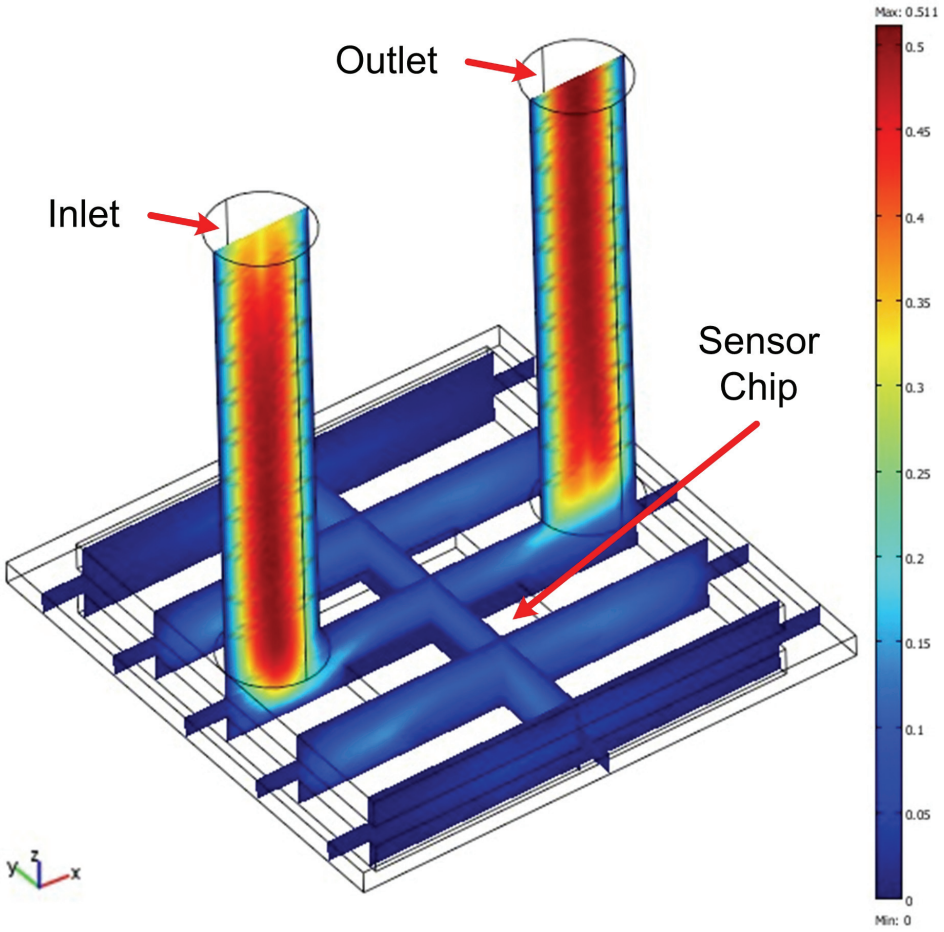

(ii)

Figure 5.7: (i) Schematic diagram of the measurement chamber and (ii) finite-element simulation result showing the uniform gas flow through the chamber.

5.1.4 Setup Control

The measurement setup is controlled by a PC with a DAQ card (PCI NI-6251, National Instruments) and a Labview program. A custom-made PCB is used as an interface between the setup and the PC. The PCB includes a four-output DAC that generates the analog voltages used to adjust the flow rates of the MFCs. The MFCs are read-out via the analog input channels of the DAQ card to monitor the flow rate. A high-voltage MOSFET switch is also included on the PCB for switching the solenoid valve. The digital control signals for the MFCs and the MOSFET switch are produced by the digital output channels of the DAQ card. The PCB is powered with 15 V, which is directly applied to the MFCs as a supply voltage. The other necessary voltages, 5 V for the DAC and 24 V for the pneumatic valve, are produced by a regulator and a DC-DC converter, respectively. A schematic diagram of the off-chip electronics is given in Appendix B.

The Labview program allows the user to enter the total flow rate, 10 different analyte flow rates that will be applied consecutively, and the durations of analyte and purge modes. The program then calculates the necessary voltages and controls the DAQ card accordingly. The flow rates obtained from the MFCs are displayed by the program.

5.2 Experimental Results

To perform gas-phase chemical tests, a cantilever was spray-coated with poly-isobutylene (PIB) as the chemically-sensitive polymer film. Figure 5.8 (i) and (ii) show the micrographs of the cantilever before and after spray-coating, respectively. The PIB-coated cantilever with a resonance frequency of 368.5 kHz was mounted in a 28-pin DIL package and then attached to the measurement chamber as described in the previous section. The PCB including ASIC_v2 was placed on the measurement chamber, and the resonator was connected to the PCB using the ZIF-socket on the backside of the PCB

(see Figure 4.22). The Wheatstone bridge bias and DC-offset voltages were adjusted to ±1 V and ±2 V, respectively. AC excitation signal amplitudes of approximately 800 mV_{pp} were used.

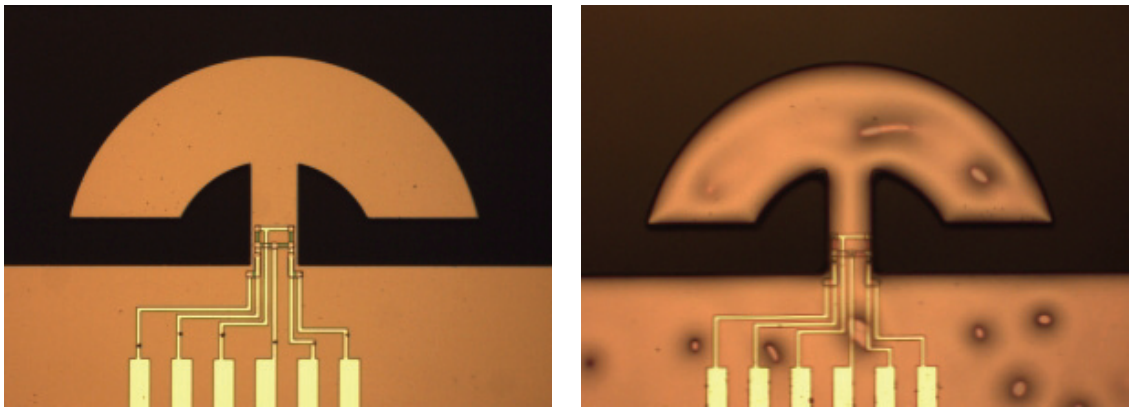

(i) **(ii)**

Figure 5.8: Micrographs of a cantilever-type microresonator (i) before and (ii) after spray-coating. The polymer film thickness is approximately 1.5 μm.

During the chemical measurements, different concentrations of VOCs, such as benzene, toluene and m-xylene have been detected. In each measurement, the bubbler was refilled with the desired liquid analyte. Reference gas (nitrogen) and analyte gas were alternately applied to the measurement chamber in approximately 5 minute intervals. The analyte concentration was ramped up or down after every analyte injection by adjusting analyte and reference gas flow rates. The measurement was performed at a temperature around 23° C. The saturation vapor pressure of the analytes at 23° C has been calculated using Eq. (5.2) and has been used to estimate the initial analyte concentration $c_b(T)$. (The saturation vapor pressures of the analytes of interest at different temperatures are listed in Appendix C.) With this initial value, the final analyte concentration c_a is estimated using Eq. (5.4) for given analyte and reference gas flow rates.

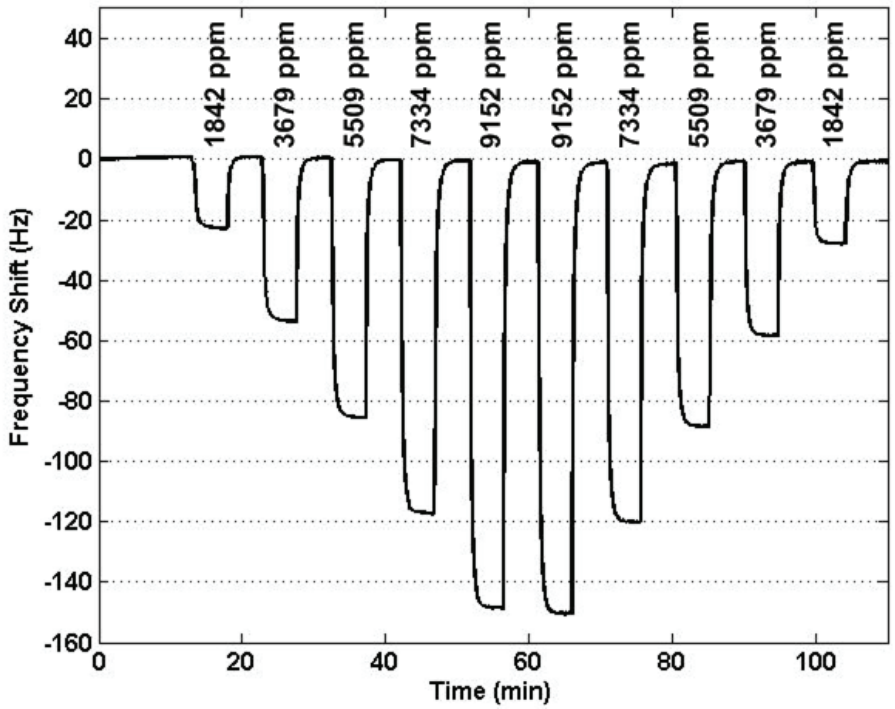

Figure 5.9: Frequency shift of the PIB-coated resonator as a function of time; the microsensor is subsequently exposed to different benzene concentrations.

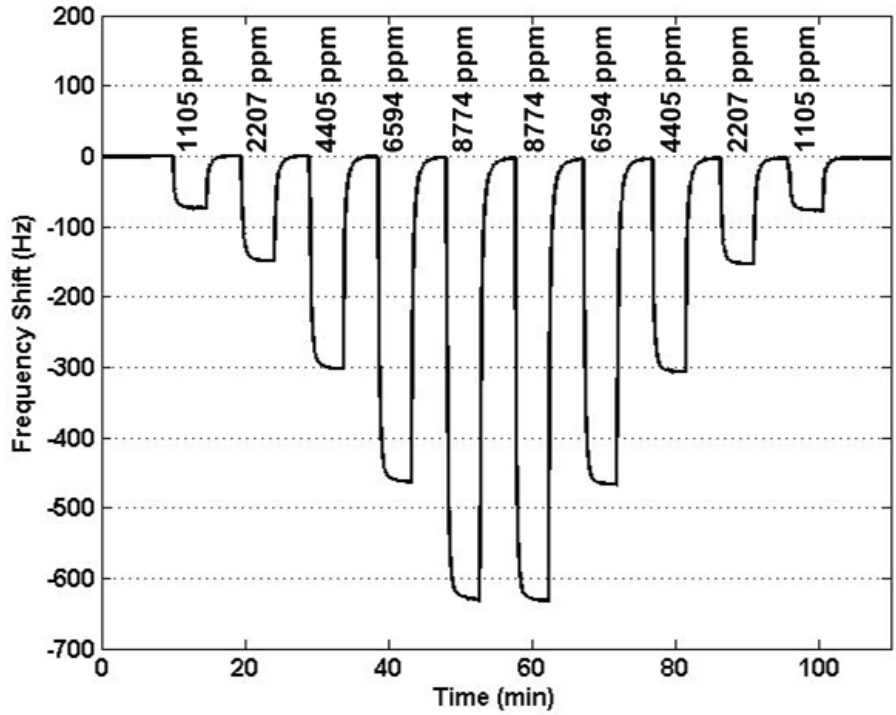

Figure 5.10: Frequency shift of the PIB-coated resonator as a function of time; the microsensor is subsequently exposed to different toluene concentrations.

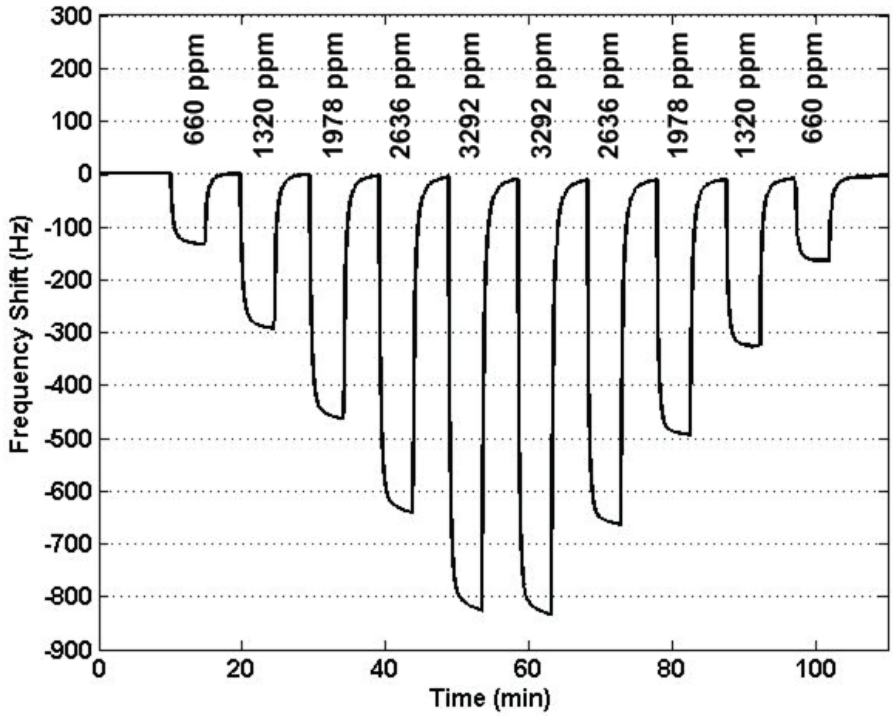

Figure 5.11: Frequency shift of the PIB-coated resonator as a function of time; the microsensor is subsequently exposed to different m-xylene concentrations.

Figures 5.9, 5.10 and 5.11 show the frequency shifts upon exposure to different concentrations of benzene, toluene and m-xylene in the gas-phase, respectively. The oscillation frequency shifts down because of the mass loading, when the resonator is exposed to the analyte gas. Figure 5.12 demonstrates the response of the PIB-coated resonator to toluene with a concentration of 1105 ppm. The time to reach 90 % of the full response is approximately 45 sec as shown in the close-up view.

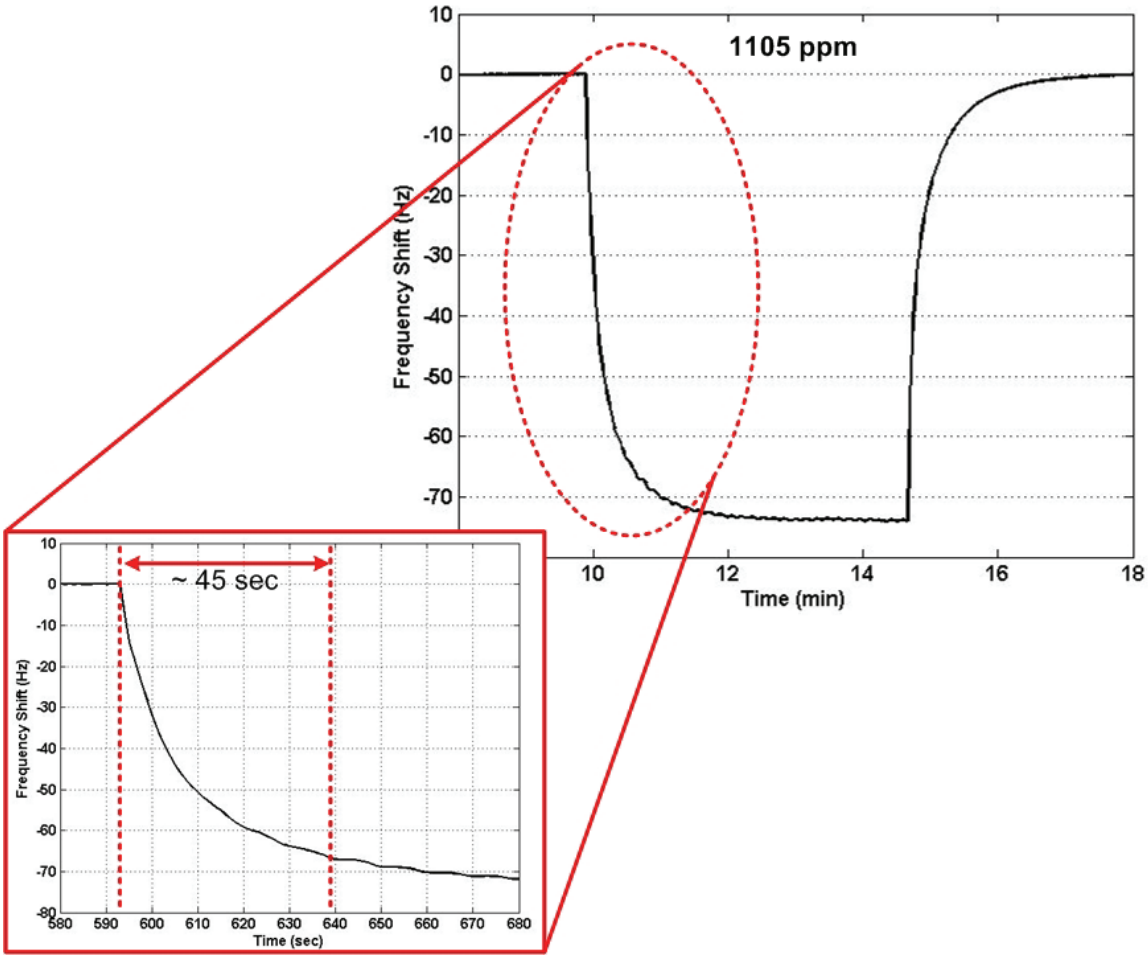

Figure 5.12: Frequency shift of PIB-coated resonator as a function of time when exposed to toluene with a concentration of 1105 ppm, and close-up view showing the response time.

Figure 5.13 shows the measured frequency change of the PIB-coated resonator as a function of the analyte concentration when the concentration is ramped up (red symbols) and ramped down (blue symbols). The frequency change shows almost a linear increase with increasing analyte concentration and good reproducibility. From the linear fits (lines) to the measured data, the sensitivity of the microsystem for benzene, toluene, and m-xylene is extracted as 16.1 mHz/ppm, 70.7 mHz/ppm and 244.1 mHz/ppm, respectively. The sensitivity increases with the decreasing saturation vapor pressure of

the analytes at a given temperature, since a lower saturation vapor pressure results in a higher partition coefficient.

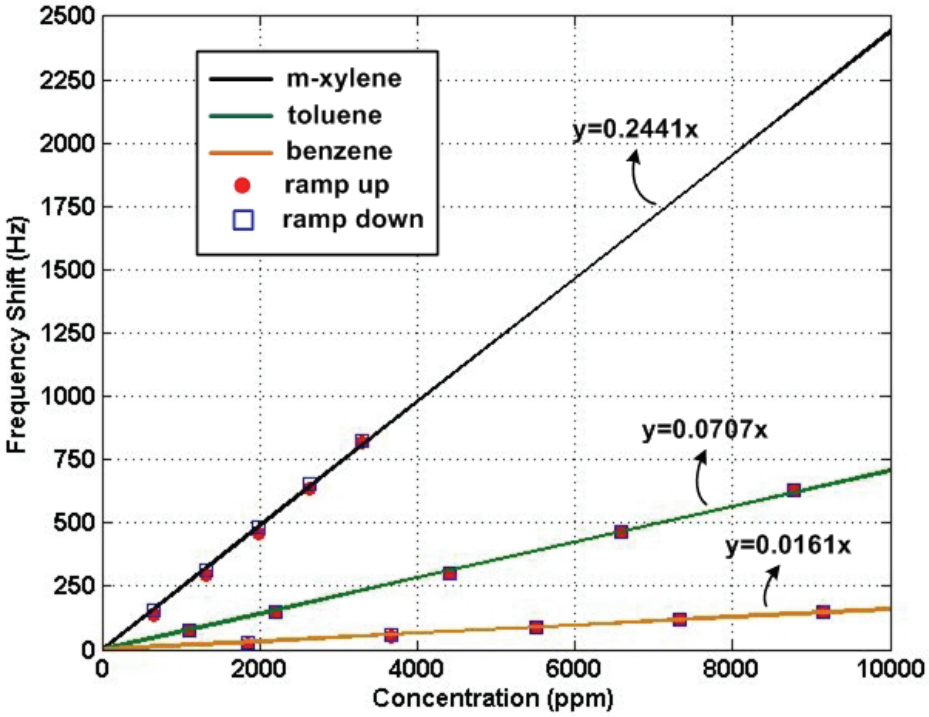

Figure 5.13: Measured frequency change of the PIB-coated resonator as a function of the analyte concentration when the concentration is ramped up (red symbols) and ramped down (blue symbols), and the linear fits to the measurement data (lines).

Finally, Figure 5.14 shows the short-term frequency fluctuations of the PIB-coated resonator. With a short-term frequency stability of 28.5 mHz extracted with the Allan variance method, the LOD of the sensor system for benzene, toluene and m-xylene is calculated by using Eq. (2.17) given in Section 2.4 as 5.3 ppm, 1.2 ppm and 0.35 ppm, respectively. The LOD for toluene achieved in this work is better than the one obtained with a similar cantilever-based chemical microsystem [58].

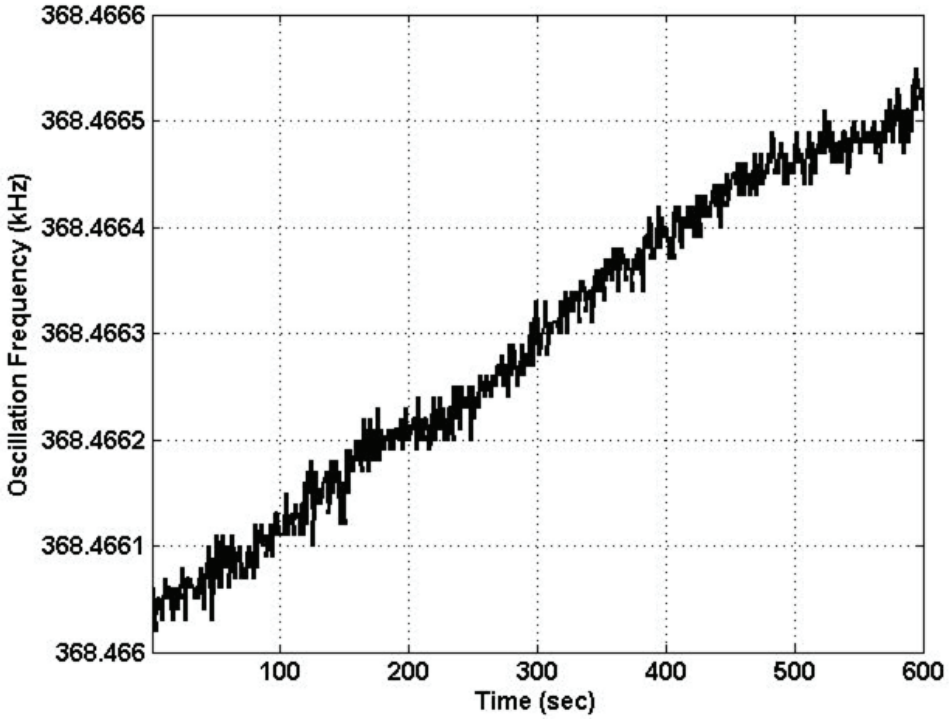

Figure 5.14: Frequency fluctuations of the PIB-coated resonator as a function of time.

CHAPTER 6

FREQUENCY DRIFT COMPENSATION

The resonance frequency of a microresonator is affected by changes in its mass and its stiffness as mentioned in Chapter 2 (see Eq. (2.15)). If the microresonator is used as a mass-sensitive chemical sensor, it is exposed to the environment in order to detect the analytes of interest. In this case, any changes in the environmental conditions, such as changes in temperature, humidity or pressure [113], but also microstructure aging [114] might affect the stiffness of the microresonator and hence cause stiffness-induced resonance frequency changes. As a result, the resonance frequency varies in time and generates a sensor response that is very similar to the one generated by a slowly changing analyte concentration. In this situation, it becomes very difficult, if not impossible, to determine if the sensor response, i.e. frequency change, is the result of drift or the presence of a chemical analyte. Therefore, frequency drift caused by environmental disturbances limits the sensor resolution especially in long-term monitoring applications with slowly changing analyte signatures and has to be compensated in order to obtain high sensor resolution.

To address the need for compensating drift effects, ASIC_v2 employs a frequency drift compensation (FDC) method. In this method, ASIC_v2 uses a controlled stiffness modulation generated by the FDC loop to track the changes in the resonator's Q-factor in response to variations in the environmental conditions. The measured Q-factor is then used to compensate for the frequency drift using the relation between Q-factor and resonance frequency obtained through an initial calibration step. This method has been previously applied for compensation for frequency drift caused by temperature variations with off-chip electronics [115]. Here, this compensation scheme is successfully

implemented with CMOS-integrated electronics into a closed-loop chemical sensing system.

This chapter first gives an overview of compensation methods that have been proposed in the literature in Section 6.1. Then, the principle of the implemented FDC method is explained in Section 6.2. At the end, Section 6.3 presents experimental results, which demonstrate the feasibility of the FDC method in gas-phase chemical measurements.

6.1 Overview of Current Frequency Compensation Methods

Several approaches have been investigated to compensate for frequency drift induced by environmental effects. One of the most common approaches is the co-integration of a temperature sensor close to the microresonator [116]. In this approach, a temperature-sensitive device monitors the temperature, and then the temperature-induced frequency drift is compensated for by using a relation between temperature and resonance frequency obtained through a calibration step.

A second compensation method incorporates a reference resonator in addition to the one used as sensing resonator [117]. In this method, the sensing resonator is coated with a sensitive layer and responds to both analytes and environmental variations, while the reference resonator is kept uncoated and hence responds primarily to environmental changes. If the mechanical properties of both resonators are the same, the resonators' response to environmental changes will be almost the same. In this case, the difference between the resonance frequencies of the sensing and reference resonators gives the frequency shift caused by analytes.

Another compensation approach uses two resonance modes of a single resonator [118]. The resonator is excited at two different resonance modes with different temperature coefficient of frequencies (TCfs). The difference between the resonance

frequencies of the modes is a measure of the temperature of the resonator and is used to compensate for temperature-induced frequency drift.

In another technique, thin film induced stress is used for passive temperature compensation [119]. Here, the negative TCf of the resonator because of a compressive stress is compensated for by including an additional thin film in the resonator to generate an appropriate tensile stress and thus obtain a resulting TCf of zero.

Despite of their successful uses for frequency drift compensation, all of the above methods require either additional sensing devices, device-specific fabrication steps, or certain resonator geometries for proper excitation and detection. Thus, their applications are limited.

The Q-factor is related to the mechanical properties of the resonator, namely its stiffness, mass, and damping. Therefore, any variation in these properties in response to a measurand causes a Q-factor change. In particular, this means that the response of a resonant sensor to environmental disturbances can be monitored and compensated via the Q-factor. This fact has been exploited by using the Q-factor to sense e.g. temperature [120], fluidic properties such as viscosity and density [120, 121], and pressure [122].

In addition to monitoring environmental variations, the Q-factor can be used to compensate for frequency drift caused by them. In a previous study [123], the Q-factor was utilized as a temperature sensor and used to compensate for temperature-induced frequency drift. In that study, the Q-factor was obtained from the oscillation amplitude of the microresonator, requiring precise A/D conversion. In that case, the advantages of the resonant sensor, in particular the use of a frequency signal that can be easily digitized, are not fully utilized. On the contrary, in the FDC method implemented in this research, the Q-factor is solely obtained from frequency measurements without the need for additional sensing devices and monitored along with the measurand-induced frequency shift during the normal closed-loop sensor operation of the resonator. In addition, the proposed

method is applicable to all resonant microstructures featuring excitation and detection elements.

6.2 Principle of Frequency Drift Compensation

Figure 6.1 presents a schematic diagram showing the concept of the implemented FDC method. In addition to the main feedback (MF) circuit to start and sustain oscillation at the resonance frequency, a second feedback circuit, the so-called frequency drift compensation (FDC) circuit, generates a signal in-phase with the deflection of the resonator. This signal is applied to the resonator excitation elements in addition to the signal generated by the MF circuit and modulates the effective stiffness of the resonator [124]. By controlling the polarity of the modulation signal using a switch in the FDC circuit, the effective stiffness of the resonator can be either reduced or increased. As a result, the resonance frequency of the harmonic oscillator is changed in response to the modulated effective stiffness.

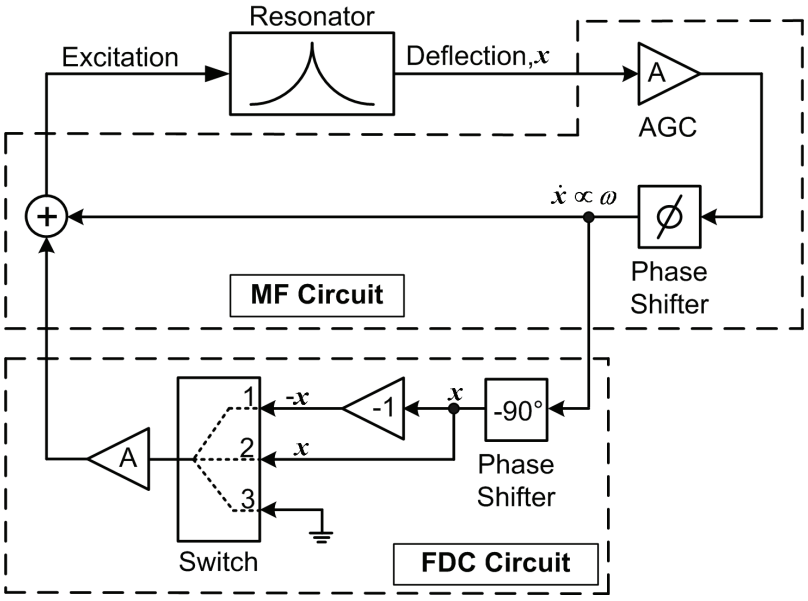

Figure 6.1: Schematic diagram showing the concept of the FDC method.

The motion of the resonator with the MF circuit and enabled FDC circuit can be described by

$$m\ddot{x} + b\dot{x} + kx = \psi_{MF}\frac{\dot{x}}{|\dot{x}|} \mp \psi_{FDC}\frac{x}{|x|}, \tag{6.1}$$

where ψ_{MF} and ψ_{FDC} are the force amplitudes of the MF and FDC circuits, respectively. In this case, the system equation for the resonator shown in Figure 6.1 is expressed by

$$m\ddot{x} + \left[b - \frac{\psi_{MF}}{|\dot{x}|}\right]\dot{x} + \left[k \pm \frac{\psi_{FDC}}{|x|}\right]x = 0. \tag{6.2}$$

Under steady-state oscillation, the force generated by the MF circuit is the same as the damping force of the resonator to sustain a constant-amplitude oscillation at the resonance frequency. In this case, the magnitudes of the steady-state vibration velocity $\dot{x}$ and the vibration amplitude x of the resonator embedded in the feedback circuit are obtained from Eq. (6.2) by forcing the effective damping force (second term in Eq. (6.2)) to zero, i.e.

$$|\dot{x}| = \frac{\psi_{MF}}{b}, \quad |x| = \frac{\psi_{MF}}{b\omega_o}. \tag{6.3}$$

As a result, the equation of motion becomes

$$m\ddot{x} + \left[k \pm \frac{\psi_{FDC}}{\psi_{MF}} b\omega_o\right]x = 0. \tag{6.4}$$

Using the relation $Q = k\, b^{-1}\, \omega_0^{-1}$, Eq. (6.4) can be expressed in terms of the Q-factor by

$$m\ddot{x} + \left[k\left(1 \pm \frac{\psi_{FDC}}{\psi_{MF}}\frac{1}{Q}\right)\right]x = 0. \tag{6.5}$$

Equation (6.5) reveals that the relative stiffness change induced by the modulation loop is directly related to the Q-factor of the resonator. In fact, the stiffness is modified by the FDC circuit by the factor

$$1 \pm \frac{\psi_{FDC}}{\psi_{MF}} \frac{1}{Q}. \tag{6.6}$$

It should be noted that Eqs. (6.1) – (6.6) only hold when the excitation signals generated by the MF and FDC circuits are exactly phase matched with the vibration velocity $\dot{x}$ and the deflection of the resonator x, respectively. In the realized system, the phase tuning is done by an all-pass filter as described before, and there is a possibility of a tuning error, which will introduce an error in the estimated Q-factor. To minimize this phase tuning error, the polarity of the signal generated by the FDC circuit is altered to obtain both positive and negative stiffness modulations using a switch in the FDC circuit, resulting in an increase or decrease in the resonance frequency. In this case, the resonance frequencies with positive and negative stiffness modulation, respectively, become

$$\omega_{pos} = \sqrt{\frac{k}{m}\left(1 + \frac{\psi_{FDC}}{\psi_{MF}} \frac{1}{Q}\right)}, \quad \omega_{neg} = \sqrt{\frac{k}{m}\left(1 - \frac{\psi_{FDC}}{\psi_{MF}} \frac{1}{Q}\right)}. \tag{6.7}$$

From the ratio of the frequencies $\omega_{pos}/\omega_{neg}$, the Q-factor of the resonator can be calculated as

$$Q = \frac{\psi_{FDC}}{\psi_{MF}} \frac{\alpha + 1}{\alpha - 1}, \quad \alpha = \left(\frac{\omega_{pos}}{\omega_{neg}}\right)^2 \quad . \tag{6.8}$$

Therefore, by measuring the resonance frequency changes caused by the periodically enabled FDC circuit, the Q-factor (or the relative Q-factor change) of a microresonator can be extracted and tracked during closed-loop sensor operation. If the influence of the Q-factor on the resonance frequency is known, the measured Q-factor data can be used to compensate for frequency drift. In this study, an initial calibration step establishes the relation between the relative Q-factor dQ/Q and frequency $d\omega_0/\omega_0$ changes.

6.3 Experimental Results

Figure 6.2 shows the schematic diagram of the FDC circuit implemented in ASIC_v2 and its connections to the MF circuit. The phase-shifted main oscillation signal from the MF circuit is connected to the FDC circuit input, where it is -90° phase shifted by the DCPS to generate a signal in-phase with the deflection of the resonator. The DCPS used in the FDC circuit is the same one used in the MF circuit and described in detail in Chapter 4. A cross-switch is implemented with CMOS transmission gates and connected at the output of the DCPS. The cross-switch periodically enables/disables the FDC circuit. When the FDC circuit is enabled, the cross-switch position determines the polarity of the compensation signal. A fully-differential variable-gain amplifier (VGA) is included to adjust the modulation signal amplitude ψ_{FDC} and, at the same time, to generate the out-of-phase compensation signals (V_{comp1} and V_{comp2}). The gain of the VGA is given by

$$A_v = -\frac{R_4}{R_3} \quad . \tag{6.9}$$

To be able to adjust the gain, R_4 is implemented with switched-resistors with a unit resistance of 2.5 kΩ. With R3 = 20 kΩ, the gain of the VGA can be adjusted between 0.125 V/V and 1 V/V in eight steps. The op-amp used in the VGA is the same fully-differential folded-cascode op-amp used in the summing amplifier and described in detail in Chapter 4. The compensation signals from the VGA are connected to the summing amplifier in the MF circuit and added to the main oscillation signal. With a gain of -1 V/V obtained by selecting $R_2 = R_1 = 20$ kΩ, the summing amplifier only changes the polarity of the compensation signals.

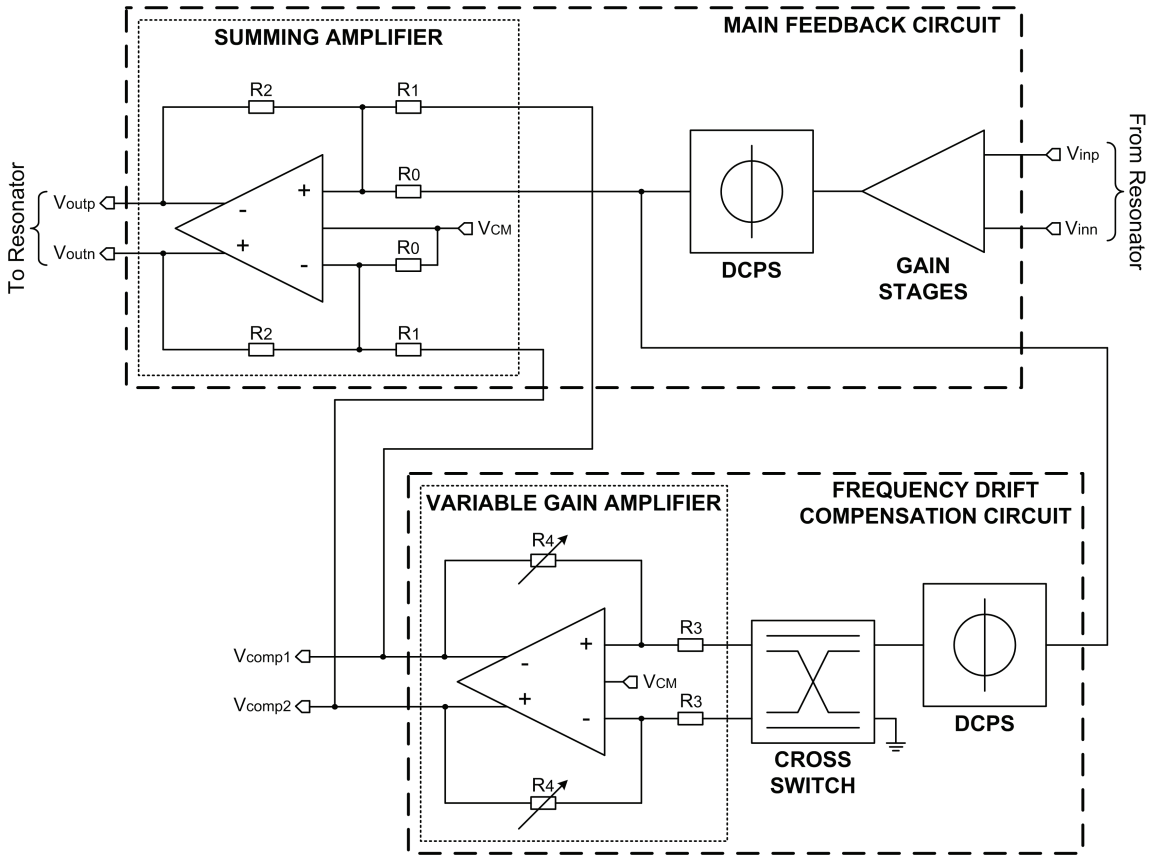

Figure 6.2: Schematic diagram of the FDC circuit implemented in ASIC_v2 and its connections to the MF circuit.

To demonstrate the feasibility of the drift compensation scheme for mass-sensitive chemical microsensors, gas-phase chemical measurements have been performed using ASIC_v2 interfaced to the same PIB-coated microresonator employed in the chemical measurements described in Chapter 5. Before performing chemical measurements, the relation between the extracted Q-factor change and the measured resonance frequency has been obtained with a calibration measurement. For both measurements, the measurement setup explained in Chapter 5 is used with the resonator being mounted on the measurement chamber.

During the measurements, the Wheatstone bridge bias and DC-offset voltages are set to ±1 V and ±2 V, respectively. The output signal amplitudes of the MF and FDC

circuits of ASIC_v2 are adjusted to be approximately 760 mV_{pp} and 340 mV_{pp}, respectively. The negative and positive stiffness modulations (switch position 1 and 2 in Figure 6.1) are periodically enabled for 2 seconds each, every 30 seconds. Figure 6.3 shows the measured signals at the outputs of the MF circuit, V_{outp} (blue line), and FDC circuit, V_{comp1} (red line) and V_{comp2} (green line), when (i) the FDC circuit is disabled, (ii) the FDC is enabled with a positive stiffness modulation, and (iii) the FDC is enabled with a negative stiffness modulation. The microresonator with a resonance frequency of approx. 368.5 kHz exhibits a frequency change ($f_{pos} - f_{neg}$) of approximately 198 Hz by the enabled FDC circuit as shown in Figure 6.4. Generally, a larger Q-factor yields a smaller frequency change ($f_{pos} - f_{neg}$).

In the calibration measurement, the temperature of the resonator is varied by means of a thermoelectric cooler placed under the measurement chamber. This way, a temperature-induced frequency drift is obtained. The oscillation frequency is measured using a frequency counter and is shown in Figure 6.5. A temperature increase/decrease of approximately 10° C causes a total frequency decrease/increase of around 200 Hz. The Q-factor is tracked with the help of the FDC circuit and extracted using Eq. (6.8). The measured relative frequency change and the extracted relative Q-factor change as a function of time are shown in Figure 6.6 (i) and (ii), respectively.

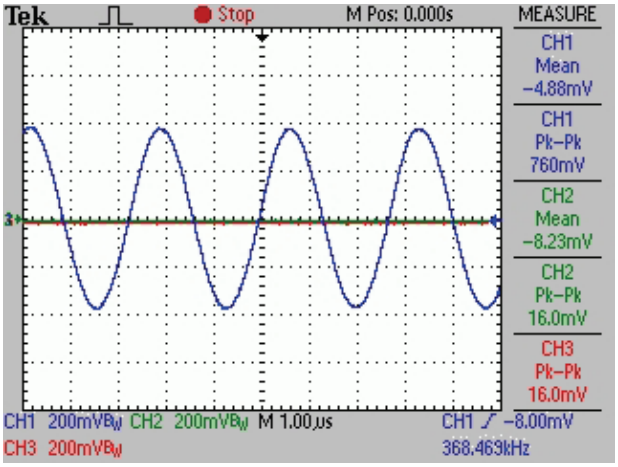

(i)

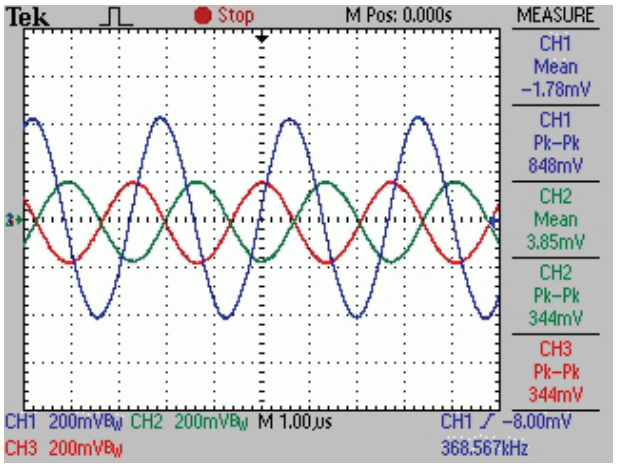

(ii)

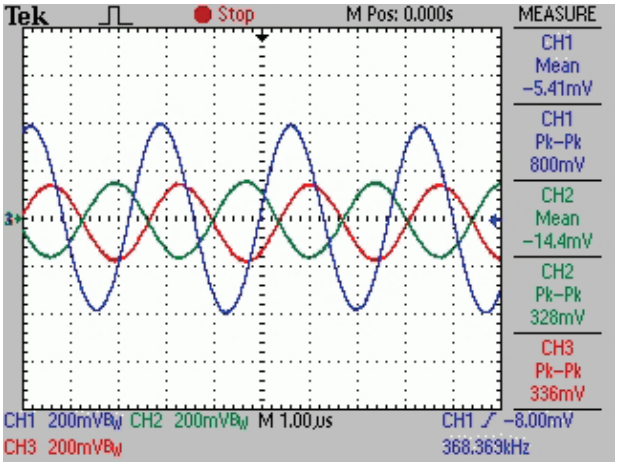

(iii)

Figure 6.3: Measured signals at the outputs of the MF circuit, V_{outp} (blue line), and FDC circuit, V_{comp1} (red line) and V_{comp2} (green line), when (i) the FDC circuit is disabled, (ii) the FDC is enabled with positive stiffness modulation, and (iii) the FDC is enabled with negative stiffness modulation.

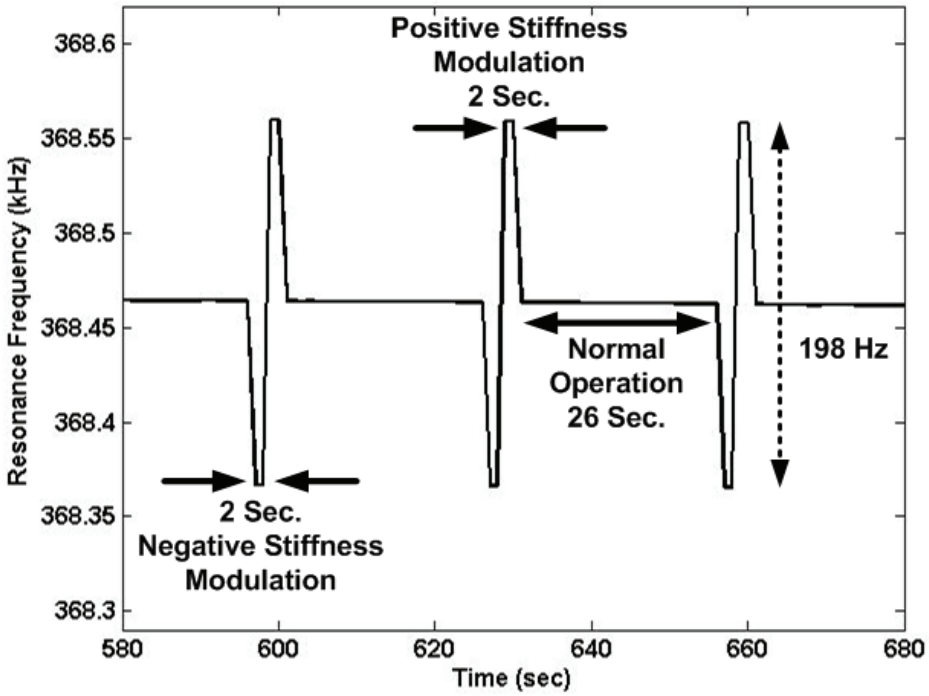

Figure 6.4: Closed-loop oscillation frequency with periodically enabled positive and negative stiffness modulation.

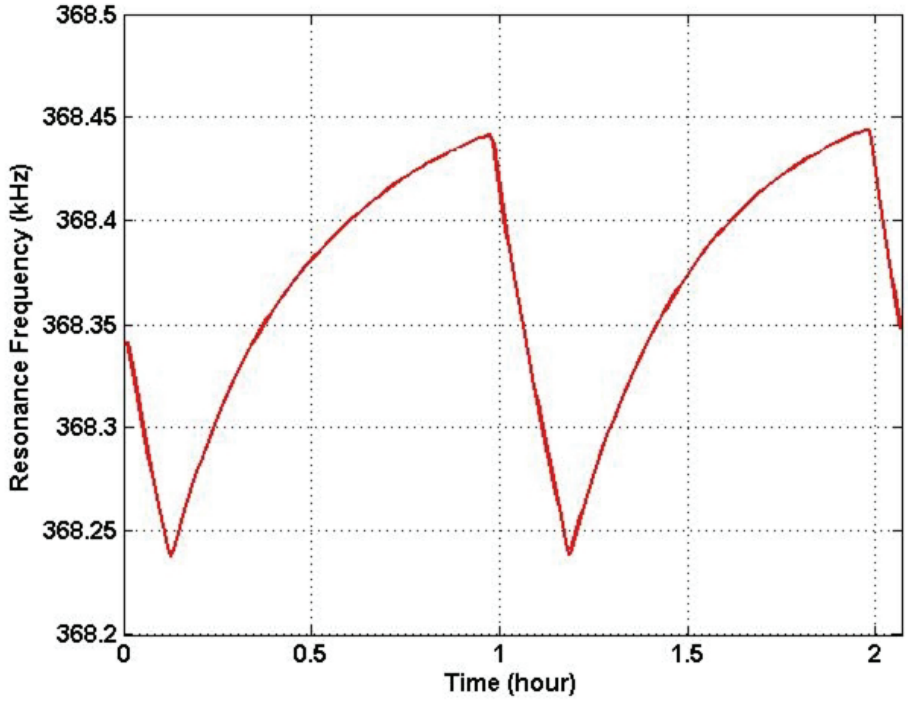

Figure 6.5: Closed-loop oscillation frequency change during the calibration measurement in which the temperature of the resonator is varied using a thermoelectric cooler.

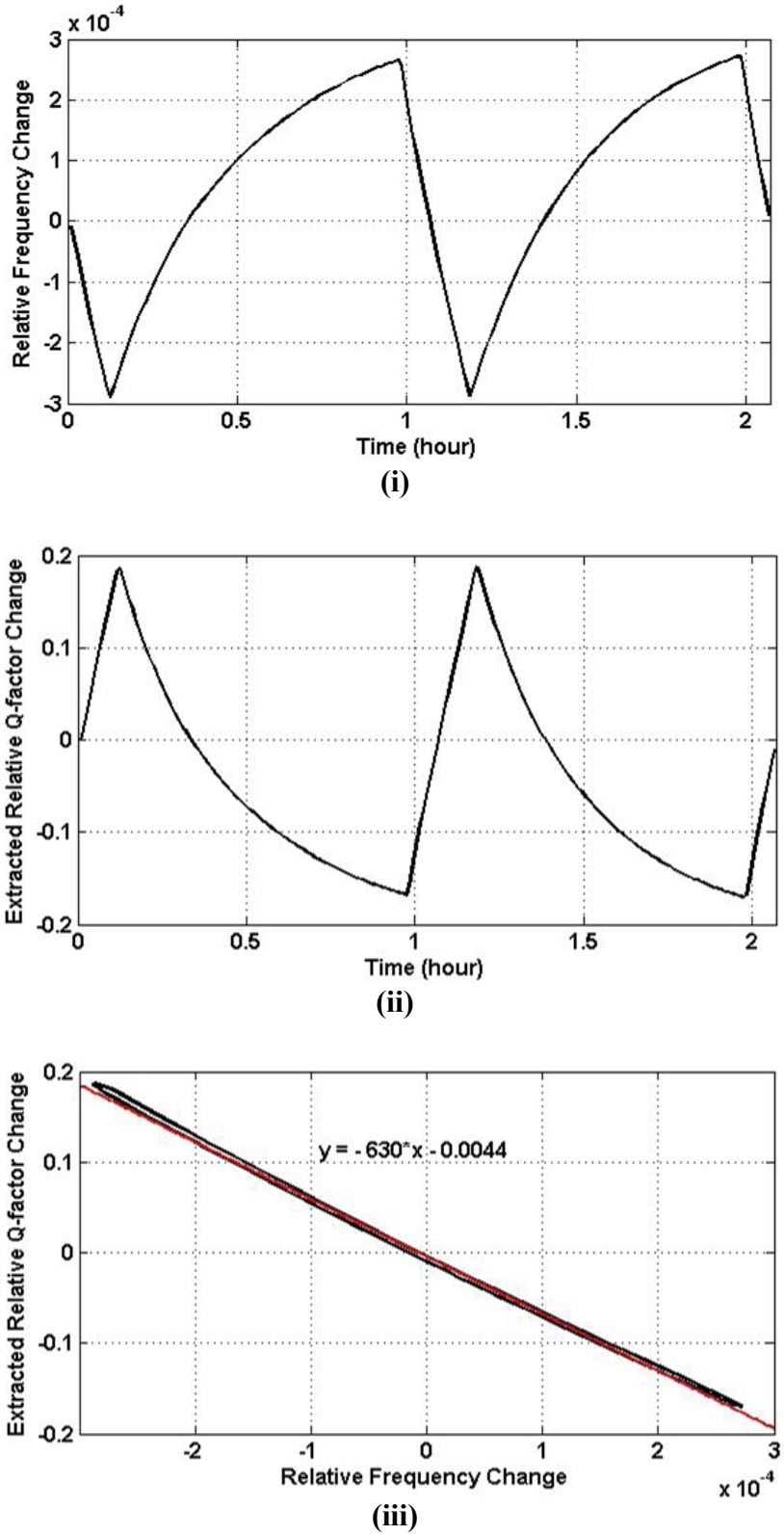

Figure 6.6: (i) Relative frequency change and (ii) extracted relative Q-factor change obtained during the calibration measurement, and (iii) extracted Q-factor change as a function of the relative frequency change.

Using the data from Figures 6.6 (i) and (ii), the calibration curve is extracted (Figure 6.6 (iii)). As can be seen in Figure 6.6 (iii), there is an almost linear relationship between the relative Q-factor and frequency changes. In this case, a linear regression yields $dQ/Q = -630\, d\omega_0/\omega_0$; this relationship is used to compensate for the frequency drift of the employed resonator during the chemical measurements.

After the calibration step, gas-phase chemical measurements are performed. An example measurement is shown in Figure 6.7, displaying the resonance frequency change with (blue line) and without (red line) compensation versus time.

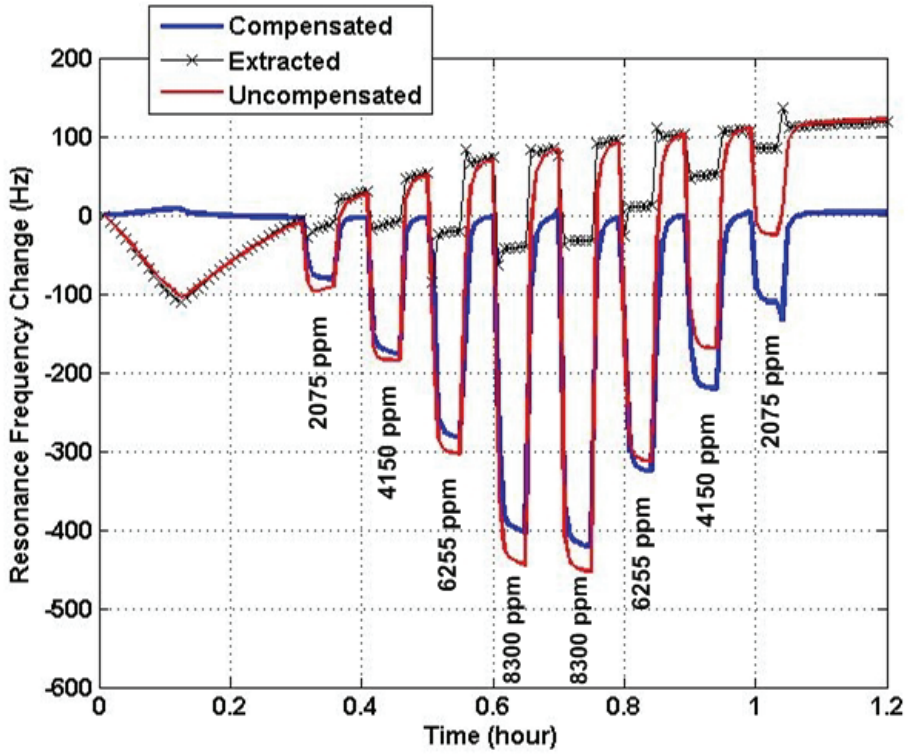

Figure 6.7: Closed-loop oscillation frequency change with (blue line) and without (red line) compensation while exposing the microresonator to different toluene concentrations and slowly changing the measurement chamber temperature with a thermoelectric cooler. The dotted black line shows the extracted frequency change obtained using the extracted Q-factor.

For this measurement, the total gas flow was set to 80 ml/min. Reference gas (nitrogen) and analyte gas (toluene) are alternately applied to the measurement chamber in 5 minute intervals and the analyte concentration is changed after every analyte injection. Again, the temperature of the measurement chamber is slowly varied by using a thermoelectric cooler to simulate a temperature drift, which results in a 200 Hz frequency drift.

The Q-factor is extracted using Eq. (6.8) and shown in Figure 6.8. The extracted Q-factor of 1070 at the beginning of the measurement corresponds to the value at room temperature and is in close proximity to the Q-factor of 1160 obtained with an open-loop transfer function measurement using a network analyzer. It should be noted that this Q-factor is for a polymer-coated resonator. Using this extracted Q-factor, the frequency change stemming from the Q-factor change is estimated using the relation $dQ/Q = -630\, d\omega_0/\omega_0$ obtained with the initial calibration step. This estimated frequency change is shown as the dotted black line in Figure 6.7 and is used to compensate for the frequency drift. The final compensated frequency signal (blue line in Figure 6.7) is simply the difference between the measured (red line) and estimated frequency (dotted black line). After compensation, the frequency is stable to within ±10Hz over the 1.2 hour measurement time, and the frequency decreases during analyte exposure are clearly visible.

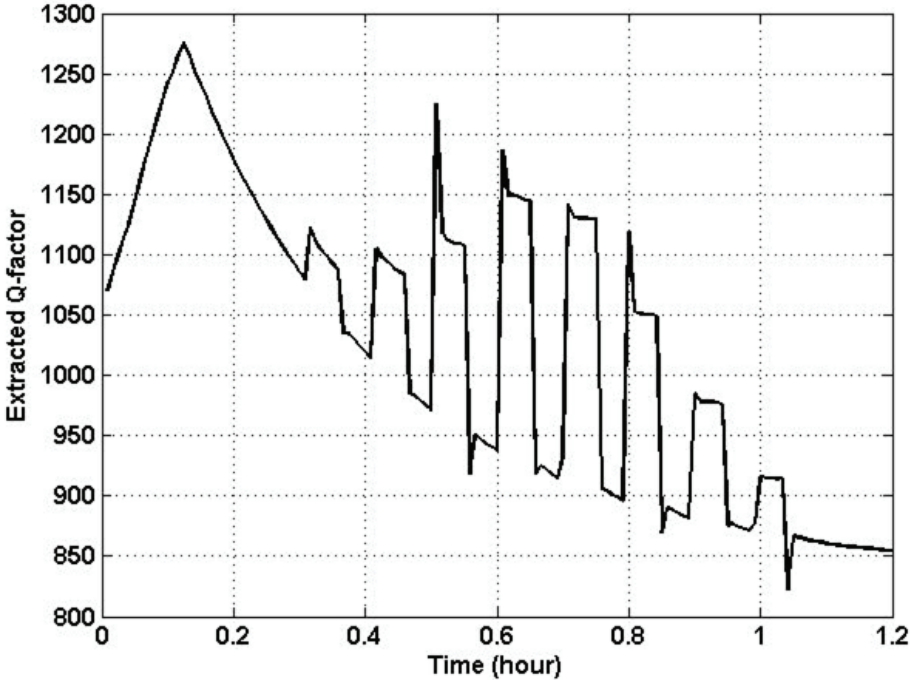

Figure 6.8: Extracted Q-factor from Eq. (6.8) during the gas-phase chemical measurement shown in Figure 6.7.

CHAPTER 7

CONCLUSION

Hand-held chemical sensing instruments have broadened the chemical detection market by enabling new application areas. In particular, these devices allow for the continuous on-site monitoring of a wide range of chemical analytes, which cannot be done with bench-top analytical instruments. In realizing such hand-held instruments, CMOS-integrated interface electronics can play a crucial role. When compared to off-chip electronics, CMOS interface circuits enable the integration of the entire sensing system in a compact package with reduced power consumption and system cost. Therefore, in this work, a CMOS ASIC has been developed and integrated with silicon-based resonant microsensors to implement a chemical microsystem, which can be incorporated in a hand-held platform.

The development of a microsystem requires the assessment of not only the characteristics and operation principles of the sensor but also of the appropriate CMOS interface circuit architectures for signal conditioning. Therefore, various circuitry techniques to monitor frequency output signals from resonant sensors have been investigated. Also, the resonant microstructures (cantilever and disk-shape microresonators with thermal excitation and piezoresistive detection elements) previously developed in our research group have been carefully examined to understand their characteristics pertinent to the circuit and system design. Accordingly, CMOS-integrated interface and control electronics have been designed and implemented. The circuit blocks have been designed to obtain low noise and adequate bandwidth with low power consumption, which is especially important for portable devices.

The CMOS ASIC utilizes the self-oscillation method, which incorporates the microresonator in an amplifying feedback loop as the frequency determining element. In

this manner, the ASIC includes a main feedback (MF) loop to start and sustain oscillation at or close to the fundamental resonance frequency of the microresonator. For stable oscillation, an automatic gain control (AGC) loop, which regulates the oscillation amplitude by controlling the gain of the MF loop, has been implemented. In addition, an automatic phase control (APC) loop has been included to adjust the phase of the main feedback loop, thus ensuring an operating point as close as possible to the resonance frequency, which results in improved frequency stability. Currently, the analog output of the APC loop is interfaced to a PC via a DAQ card with long cables, resulting in increased noise, which limits the APC performance. By implementing an ADC on the CMOS chip, the APC output can be directly converted into digital signals, which are less effected by noise. As a result, the APC can be used more effectively. The CMOS chip has been interfaced to cantilever and disk-shape microresonators and short-term frequency stabilities as low as 3.4×10^{-8} in air have been obtained with a 1 sec gate time.

The CMOS ASIC consumes a current of 5 mA, resulting in a power consumption of 16.5 mW. Together with the off-chip electronics necessary to control the ASIC, the power consumption of the implemented system increases to 117.6 mW, mainly because of the increase in the power supply voltages from ±1.65 V to ±6 V. The power consumption can be further reduced significantly if the system is interfaced with a microcontroller instead of a PC.

The performance of the implemented microsystem as a chemical sensor has been evaluated experimentally using microresonators coated with a chemically-sensitive polymer film. A gas-phase chemical measurement setup has been constructed for these experiments. The measurement setup features two different gas mixing methods to provide analytes at desired concentrations. With this setup, gas-phase chemical measurements have been performed and different concentrations of benzene, toluene, and m-xylene have been detected. As an example, the sensitivity of the sensor system for toluene is found to be approximately 70.7 mHz/ppm. With a short-term frequency

stability of 28.5 mHz extracted with the Allan variance method, the LOD of the sensor system is estimated as 1.2 ppm for toluene in the gas phase.

To improve the long-term stability of the resonant microsystem, a method to compensate for frequency drift caused by environmental disturbances and aging of the microresonator has been proposed and implemented on the CMOS chip. This method uses a controlled stiffness modulation generated by the frequency drift compensation circuit to track the changes in the resonator's Q-factor in response to variations in the environmental conditions. The measured Q-factor is then used to compensate for the frequency drift caused by e.g. temperature variations using an initial calibration step. By compensating for frequency drift, the resonator's response to mass changes can be measured more precisely. The implemented compensation method has three particular advantages. First, the method only requires frequency measurements and does not need additional sensing devices to track the Q-factor. Second, the Q-factor is monitored along with the measurand-induced frequency shift during normal closed-loop sensor operation of the resonator. Finally, the method only requires an additional feedback circuit; therefore, this method is applicable to all resonant microstructures featuring excitation and detection elements without structural modifications. The feasibility of the proposed method has been verified experimentally by compensating for temperature-induced frequency drift during gas-phase chemical measurements. However, the possibility of compensating for other environmental factors, e.g. humidity, with the developed compensation method has not been investigated yet.

APPENDIX A

PCB CONTROLLING ASIC_v2

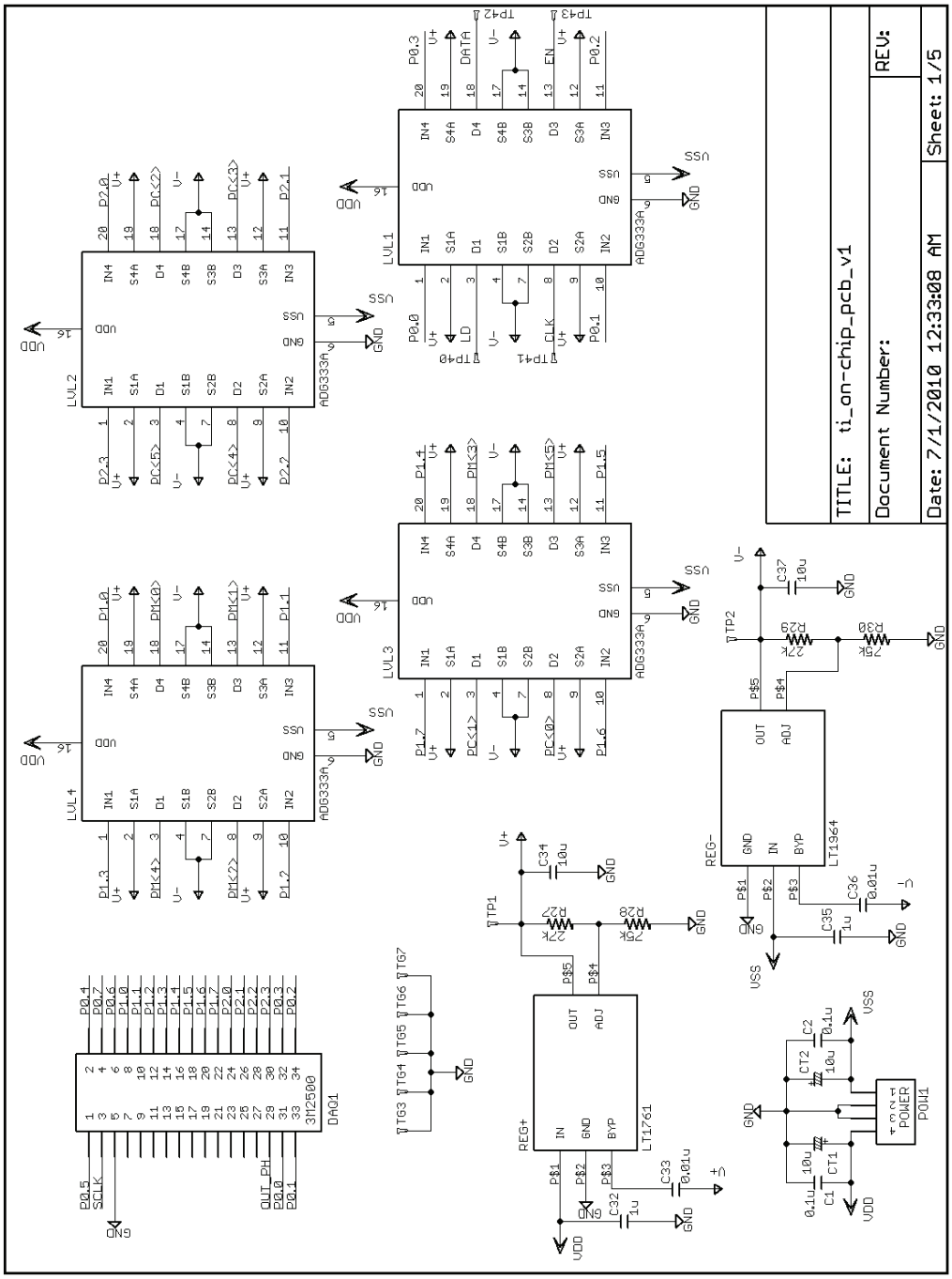

Figure A.1: Voltage regulators, level translators, and power and DAQ connectors, as implemented on the PCB controlling ASIC_v2.

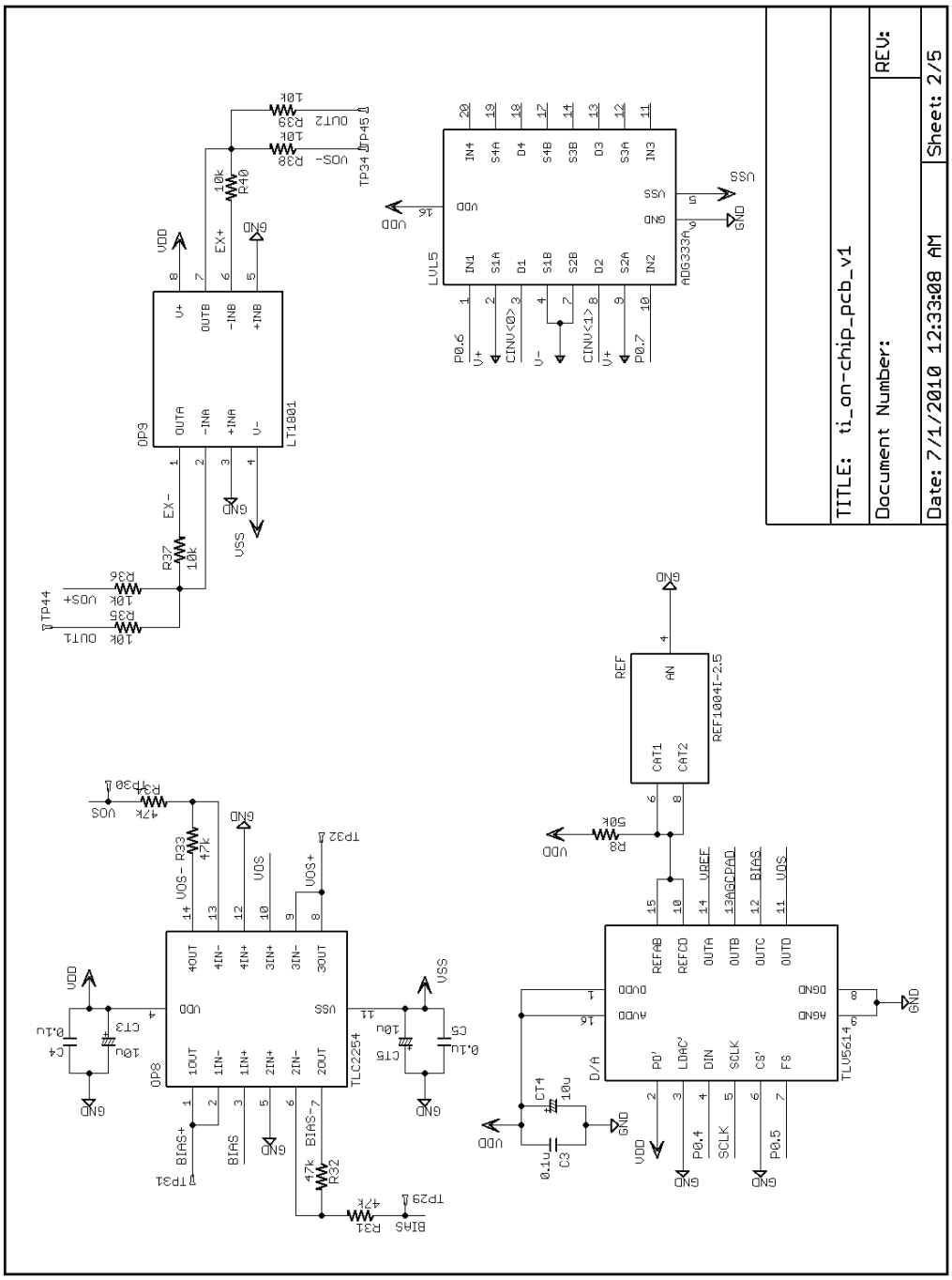

Figure A.2: DAC and sensor bias generator circuits, as implemented on the PCB controlling ASIC_v2.

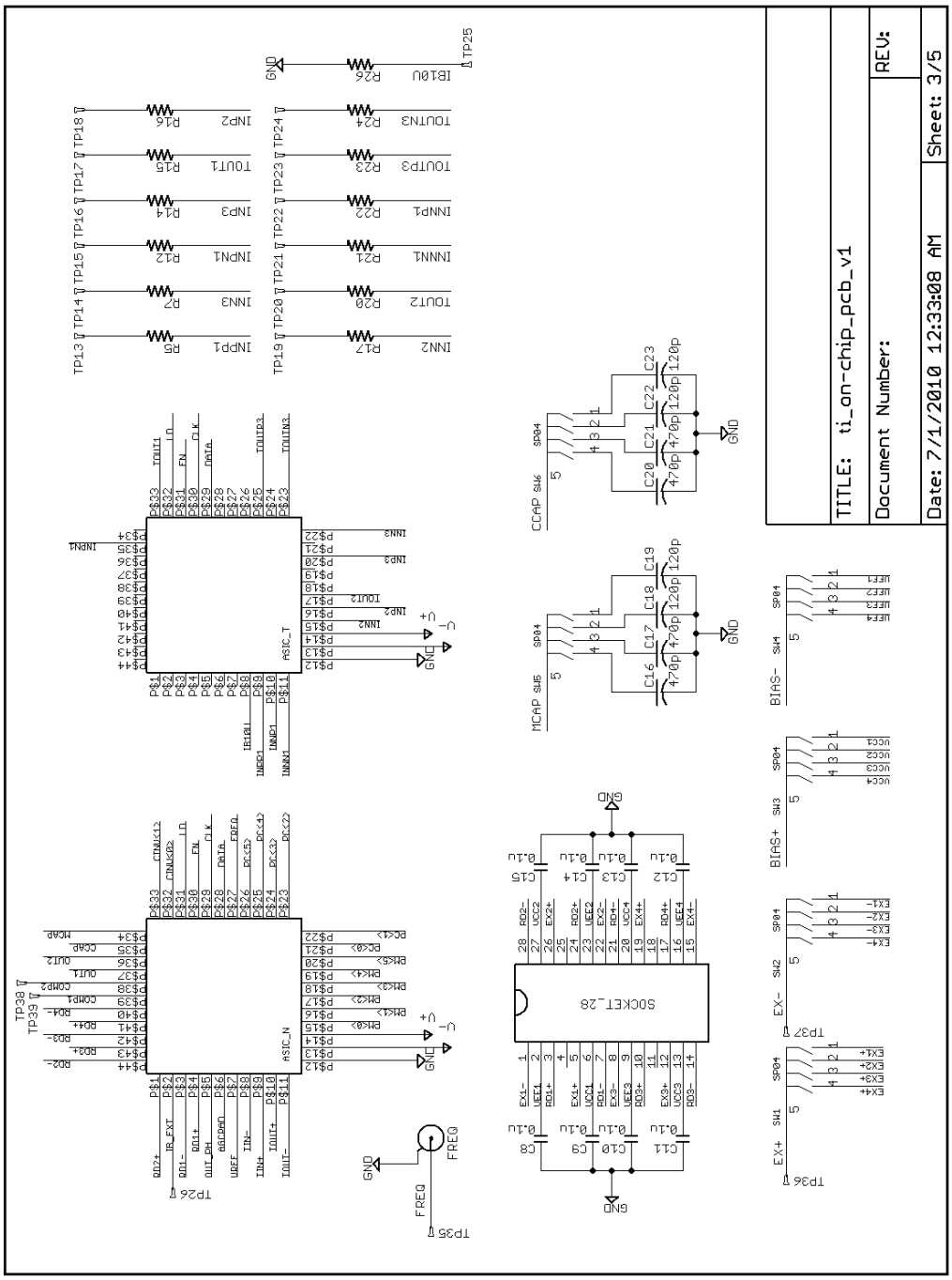

Figure A.3: Capacitor bank, chip connectors and manual switches, as implemented on the PCB controlling ASIC_v2.

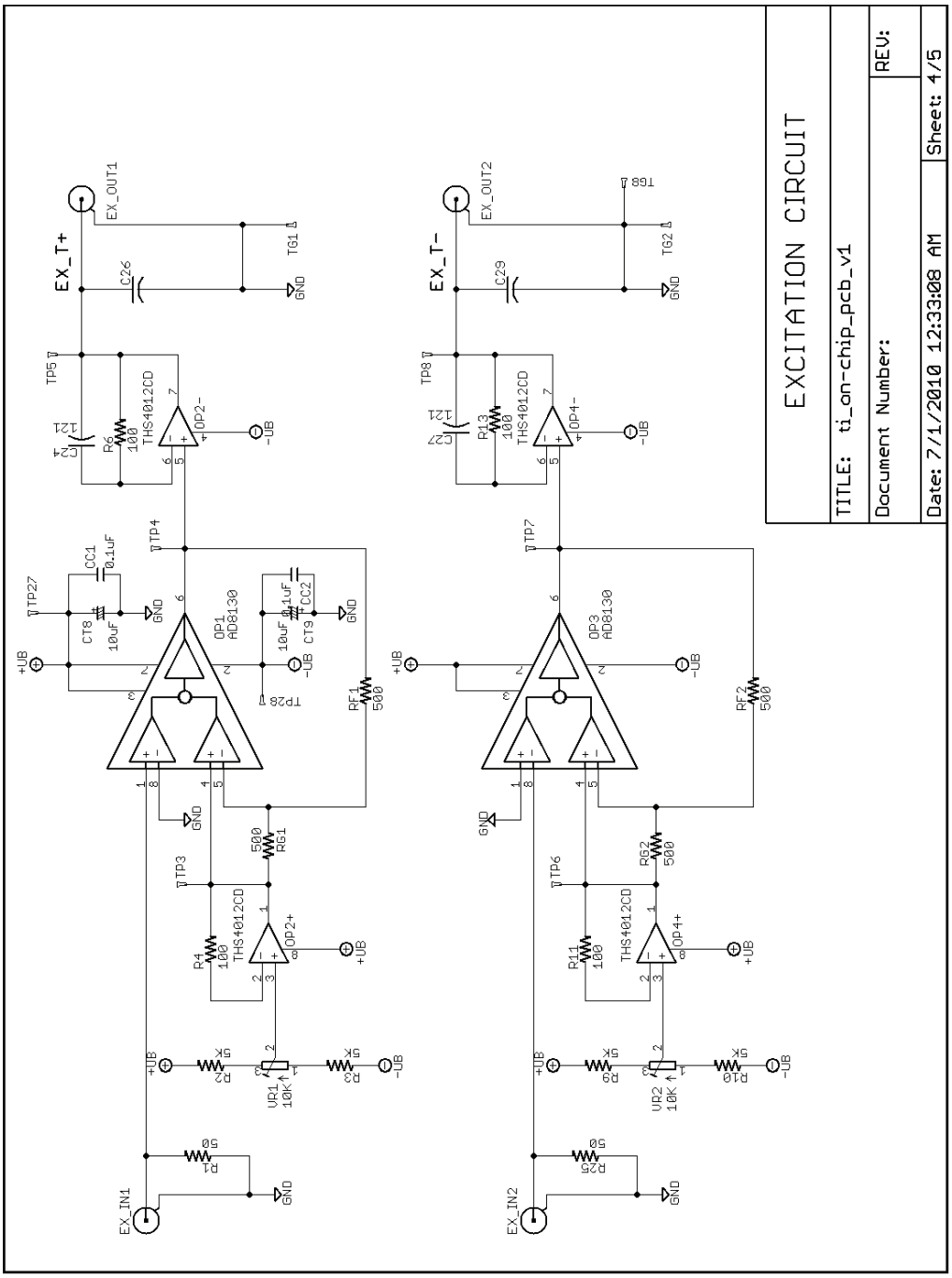

Figure A.4: Excitation circuits for tests, as implemented on the PCB controlling ASIC_v2.

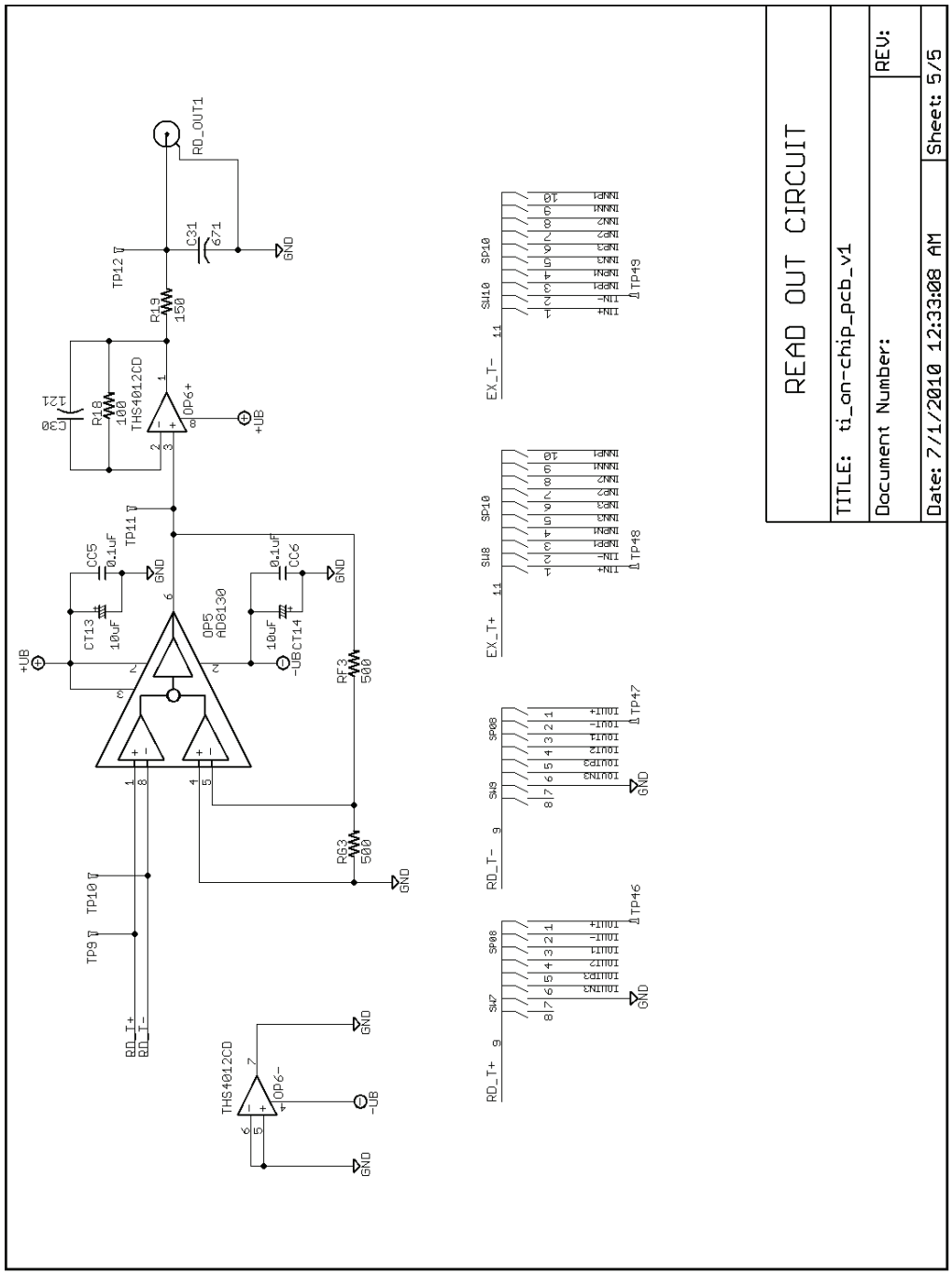

Figure A.5: Readout circuits for tests, as implemented on the PCB controlling ASIC_v2.

APPENDIX B

PCB CONTROLLING CHEMICAL MEASUREMENT SETUP

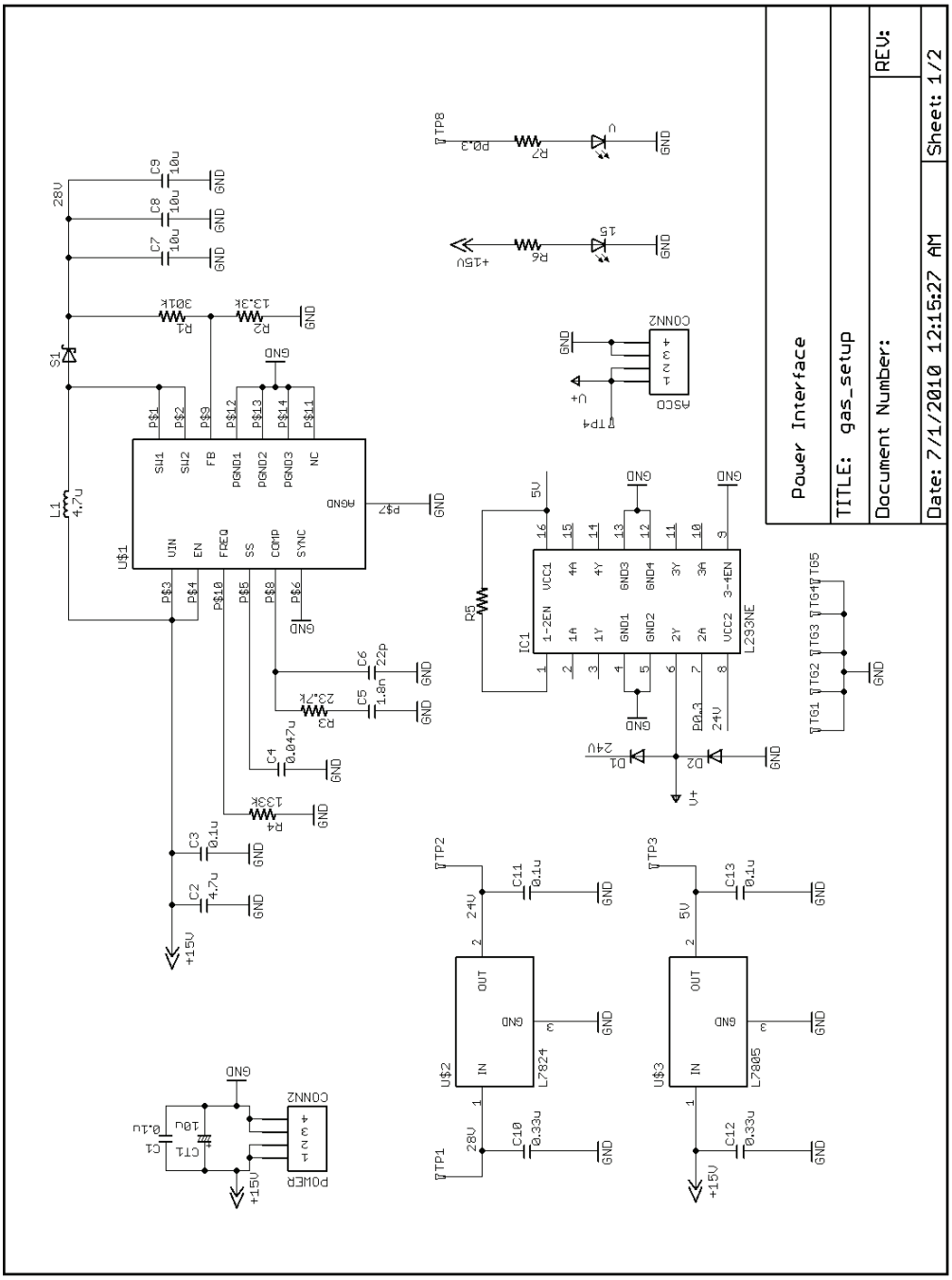

Figure B.1: Voltage regulators, DC-DC converter circuit, and power connector, as implemented on the PCB controlling the gas-phase chemical measurement setup.

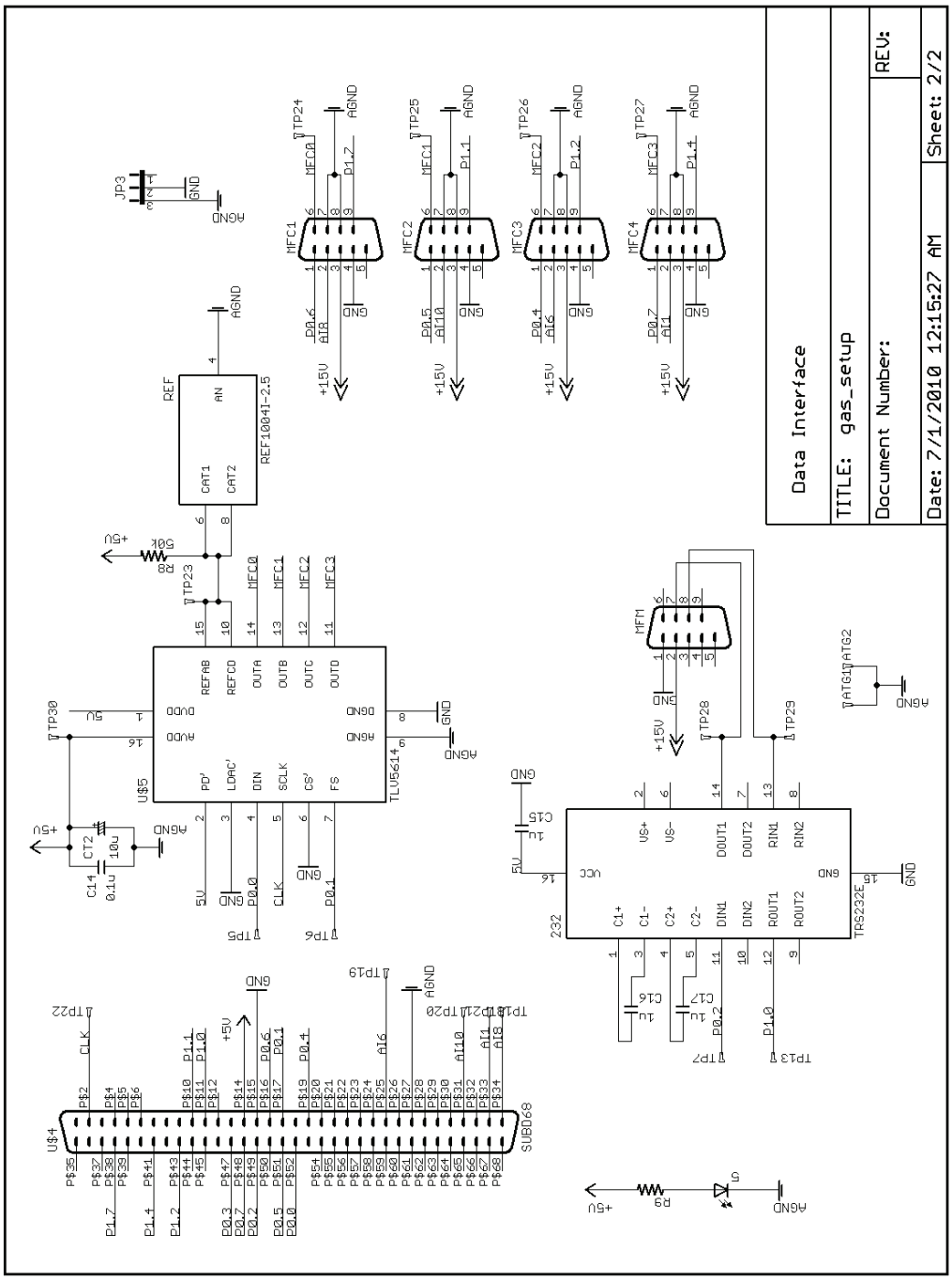

Figure B.2: DAC and RS-232 interface circuits, and DAQ and MFC connectors, as implemented on the PCB controlling the gas-phase chemical measurement setup.

APPENDIX C

SATURATION VAPOR PRESSURES

The temperature-dependent saturation vapor pressure $p_a(T)$ of the analyte in units of mmHg is given by the Antoine equation [110]

$$\log p_a(T) = A - \frac{B}{C+T}, \tag{C.1}$$

where T is the temperature, and A, B, and C are analyte specific constants, which can be found in [110]. Using the conversion factor of 133.2 to convert mmHg into Pa, Eq. (C.1) can be expressed in units of Pa by

$$p_a(T) = 133.2 \times 10^{\left(A - \frac{B}{C+T}\right)}. \tag{C.2}$$

The saturation vapor pressure $p_a(T)$ of the analyte is then converted into the initial analyte concentration $c_b(T)$ in units of ppm with the relation [111]:

$$c_b(T) = 10\, p_a(T). \tag{C.3}$$

The saturation vapor pressures and initial concentrations of the analytes of interest at different temperatures are listed in Table C.1.

Table C.1: Saturation vapor pressures and initial concentrations of analytes of interest at different temperatures.

	Benzene		Toluene		m-Xylene	
Temp. (°C)	**Sat. Vapor Pres. (Pa)**	**Initial Conc. (ppm)**	**Sat. Vapor Pres. (Pa)**	**Initial Conc. (ppm)**	**Sat. Vapor Pres. (Pa)**	**Initial Conc. (ppm)**
-20	1039.91	10399.1	219.15	2191.5	43.93	439.3
-18	1191.76	11917.6	255.58	2555.8	52.31	523.1
-16	1362.15	13621.5	297.17	2971.7	62.08	620.8
-14	1552.89	15528.9	344.52	3445.2	73.43	734.3
-12	1765.90	17659.0	398.28	3982.8	86.57	865.7
-10	2003.23	20032.3	459.15	4591.5	101.72	1017.2
-8	2267.09	22670.9	527.91	5279.1	119.16	1191.6
-6	2559.80	25598.0	605.39	6053.9	139.17	1391.7
-4	2883.83	28838.3	692.47	6924.7	162.06	1620.6
-2	3241.82	32418.2	790.14	7901.4	188.19	1881.9
0	3636.53	36365.3	899.42	8994.2	217.91	2179.1
2	4070.90	40709.0	1021.42	10214.2	251.65	2516.5
4	4548.01	45480.1	1157.35	11573.5	289.86	2898.6
6	5071.13	50711.3	1308.46	13084.6	333.01	3330.1
8	5643.67	56436.7	1476.12	14761.2	381.64	3816.4
10	6269.22	62692.2	1661.78	16617.8	436.31	4363.1
12	6951.55	69515.5	1866.97	18669.7	497.64	4976.4
14	7694.60	76946.0	2093.33	20933.3	566.30	5663.0
16	8502.47	85024.7	2342.58	23425.8	642.99	6429.9
18	9379.48	93794.8	2616.56	26165.6	728.48	7284.8
20	10330.09	103300.9	2917.20	29172.0	823.58	8235.8
22	11358.98	113589.8	3246.54	32465.4	929.18	9291.8
24	12470.99	124709.9	3606.73	36067.3	1046.22	10462.2
26	13671.17	136711.7	4000.03	40000.3	1175.67	11756.7
28	14964.73	149647.3	4428.82	44288.2	1318.62	13186.2
30	16357.10	163571.0	4895.59	48955.9	1476.19	14761.9
32	17853.88	178538.8	5402.95	54029.5	1649.58	16495.8
34	19460.87	194608.7	5953.65	59536.5	1840.05	18400.5
36	21184.06	211840.6	6550.53	65505.3	2048.95	20489.5
38	23029.62	230296.2	7196.58	71965.8	2277.69	22776.9
40	25003.92	250039.2	7894.91	78949.1	2527.79	25277.9

REFERENCES

[1] A. Hierlemann, O. Brand, C. Hagleitner, and H. Baltes, "Microfabrication techniques for chemical/biosensors," *Proceedings of the IEEE,* vol. 91, pp. 839-863, 2003.

[2] D. Diamond, *Principles of chemical and biological sensors*. New York: Wiley, 1994.

[3] S. Alegret, "Integrated analytical systems," in *Comprehensive analytical chemistry*, D. Barcelo, Ed. Amsterdam: Elsevier Science, 2003.

[4] J. Janata, M. Josowicz, P. Vanysek, and D. M. DeVaney, "Chemical sensors," *Analytical Chemistry,* vol. 70, pp. 179r-208r, 1998.

[5] R. C. Hughes, A. J. Ricco, M. A. Butler, and S. J. Martin, "Chemical Microsensors," *Science,* vol. 254, pp. 74-80, 1991.

[6] P. A. Lieberzeit and F. L. Dickert, "Chemosensors in environmental monitoring: challenges in ruggedness and selectivity," *Analytical and Bioanalytical Chemistry,* vol. 393, pp. 467-472, 2009.

[7] R. F. Taylor, "Chemical and biological sensors: markets and commercialization," in *Handbook of chemical and biological sensors*, R. F. Taylor, Schultz, J. S., Ed. Bristol: IOP Publishing Ltd, 1996.

[8] J. Saffell, "Gas detection: market needs driving innovation," *J. Phys., Conf. Ser. (UK)*, UK, 2009, p. 012002 (3 pp.).

[9] C. K. Ho, A. Robinson, D. R. Miller, and M. J. Davis, "Sensors for environmental monitoring and long-term environmental stewardship," Sandia National Laboratories, Albuquerque, Report SAND2004-4596, 2004.

[10] www.epa.gov/air/airpollutants.html.

[11] www.epa.gov/safewater/contaminants/index.html.

[12] M. Arndt and M. Sauer, "Infrared carbon dioxide sensor and its applications in automotive air-conditioning systems," in *Advanced microsystems for automotive applications*, J. Valldorf and W. Gessner, Eds. New York: Springer, 2005.

[13] C. L. Whittle, S. Fakharzadeh, J. Eades, and G. Preti, "Human Breath Odors and Their Use in Diagnosis," *Annals of the New York Academy of Sciences,* vol. 1098, pp. 252-266, 2007.

[14] C. E. Davis, M. J. Bogan, S. Sankaran, M. A. Molina, B. R. Loyola, Z. Weixiang, W. H. Benner, M. Schivo, G. R. Farquar, N. J. Kenyon, and M. Frank, "Analysis of volatile and non-volatile biomarkers in human breath using differential mobility spectrometry (DMS)," *IEEE Sensors Journal,* vol. 10, pp. 114-22, 2010.

[15] www.figarosensor.com.

[16] J. J. Lavigne and E. V. Anslyn, "Sensing a paradigm shift in the field of molecular recognition: From selective to differential receptors," *Angewandte Chemie-International Edition,* vol. 40, pp. 3119-3130, 2001.

[17] "C16 PortaSens II," Analytical technology, Inc., Collegeville, PA, USA (analyticaltechnology.com).

[18] "GasAlertMicro 5 PID," BW Technologies, Arlington, TX, USA (www.gasmonitors.com).

[19] "X-am 7000," Draeger Safety Inc., Pittsburgh, PA, USA (www.draeger.com).

[20] "Recon/4," Enmet Corp., Ann Arbor, MI, USA (www.enmet.com).

[21] "M40," Industrial Scientific, Oakdale, PA, USA (www.indsci.com).

[22] "IQ-250," International Sensor Technology, Irvine, CA, USA (www.intlsensor.com).

[23] "Sirius," MSA, Pittsburgh, PA, USA (www.msanorthamerica.com).

[24] "HAZMATCAD Plus," MSA, Pittsburgh, PA, USA (www.msanorthamerica.com).

[25] "MultiLog 2000," Quest Technologies, Inc., Oconomowoc, WI, USA (questtechnologies.com).

[26] "VRAE," RAE Systems, San Jose, CA, USA (www.raesystems.com).

[27] "Scout," Scott Health & Safety, Monroe, NC, USA (www.scotthealthsafety.com).

[28] "Genesis," Thermo Fisher Scientific, USA (www.thermoscientific.com).

[29] "Sensit Gold CGI," J and N Enterprises, Inc., Valparaiso, IN, USA (www.gasleaksensors.com).

[30] "Biosystems MultiVision," Sperian Protection, Smithfield, RI, USA (www.sperian.com).

[31] "MiniMax X4," Honeywell Analytics, Inc., Lincolnshire, IL, USA (www.honeywellanalytics.com).

[32] Q. Zhong, W. H. Steinecker, and E. T. Zellers, "Characterization of a high-performance portable GC with a chemiresistor array detector," *Analyst,* vol. 134, pp. 283-293, 2009.

[33] G. T. Dobbs, B. Balu, C. Young, C. Kranz, D. W. Hess, and B. Mizaikoff, "Mid-infrared chemical sensors utilizing plasma-deposited fluorocarbon membranes," *Analytical Chemistry,* vol. 79, pp. 9566-9571, 2007.

[34] L. A. Beardslee, S. M. Heinrich, F. Josse, and O. Brand, "Thermal Excitation and Piezoresistive Detection of Cantilever In-Plane Resonance Modes for Sensing Applications," *Journal of Microelectromechanical Systems,* 2010, in print.

[35] J. H. Seo and O. Brand, "High Q-factor in-plane-mode resonant microsensor platform for gaseous/liquid environment," *Journal of Microelectromechanical Systems,* vol. 17, pp. 483-493, 2008.

[36] C. K. Ho, M. T. Itamura, M. Kelley, and R. C. Hughes, "Review of chemical sensors for in-situ monitoring of volatile contaminants," Sandia National Laboratories, Albuquerque, Report SAND2001-0643, 2001.

[37] "Volatile organic compounds in the environment," in *STP*, W.-C. Wang, J. L. Schnoor, and J. Doi, Eds. West Conshohocken, Pa.: ASTM, 1996.

[38] EPA, "National Air Pollutant Emission Trends Update 1970-2008," U.S. EPA, 2009.

[39] E. R. Benes, R. Groschl, F. Seifert, and A. Pohl, "Comparison between BAW and SAW sensor principles," *IEEE Transactions on Ultrasonics Ferroelectrics and Frequency Control,* vol. 45, pp. 1314-1330, 1998.

[40] H. A. C. Tilmans, M. Elwenspoek, and J. H. J. Fluitman, "Micro resonant force gauges," *Sensors and Actuators A-Physical,* vol. 30, pp. 35-53, 1992.

[41] T. C. Pearce, S. S. Schiffman, H. T. Nagle, and J. W. Gardner, *Handbook of machine olfaction*. Weinhem: Wiley-VCH, 2003.

[42] B. Drafts, "Acoustic wave technology sensors," *IEEE Transactions on Microwave Theory and Techniques,* vol. 49, pp. 795-802, 2001.

[43] D. James, S. M. Scott, Z. Ali, and W. T. O'Hare, "Chemical sensors for electronic nose systems," *Microchimica Acta,* vol. 149, pp. 1-17, 2005.

[44] A. Arnau, "Piezoelectric transducers and applications," 2nd ed Verlag Berlin Heidelberg: Springer, 2008.

[45] L. Rodriguez-Pardo, J. F. Rodriguez, C. Gabrielli, and R. Brendel, "Sensitivity, noise, and resolution in QCM sensors in liquid media," *IEEE Sensors Journal,* vol. 5, pp. 1251-1257, 2005.

[46] L. M. Dorozhkin and I. A. Rozanov, "Acoustic wave chemical sensors for gases," *Journal of Analytical Chemistry,* vol. 56, pp. 399-416, 2001.

[47] M. Hoummady, A. Campitelli, and W. Wlodarski, "Acoustic wave sensors: design, sensing mechanisms and applications," *Smart Materials & Structures,* vol. 6, pp. 647-657, 1997.

[48] E. Schaller, J. O. Bosset, and F. Escher, "'Electronic noses' and their application to food," *Food Science and Technology-Lebensmittel-Wissenschaft & Technologie,* vol. 31, pp. 305-316, 1998.

[49] Z. H. Ying, Y. D. Jiang, X. S. Du, G. Z. Xie, J. S. Yu, and H. L. Tai, "Polymer coated sensor array based on quartz crystal microbalance for chemical agent analysis," *European Polymer Journal,* vol. 44, pp. 1157-1164, 2008.

[50] P. A. Lieberzeit, A. Rehman, B. Najafi, and F. L. Dickert, "Real-life application of a QCM-based e-nose: quantitative characterization different plant-degradation processes," *Analytical and Bioanalytical Chemistry,* vol. 391, pp. 2897-2903, 2008.

[51] X. X. Jin, Y. Huang, A. Mason, and X. Q. Zeng, "Multichannel monolithic quartz crystal microbalance gas sensor array," *Analytical Chemistry,* vol. 81, pp. 595-603, 2009.

[52] J. Rabe, S. Buttgenbach, J. Schroder, and P. Hauptmann, "Monolithic miniaturized quartz microbalance array and its application to chemical sensor systems for liquids," *IEEE Sensors Journal,* vol. 3, pp. 361-368, 2003.

[53] B. S. Joo, J. S. Huh, and D. D. Lee, "Fabrication of polymer SAW sensor array to classify chemical warfare agents," *Sensors and Actuators B-Chemical,* vol. 121, pp. 47-53, 2007.

[54] H. B. Lin and J. S. Shih, "Fullerene C60-cryptand coated surface acoustic wave quartz crystal sensor for organic vapors," *Sensors and Actuators B-Chemical,* vol. 92, pp. 243-254, 2003.

[55] Z. H. Li, Y. Jones, J. Hossenlopp, R. Cernosek, and F. Josse, "Analysis of liquid-phase chemical detection using guided shear horizontal-surface acoustic wave sensors," *Analytical Chemistry,* vol. 77, pp. 4595-4603, 2005.

[56] N. V. Lavrik, M. J. Sepaniak, and P. G. Datskos, "Cantilever transducers as a platform for chemical and biological sensors," *Review of Scientific Instruments,* vol. 75, pp. 2229-2253, 2004.

[57] P. S. Waggoner and H. G. Craighead, "Micro- and nanomechanical sensors for environmental, chemical, and biological detection," *Lab on a Chip,* vol. 7, pp. 1238-1255, 2007.

[58] C. Vancura, M. Ruegg, Y. Li, C. Hagleitner, and A. Hierlemann, "Magnetically actuated complementary metal oxide semiconductor resonant cantilever gas sensor systems," *Analytical Chemistry,* vol. 77, pp. 2690-2699, 2005.

[59] D. Lange, C. Hagleitner, A. Hierlemann, O. Brand, and H. Baltes, "Complementary metal oxide semiconductor cantilever arrays on a single chip: Mass-sensitive detection of volatile organic compounds," *Analytical Chemistry,* vol. 74, pp. 3084-3095, 2002.

[60] D. Then, A. Vidic, and C. Ziegler, "A highly sensitive self-oscillating cantilever array for the quantitative and qualitative analysis of organic vapor mixtures," *Sensors and Actuators B-Chemical,* vol. 117, pp. 1-9, 2006.

[61] I. Voiculescu, M. E. Zaghloul, R. A. McGill, E. J. Houser, and G. K. Fedder, "Electrostatically actuated resonant microcantilever beam in CMOS technology for the detection of chemical weapons," *IEEE Sensors Journal,* vol. 5, pp. 641-647, 2005.

[62] C. Vancura, Y. Li, J. Lichtenberg, K. U. Kirstein, A. Hierlemann, and F. Josse, "Liquid-phase chemical and biochemical detection using fully integrated magnetically actuated complementary metal oxide semiconductor resonant cantilever sensor systems," *Analytical Chemistry,* vol. 79, pp. 1646-1654, 2007.

[63] J. H. Seo, "Silicon-based resonant microsensor platform for chemical and biological applications," PhD thesis, Georgia Institute of Technology, 2007.

[64] T. R. Albrecht, P. Grutter, D. Horne, and D. Rugar, "Frequency-modulation detection using high-Q cantilevers for enhanced force microscope sensitivity," *Journal of Applied Physics,* vol. 69, pp. 668-673, 1991.

[65] R. G. Kryshtal and A. V. Medved, "Sensors based on SAW resonator with "nontraditional formats" of output signal," *Journal of Electroceramics,* vol. 17, pp. 987-993, 2006.

[66] A. N. Cleland and M. L. Roukes, "A nanometre-scale mechanical electrometer," *Nature,* vol. 392, pp. 160-162, 1998.

[67] W. Y. Chang, P. H. Sung, C. H. Chu, C. J. Shih, and Y. C. Lin, "Phase detection of the two-port FPW sensor for biosensing," *IEEE Sensors Journal,* vol. 8, pp. 501-507, 2008.

[68] D. Jeutter, F. Josse, M. Johnson, M. Wenzel, J. Hossenlopp, and R. Cernosek, "Design of a portable guided SH-SAW chemical sensor system for liquid environments," *2005 IEEE International Frequency Control Symposium and Exhibition*, Vancouver, BC, Canada, 2005, pp. 59-68.

[69] J. D. Sternhagen, K. Mitzner, E. Berkenpas, M. Karlgaard, C. E. Wold, and D. W. Galipeau, "A direct digital synthesis system for acoustic wave sensors," *IEEE Sensors Journal,* vol. 2, pp. 288-93, 2002.

[70] T. Okajima, H. Sekiguchi, H. Arakawa, and A. Ikai, "Self-oscillation technique for AFM in liquids," *Applied Surface Science,* vol. 210, pp. 68-72, 2003.

[71] A. T. Nimal, U. Mittal, M. Singh, M. Khaneja, G. K. Kannan, J. C. Kapoor, V. Dubey, P. K. Gutch, G. Lal, K. D. Vyas, and D. C. Gupta, "Development of handheld SAW vapor sensors for explosives and CW agents," *Sensors and Actuators B-Chemical,* vol. 135, pp. 399-410, 2009.

[72] U. Durig, O. Zuger, and A. Stalder, "Interaction force detection in scanning probe microscopy - methods and applications," *Journal of Applied Physics,* vol. 72, pp. 1778-1798, 1992.

[73] K. L. Ekinci, Y. T. Yang, and M. L. Roukes, "Ultimate limits to inertial mass sensing based upon nanoelectromechanical systems," *Journal of Applied Physics,* vol. 95, pp. 2682-2689, 2004.

[74] N. M. Nguyen and R. G. Meyer, "Start-up and frequency stability in high-frequency oscillators," *IEEE Journal of Solid-State Circuits,* vol. 27, pp. 810-820, 1992.

[75] J. Janata, "Centennial retrospective on chemical sensors," *Analytical Chemistry,* vol. 73, pp. 150a-153a, 2001.

[76] T. H. Lee and A. Hajimiri, "Oscillator phase noise: A tutorial," *IEEE Journal of Solid-State Circuits,* vol. 35, pp. 326-336, 2000.

[77] T. E. Parker, "Characteristics and sources of phase noise in stable oscillators," *41st Annual Frequency Symposium*, Philadelphia, PA, USA, 1987, pp. 99-110.

[78] L. Fadel, I. Dufour, F. Lochon, and O. Francais, "Signal-to-noise ratio of resonant microcantilever type chemical sensors as a function of resonant frequency and quality factor," *Sensors and Actuators B-Chemical,* vol. 102, pp. 73-77, 2004.

[79] J. H. Ginsberg, *Mechanical and structural vibrations: theory and applications*. New York: John Wiley & Sons, Inc., 2001.

[80] D. B. Leeson, "A simple model of feedback oscillator noise spectrum," *Proceedings of the Institute of Electrical and Electronics Engineers,* vol. 54, pp. 329-330, 1966.

[81] D. Allan, H. Hellwig, P. Kartaschoff, J. Vanier, J. Vig, G. M. R. Winkler, and N. F. Yannoni, "Standard terminology for fundamental frequency and time metrology," *Proceedings of the 42nd Annual Frequency Control Symposium 1988*, New York, NY, USA, 1988, pp. 419-25.

[82] D. W. Allan and J. A. Barnes, "A Modified "Allan Variance" with Increased Oscillator Characterization Ability," *Thirty Fifth Annual Frequency Control Symposium. 1981*, 1981, pp. 470-475.

[83] J. Bryzek, A. Flannery, and D. Skurnik, "Integrating microelectromechanical systems with integrated circuits," *IEEE Instrumentation & Measurement Magazine,* vol. 7, pp. 51-59, 2004.

[84] C. Kitchin and L. Counts, *A designer's guide to instrumentation amplifiers*: Analog Devices, Inc., 2004.

[85] K. S. Demirci, S. Truax, L. A. Beardslee, and O. Brand, "Chemical microsystem based on integration of microresonant sensor and CMOS ASIC," *2009 IEEE Custom Integrated Circuits Conference (CICC)*, San Jose, CA, USA, 2009, pp. 515-18.

[86] P. R. Gray, Hurst, P. J., Lewis, S. H., Meyer, R. G., *Analysis and design of analog integrated circuits*. New York: John Wiley & Sons, Inc., 2001.

[87] B. Razavi, *Design of analog CMOS integrated circuits*. New York: McGraw-Hill, 2001.

[88] P. E. Allen, D. R. Holberg, *CMOS analog circuit design*. New York: Oxford University Press, Inc., 2002.

[89] C. C. Enz and G. C. Temes, "Circuit techniques for reducing the effects of op-amp imperfections: autozeroing, correlated double sampling, and chopper stabilization," *Proceedings of the IEEE,* vol. 84, pp. 1584-614, 1996.

[90] J. F. Witte, "Dynamic offset compensated CMOS amplifiers," PhD thesis, Delft University of Technology, 2008.

[91] S. Galal and B. Razavi, "10-Gb/s limiting amplifier and laser/modulator driver in 0.18-um CMOS technology," *Solid-State Circuits, IEEE Journal of,* vol. 38, pp. 2138-2146, 2003.

[92] E. Sackinger and W. C. Fischer, "A 3-GHz 32-dB CMOS limiting amplifier for SONET OC-48 receivers," *IEEE Journal of Solid-State Circuits,* vol. 35, pp. 1884-1888, 2000.

[93] M. Degrauwe, E. Vittoz, and I. Verbauwhede, "A micropower CMOS-instrumentation amplifier," *IEEE Journal of Solid-State Circuits,* vol. SC-20, pp. 805-807, 1984.

[94] J. H. Atherton and H. T. Simmonds, "An offset reduction technique for use with CMOS integrated comparators and amplifiers," *IEEE Journal of Solid-State Circuits,* vol. 27, pp. 1168-1175, 1992.

[95] R. R. Harrison and C. Charles, "A low-power low-noise CMOS amplifier for neural recording applications," *IEEE Journal of Solid-State Circuits,* vol. 38, pp. 958-65, 2003.

[96] P. Naktongkul and A. Thanachayanont, "A 1-V 25-dB 100-MHz CMOS variable gain amplifier cell," *IEEE International Symposium on Communications and Information Technology*, 2004, pp. 527-30.

[97] E. Sackinger and W. Guggenbuhl, "A versatile building block: the CMOS differential difference amplifier," *IEEE Journal of Solid-State Circuits,* vol. 22, pp. 287-94, 1987.

[98] H. Alzaher and M. Ismail, "A CMOS fully balanced differential difference amplifier and its applications," *IEEE Transactions on Circuits and Systems II: Analog and Digital Signal Processing,* vol. 48, pp. 614-20, 2001.

[99] L. Seungbae and C. T. C. Nguyen, "Influence of automatic level control on micromechanical resonator oscillator phase noise," *Proceedings of the 2003 IEEE International Frequency Control Symposium and PDA Exhibition. Jointly with the 17th European Frequency and Time Forum*, 2003, pp. 341-9.

[100] L. Yu-Wei, L. Seungbae, L. Sheng-Shian, X. Yuan, R. Zeying, and C. T. C. Nguyen, "Series-resonant VHF micromechanical resonator reference oscillators," *IEEE Journal of Solid-State Circuits,* vol. 39, pp. 2477-91, 2004.

[101] H. Lin, X. Yong Ping, and M. Palaniapan, "A CMOS readout circuit for SOI resonant accelerometer with 4-g bias stability and 20-g/Hz resolution," *IEEE Journal of Solid-State Circuits,* vol. 43, pp. 1480-90, 2008.

[102] T. Kugelstadt, "Active filter design techniques," in *Op amps for everyone: design reference*, R. Mancini, Ed. Burlington, MA: Elsevier, 2003.

[103] R. Hogervorst, J. P. Tero, R. G. H. Eschauzier, and J. H. Huijsing, "A compact power-efficient 3-V CMOS rail-to-rail input/output operational-amplifier for VLSI cell libraries," *IEEE Journal of Solid-State Circuits,* vol. 29, pp. 1505-1513, 1994.

[104] M. Banu, J. M. Khoury, and Y. Tsividis, "Fully differential operational amplifiers with accurate output balancing," *IEEE Journal of Solid-State Circuits,* vol. 23, pp. 1410-1414, 1988.

[105] S. Truax, K. S. Demirci, J. H. Seo, P. Kurzawski, Y. Luzinova, A. Hierlemann, B. Mizaikoff, and O. Brand, "Gas and liquid phase sensing of volatile organics with disk microresonator," *21st IEEE International Conference on Micro Electro Mechanical Systems - MEMS '08*, 2008, pp. 220-3.

[106] S. Truax, K. S. Demirci, A. Hierlemann, and O. Brand, "Exploring the resolution of different disk-type chemical sensors," *15th International Conference on Solid-State Sensors, Actuators and Microsystems. Transducers 2009*, 2009, pp. 1838-41.

[107] A. Sharma, "CMOS sytems and circuits for sub-degree per hour MEMS gyroscopes," PhD thesis, Georgia Institute of Technology, 2007.

[108] "IEEE Standard Definitions of Physical Quantities for Fundamental Frequency and Time Metrology - Random Instabilities," vol. IEEE Std 1139-2008, p. 45, 2009.

[109] D. Lange, "Cantilever-based microsystem for gas sensing and atomic force microscopy," PhD thesis, ETH Zurich, 2000.

[110] J. A. Riddick, Bunger, W. B., Sakano, T. K., *Organic solvents - physical properties and methods of purification*, 4th ed. New York: John Wiley & Sons, 1986.

[111] A. Koll, "CMOS capacitive chemical microsystems for volatile organic compounds," PhD thesis, ETH Zurich, 1999.

[112] "SFC4100 ulta-fast CMOSens mass flow controller for gases," in *Sensirion Datasheet*, 2009.

[113] F. L. Walls and J. J. Gagnepain, "Environmental sensitivities of quartz oscillators," *IEEE Transactions on Ultrasonics, Ferroelectrics and Frequency Control,* vol. 39, pp. 241-9, 1992.

[114] M. Koskenvuori, T. Mattila, A. Haara, J. Kiihamaki, I. Tittonen, A. Oja, and H. Seppa, "Long-term stability of single-crystal silicon microresonators," *Sensors and Actuators A (Physical),* vol. A115, pp. 23-7, 2004.

[115] J. H. Seo, K. S. Demirci, A. Byun, S. Truax, and O. Brand, "Temperature compensation method for resonant microsensors based on a controlled stiffness modulation," *Journal of Applied Physics,* vol. 104, pp. 014911-1-9, 2008.

[116] B. Roith, A. Gollwitzer, A. Lerner, and G. Fischerauer, "Microcontroller-based temperature compensation scheme for two-port SAW oscillators," *IEEE International Frequency Control Symposium*, 2006, pp. 827-830.

[117] J. H. Smith and S. D. Senturia, "Self-consistent temperature compensation for resonant sensors with application to quartz bulk acoustic wave chemical sensors," *International Conference on Solid-State Sensors and Actuators, and Eurosensors IX*, 1995, pp. 724-727.

[118] J. R. Vig, "Temperature-insensitive dual-mode resonant sensors-a review," *Sensors Journal,* vol. 1, pp. 62-68, 2001.

[119] R. Melamud, M. Hopcroft, C. Jha, K. Bongsang, S. Chandorkar, R. Candler, and T. W. Kenny, "Effects of stress on the temperature coefficient of frequency in double clamped resonators," *The 13th International Conference on Solid-State Sensors, Actuators and Microsystems*, 2005, pp. 392-395.

[120] M. K. Jain, S. Schmidt, and C. A. Grimes, "Magneto-acoustic sensors for measurement of liquid temperature, viscosity and density," *Applied Acoustics,* vol. 62, pp. 1001-1011, 2001.

[121] S. J. Martin, R. W. Cernosek, and J. J. Spates, "Sensing liquid properties with shear-mode resonator sensors," *International Conference on Solid-State Sensors and Actuators, and Eurosensors IX*, Stockholm, Sweden, 1995, pp. 712-715.

[122] S. Bianco, M. Cocuzza, S. Ferrero, E. Giuri, G. Piacenza, C. F. Pirri, A. Ricci, L. Scaltrito, D. Bich, A. Merialdo, P. Schina, and R. Correale, "Silicon resonant microcantilevers for absolute pressure measurement," *Journal of Vacuum Science Technology B (Microelectronics and Nanometer Structures),* vol. 24, pp. 1803-1809, 2006.

[123] M. A. Hopcroft, M. Agarwal, K. K. Park, B. Kim, C. M. Jha, R. N. Candler, G. Yama, B. Murmann, and T. W. Kenny, "Temperature Compensation of a MEMS Resonator Using Quality Factor as a Thermometer," *19th IEEE International Conference on Micro Electro Mechanical Systems, 2006. MEMS 2006 Istanbul*, 2006, pp. 222-225.

[124] R. Sunier, T. Vancura, Y. Li, K.-U. Kirstein, H. Baltes, and O. Brand, "Resonant magnetic field sensor with frequency output," *Journal of Microelectromechanical Systems,* vol. 15, pp. 1098-1107, 2006.